Radiation Generation from Ultra Intense Laser Plasma Interactions with Solid Density Plasmas for Active Interrogation of Nuclear Materials

by

Calvin Andrew Zulick

A dissertation submitted in partial fulfillment
of the requirements for the degree of
Doctor of Philosophy
(Nuclear Science)
in The University of Michigan
2014

Doctoral Committee:

Professor Karl M. Krushelnick, Chair
Professor Yogesh B. Gianchandani
Research Scientist Anatoly M. Maksimchuk
Associate Professor Alexander G. R. Thomas
Assistant Professor Louise Willingale

ACKNOWLEDGEMENTS

The work presented in this thesis would not have been possible without the support of the High Field Science group. I would like to thank my advisor, Professor Karl Krushelnick, for providing invaluable guidance during my studies, and providing me with the freedom to become involved in many research projects, both at the University of Michigan and external facilities. Thank you to Professor Louise Willingale for involving me in her research at Lawrence Livermore National Laboratory and the Laboratory for Laser Energetics in Rochester, as well as for her expert editing feedback. Dr. Anatoly Maksimchuk's oversight of the HERCULES experiments was critical to their success, and I thank him for the knowledge he has passed down to me. Thank you to Professor Alec Thomas for providing both computational and theoretical support to help explain the experiments, as well as serving as an unequaled resource for plasma physics theory. Of course, no experiments would have been possible without the effort of Dr. Victor Yanovsky, Dr. Vladimir Chvykov, and Dr. Galina Kalinchenko, and I am very appreciative of their hard work. Thanks are also due to John Nees and Dr. Bixue Hou for their assistance at the λ^3 laser.

I would also like to thank Dr. Christopher McGuffey, who's dedication to his Ph.D. studies served as an inspiration for the rest of us. My deepest thanks are due to Dr. Franklin Dollar for serving as a mentor and letting me ride in his experimental wakefield. Thank you to the other HFS students as well, particularly Anthony Raymond and Andrew McKelvey, for their assistance in the lab.

Thank you to Dr. Usha Varshney and Dr. Rajinder Khosla for their encourage-

ment to return to school. Thanks to Mr. McLaughlin for teaching a chemistry and physics class worthy of the subject. Thank you to Mr. Apinis for helping to inspire two generations of Zulicks to be interested in the world around them.

Thanks to Tim - you know what you've done. Thank you to my family for their support for all the years leading up to this point. Finally, thank you to Cheryl for everything.

PREFACE

This thesis presents work reported by the Author in the following publications:

1. **C. Zulick**, F. Dollar, V. Chvykov, J. Davis, G. Kalinchenko, A. Maksimchuck, G.M. Petrov, A. Raymond, A.G.R. Thomas, L. Willingale, V. Yanovsky, and K. Krushelnick. Energetic neutron beams generated from femtosecond laser plasma interactions. *Applied Physics Letters*, 102(12):4101, 2013.

2. **C. Zulick**, F. Dollar, V. Chvykov, J. Davis, G. Kalinchenko, A. Maksimchuk, G. M. Petrov, A. Raymond, A. G. R. Thomas, L. Willingale, V. Yanovsky, and K. Krushelnick. Ultra-intense laser neutron generation through efficient deuteron acceleration. *Proceedings of SPIE*, 8779:87790N–87790N–9, 2013.

3. **C. Zulick**, B. Hou, F. Dollar, A. Maksimchuk, J. Nees, A.G.R. Thomas, Z. Zhao, and K. Krushelnick. High resolution bremsstrahlung and fast electron characterization in ultrafast intense laser–solid interactions. *New Journal of Physics*, 15(12):123038, 2013.

The Author has also participated in research reported in the following publications which is not presented in this thesis:

4. **C. Zulick**, F. Dollar, H. Chen, K. Falk, G. Gregori, A. Hazi, C.D. Murphy, J. Park, J. Seely, C.I. Szabo, R. Tommasini, R. Shepherd, and K. Krushelnick.

K-shell spectroscopy of Au plasma generated with a short-pulse laser. *Canadian Journal of Physics*, 89(5):647–651, 2011.

5. F. Dollar, **C. Zulick**, A. G. R. Thomas, V. Chvykov, J. Davis, G. Kalinchenko, T. Matsuoka, C. McGuffey, G. M. Petrov, L. Willingale, V. Yanovsky, A. Maksimchuk, and K. Krushelnick. Finite spot effects on radiation pressure acceleration from intense high-contrast laser interactions with thin targets. *Physical Review Letters*, 108(17):175005, 2012.

6. F. Dollar, P. Cummings, V. Chvykov, L. Willingale, M. Vargas, V. Yanovsky, **C. Zulick**, A. Maksimchuk, A. G. R. Thomas, and K. Krushelnick. Scaling high-order harmonic generation from laser-solid interactions to ultrahigh intensity. *Physical Review Letters*, 110:175002, Apr 2013.

7. F. Dollar, **C. Zulick**, T. Matsuoka, C. McGuffey, S.S. Bulanov, V. Chvykov, J. Davis, G. Kalinchenko, G.M. Petrov, L. Willingale, V. Yanovsky, A. Maksimchuk, A.G.R. Thomas, and K. Krushelnick. High contrast ion acceleration at intensities exceeding 10^{21} Wcm^{-2}. *Physics of Plasmas*, 20(5):056703, 2013.

8. A. Maksimchuk, A. Raymond, F. Yu, G.M. Petrov, F. Dollar, L. Willingale, **C. Zulick**, J. Davis, and K. Krushelnick. Dominant dueteron acceleration. *Applied Physics Letters*, 102(19):191117, 2013.

9. L. Willingale, P. M. Nilson, A. G. R. Thomas, J. Cobble, R. S. Craxton, A. Maksimchuk, P. A. Norreys, T. C. Sangster, R. H. H. Scott, C. Stoeckl, **C. Zulick**, and K. Krushelnick. High-power, kilojoule class laser channeling in millimeter-scale underdense plasma. *Phys. Rev. Lett.*, 106:105002, Mar 2011.

10. L. Willingale, A.G.R. Thomas, P.M. Nilson, H. Chen, J. Cobble, R. S. Craxton, A. Maksimchuk, P.A. Norreys, T.C. Sangster, R.H.H. Scott, C. Stoeckl, **C. Zulick**, and K. Krushelnick. Surface waves and electron acceleration from

high-power, kilojoule-class laser interactions with underdense plasma. *New Journal of Physics*, 15(2):025023, 2013.

11. L. Willingale, P.M. Nilson, A G R Thomas, J. Cobble, R.S. Craxton, A Maksimchuk, P.A Norreys, T.C. Sangster, R.H.H. Scott, C. Stoeckl, **C. Zulick**, and K. Krushelnick. Proton probe imaging of fields within a laser-generated plasma channel. *IEEE Transactions on Plasma Science*, 39(11):2616–2617, 2011.

12. Hui Chen, D.D. Meyerhofer, S.C. Wilks, R. Cauble, F. Dollar, K. Falk, G. Gregori, A. Hazi, E.I. Moses, C.D. Murphy, J. Myatt, J. Park, J. Seely, R. Shepherd, A. Spitkovsky, C. Stoeckl, C.I. Szabo, R. Tommasini, **C. Zulick**, and P. Beiersdorfer. Towards laboratory produced relativistic electronpositron pair plasmas. *High Energy Density Physics*, 7(4):225 – 229, 2011.

13. W. Schumaker, N. Nakanii, C. McGuffey, **C. Zulick**, V. Chyvkov, F. Dollar, H. Habara, G. Kalintchenko, A. Maksimchuk, K.A. Tanaka, , A. G. R. Thomas, V. Yanovsky, and K. Krushelnick. Ultrafast electron radiography of magnetic fields in high-intensity laser-solid interactions. *Physical Review Letters*, 110(1):015003, 2013.

14. C. McGuffey, T. Matsuoka, S. Kneip, W. Schumaker, F. Dollar, **C. Zulick**, V. Chvykov, G. Kalintchenko, V. Yanovsky, A. Maksimchuk, A. G. R. Thomas, K. Krushelnick, and Z. Najmudin. Experimental laser wakefield acceleration scalings exceeding 100TW. *Physics of Plasmas*, 19(6), 2012.

TABLE OF CONTENTS

ACKNOWLEDGEMENTS ii

PREFACE iv

LIST OF FIGURES x

LIST OF TABLES xvi

LIST OF ABBREVIATIONS xviii

ABSTRACT xx

CHAPTER

I. Introduction 1

1.1 Homeland Security 1
1.2 Active Interrogation Techniques 3
1.3 Conventional Accelerators 6
1.3.1 Photon Sources 6
1.3.2 Neutron Sources 7
1.3.3 Current Research 7
1.4 Laser Plasma Accelerators 10
1.4.1 Photon Experiments 11
1.4.2 Neutron Experiments 13
1.4.3 High Repetition Rate Accelerators 16
1.5 Thesis Overview 16

II. Theoretical Background 18

2.1 Laser Physics 18
2.1.1 Chirped Pulse Amplification 19
2.1.2 Nonlinear Optics 20
2.2 Laser Plasma Physics 24
2.2.1 Normalized Vector Potential 25

2.2.2 Ponderomotive Force . . . 25
2.2.3 Laser Absorption Mechanisms . . . 27
2.2.4 Scaling Laws . . . 30
2.3 Ion Acceleration . . . 31
2.3.1 Target Normal Sheath Acceleration . . . 31
2.4 Photon Generation . . . 32
2.4.1 K-shell Radiation . . . 33
2.4.2 Bremsstrahlung Radiation . . . 33

III. Methods . . . 40

3.1 Experimental Facilities . . . 40
3.1.1 HERCULES Laser System . . . 40
3.1.2 λ^3 Laser System . . . 43
3.2 Laser Diagnostics . . . 44
3.2.1 Diffraction Limited Focusing . . . 45
3.2.2 Pulse Duration Measurements . . . 49
3.3 Laser Contrast . . . 54
3.4 Radiation Diagnostics . . . 58
3.4.1 CR-39 . . . 59
3.4.2 Thomson Parabola Ion Spectrometer . . . 60
3.4.3 Neutron Time-of-Flight . . . 67
3.4.4 High Purity Germanium Detector . . . 72
3.5 Computational Modeling . . . 76
3.5.1 Monte Carlo N Particle Transport Code . . . 77
3.5.2 OSIRIS . . . 78

IV. Bremsstrahlung Generation . . . 81

4.1 Introduction . . . 81
4.2 Experimental Setup . . . 83
4.3 Bremsstrahlung Spectrum . . . 86
4.4 Simulations . . . 89
4.5 Activation . . . 93
4.6 Conclusion . . . 94

V. Proton Acceleration from Structured Targets . . . 97

5.1 Introduction . . . 97
5.2 Experimental Setup . . . 98
5.3 Ion Acceleration and Electron Dynamics . . . 100
5.4 Simulations . . . 104
5.5 Conclusions . . . 106

VI. Neutron Generation . . . 108

6.1 Introduction 108
6.2 Experimental Setup 109
6.3 Ion Optimization 114
6.4 Neutron Measurements 117
6.5 Simulations 118
6.6 Activation 122
6.7 Conclusions 122

VII. Conclusions and Outlook 125

7.1 Summary and Discussion 125
7.2 Future Applications and Outlook 126

APPENDICES 129

BIBLIOGRAPHY 133

LIST OF FIGURES

Figure

2.1 Schematic of 1 set of gratings in a parallel Treacy compressor, as used in the HERCULES laser. G is the grating separation, d is the grating line spacing, and the angles γ and θ are as indicated. 21

2.2 Energy level diagram of Cu showing the Cu K_α, CuK_β and binding energy. 34

2.3 Plot of the nonrelativistic bremsstrahlung cross sections as a function of the ratio between the photon and electron energy. The analytic cross section peaks at low photon energies drops to zero for a photon energy equal to the electron energy. The semi-empirical cross section captures the overall behavior. 36

2.4 Plot of the analytic and semi-empirical formulations of the angularly resolved bremsstrahlung cross sections. The shape of the two curves deviate for large angles. 38

3.1 Block diagram of the HERCULES laser system. Red blocks represent 800 nm laser amplification stages, while green blocks represent 532 nm pump lasers. Each stage is identified by its colloquial name. The post-compressor pulse is directed to the target chamber. 41

3.2 Block Diagram of the λ^3 laser system. Red blocks represent 800 nm laser amplification stages, while green blocks represent 532 nm pump lasers. Each stage is identified by its colloquial name. The post-compressor pulse was directed to the target chamber. 44

3.3 Screen captures of the HASO diagnostic showing the (a) pre-correction wavefront aberration, (b) pre-correction calculated focal spot, (c) post-correction wavefront aberration, and (d) post-correction focal spot. The wave front aberration is a spatially resolved measurement of the aberration in the incoming laser pulse measured at the DM surface. The color bar shows the magnitude of the wavefront aberration while the peak-to-valley and root-mean-squared values are shown on the bottom right. The focal spot image is a calculated optimum distribution of the light at focus given the wavefront measured at the surface of the DM. 47

3.4 Focal spot from an F/1 parabola after DM correction with a 1.18 μm FWHM. The OD4 (blue) and OD5 (green) profiles show the spot with two filter configurations, increasing the dynamic range of the measurement. The OD5 plot has been scaled by an order of magnitude, compensating for the increase filter attenuation, to match the OD4 plot. (Inset) False color image of the focal spot with OD4 filtering showing the structure around the beam while the central portion is saturated. 48
3.5 Schematic for a single shot second order autocorrelator. The beam was split and then recombined and focused into a BBO crystal. The second harmonic light was imaged to a CCD while the first harmonic was removed with a BG-39 filter. 50
3.6 False color image of the autocorrelation light produced in the second harmonic crystal. A rotation of 2^o was performed to measure the pulse duration to account for the tilt of the pulse, which was a result of the imaging system. 51
3.7 Pulse duration measurement of the HERCULES compressed pulse from second order autocorrelation showing a minimum pulse duration of 39 fs. The measurement was performed with XPW under vacuum. The grating position was relative to the approximate best compression position for the non-XPW pulse. Negative grating positions correspond to less negative chirp when compared to the reference position of zero. 52
3.8 Pre-compressor optical spectrum of the HERCULES pulse showing a FWHM of 25.5 nm. The spectrum was recorded for every shot by collecting leak-through light from a 7 inch high reflectivity dielectric mirror located in the pre-compressor periscope. The light was focused into an optical fiber, through a diffuser, and delivered to a CCD Spectrometer. 53
3.9 (Reproduced from V. Chvykov *et al.* [87]). Third-order autocorrelation with XPW (red) and without (black). The peaks of the red curve at the $10^{-10} - 10^{-11}$ level are due to single photoelectrons. . 55
3.10 (Reproduced from Doumy, G. *et. al.* [91]). Reflectivity of bulk quartz as a function of incident fluence for three pulse durations. The fit shows good agreement with the developed theoretical model for the 4 ps pulse. 57
3.11 (Reproduced from Dollar, F. *et. al.* [93]). (a) The normalized laser energy as a function of time as measured by a fast diode. The XPW only (red) and post-DPM (green) traces were taken simultaneously. (b) 30 TW laser power flux measurements (red) as measured by a third order autocorrelator. Inferred DPM contrast is shown (blue) along with the preplasma formation threshold fluence. Lines are shown for visual aid only. 58
3.12 Microscope image of CR-39 exposed to a proton beam. Pits with two distinct sizes are visible. 59

3.13 Image of the CR-39 after a binary conversion has been performed using a threshold value to highlight the dark centers of the pits. The two pit sizes are still distinguishable through size variation. 61
3.14 Result of applying the Image-J particle counting algorithm to the binary image which shows 70 identified pits. Only circles with areas between 10 and 70 pixels were counted. This rejected false positives from single pixel noise and the larger heavy ion pits. 61
3.15 Diagram depicting the geometry of the Thomson Parabola. The electric field (orange) separates ions by q/m with lower ratios dispersed further from the axis. The magnetic field (green) disperses in the orthogonal axis with higher energy particles closer to the straight-through. 62
3.16 Thomson data from 1.8 μm Al overlaid with parabolas for different charge states. The three species are shown in different colors with the lowest charge ratios to the bottom left. The parabola for each charge species of H (green), Al (yellow), and C (magenta), is plotted according to Eqn. 3.4. The presence of Al^{13+} indicates a laser intensity of $>= 7 \times 10^{20}\ W/cm^2$. 64
3.17 Schematic depicting the placement of CR-39 to measure the proton flux allowing a calibration of the TP. The "finger" cut-outs allow simultaneous single-shot measurement of the proton trace on the MCP and CR-39. 65
3.18 Calibrated TP spectrum showing MCP signal (line) and CR-39 (crosses) data points demonstrating consistency between the two methods. The target was 6 μm Al shot with the $F/1$ parabola and 150 TW laser power. 66
3.19 Schematic of the 35.5 cm nToF detector showing the Pb blocks used to shield the detector from photons. The detector was positioned on top of a pedestal to keep it in the interaction plane. 68
3.20 Sample oscilloscope trace from the plastic scintillator for a laser interaction creating photons and neutrons together. The gammas travel from the laser interaction at the speed of light and arrive at the detector first. The neutrons travel slower and arrive later yielding a measurement of their energy through the measured speed. A region of no signal between the gamma spike and the neutron arrival, as pictured in this trace, is very important for a quantitative measurement of the neutron flux. 70
3.21 Sample oscilloscope trace from the plastic scintillator for a single D-D neutron hit. 71
3.22 Plot showing the number of counts as a function of the peak voltage threshold. The average peak area is also shown as a function of the threshold voltage. The optimum threshold voltage was found to be 0.02 V. At this threshold the average area of a detected neutron peak was 1.5 V×ns. 72

3.23 The HPGe detector's intrinsic photopeak efficiency was measured using 6 peaks that spanned the energy range from 274 keV to 1.33 MeV. The efficiency fits a power function over this range which is dominated by Compton scattering. Below 100 keV the efficiency drops as the dominant energy transfer mechanism becomes photoelectric absorption. 76
4.1 Experimental setup of the target chamber. The bremsstrahlung observation angles are shown. 84
4.2 a) Eu_2O_3 spectrum accumulated over 1.9 million shots. The resolution is sufficient to resolve nuclear peaks (511 keV) and Pb $K_{\alpha,\beta}$ peaks. b) Bremsstrahlung spectrum showing the characteristic two effective temperature spectral shape for SiO_2 along the specular direction. T_{b1} = 286 (±9) keV (blue) and T_{b2} = 480 (±31) keV (red) are shown along with the 95% confidence fits (dashed lines). The data was taken with $a_0 = 2.3$ over 180k shots. Data is summed into 10 channel bins for clarity. 87
4.3 a) The T_{b1} (black) and T_{b2} (green) experimental bremsstrahlung temperatures, observed from $\theta = 0^o$ on Eu_2O_3, with the power law fits for T_{b1} (blue) and T_{b2} (red). b) The calculated T_{e1} (blue) and T_{e2} (red) experimental electron temperatures from the bremsstrahlung temperatures in (a) with the Beg (black), λ^3 (red) and ponderomotive (green) theoretical scalings (dashed). The calculated scalings use the relationship between T_e and T_b determined from MCNPX. . . . 88
4.4 Experimental (data points) bremsstrahlung temperatures as a function of observed angle compared to MCNPX predictions (dotted lines). T_{b2} (red) and T_{b1} (blue) are shown, along with the target geometry and laser direction for clarity. The heavy dashed line (black) shows the average electron energy as a function of angle, PIC $< E_e >$ taken from a particle-in-cell simulation. 89
4.5 MCNPX results demonstrating the effect of two electron sources. The combination of two sources with different temperatures reproduces the two temperature bremsstrahlung signal observed experimentally. 92
4.6 MCNPX results showing the relationship between T_b and T_e for 3.5 mm of stainless steel. 93
4.7 ^{238}U spectra measured with the HPGe detector. The activated (green) spectrum is nearly overlapped with the background (red) spectrum. The difference between the two spectra (blue) shows a slight increase in K_α signal, mostly from Pb. 94
5.1 HERCULES solid target area chamber schematic. Plasma mirrors were not used in this experiment. 99

5.2 Cu K_α images of (a) wire (b) mesh and (c) foil targets. The confinement of electrons due to the target geometry leads to strong electron currents that illuminate the target. Vertically integrated profiles of the images (d) show how the signal is distributed. Dashed lines represent the scaled simulation results and show excellent agreement. . . . 102
5.3 Ion spectra from (triangle) wire (square) mesh and (circle) foil targets. The values represent the flux of protons above the threshold energy for the filter stack. The slope of the lines of best fit decreases from the foil to mesh to wire target. The dashed portions of the fits continue to fluxes higher than the saturation point of the CR−39 detector. . . . 103
5.4 Microscope image of CR−39 located 1 cm from a mesh target (a) showing mesh pattern in the proton distribution. Scan of CR−39 from a wire target (b) showing a line focusing feature in the proton distribution 1 cm behind the target. The orientation of the focused line was perpendicular to the orientation of the wire target. This feature was also observed 5 cm behind the target with the same angular divergence. . . . 104
5.5 Data from Vlasov-Fokker-Planck simulation for representations of (a,c) wire and (b,d) mesh targets. The (a,b) magnetic fields are shown at 500 fs and the (c,d) electric fields are shown at 600 fs . Arrows indicate the direction of the electric fields. . . . 105
6.1 The (n, f) cross sections for common fissile, ^{235}U (blue) and ^{239}Pu (black), fissionable, ^{238}U (green), and naturally occuring, ^{208}Pb (red), materials. The optimum neutron interrogation energy is above the fissionable material threshold energy, MeV's, and below the naturally occurring materials, 10's of MeV. . . . 109
6.2 HERCULES solid target area chamber schematic. nToF plastic scintilator location is not to scale. . . . 110
6.3 Sketch of the target and catcher configuration. The laser interacted with the front side of the foil and accelerated ions from the rear surface, through TNSA, into the catcher. The deuterated ice contaminant layer formed a distinct layer over the hydrogenous contaminants for the D-Li (Ice) target, but was not as well defined for D-Li (Paint). 112
6.4 Raw nToF data from the detector at 9.45 m with (black) and without (grey) the LiF catcher. In the absence of the catcher the photon flash showed a smooth decay without additional scattered photon signal or signal reflections. The LiF catcher shot showed a neutron signal clearly separated from the photon flash. . . . 113

6.5 Simulated and experimental ion (a) and neutron (b) spectra along the target normal direction. (a) The P-Li spectrum from 100 nm Parylene shows the highest energies and total flux. The D-Li (Ice) spectrum shows higher flux and energy than D-Li (Paint). The simulated D-Li (Ice) spectrum was calculated with exponential scale length L_s = 100nm and scaled to match the experimental flux. (b) Experimental spectra from the four reactions. Monte Carlo simulated neutron spectra are shown for comparison. 114
6.6 Ion spectra for q/m = 1 (a) and q/m = 1/2 (b) parabolas from sequential laser shots on 1.8 μm Al foil. (a) Proton spectra for the clean and ice covered target case showing suppression of the protons by the ice layer. (b) q/m = 1/2 trace showing a small amount of C^{6+} contaminant for the clean case. The ice case shows no O^{7+} which precludes the presence of O^{8+} contamination in the trace, as well as no carbon traces, yielding a pure deuteron signal. The corresponding Thomson parabola traces for the clean (c) and ice (d) case demonstrate the dramatic increase in deuteron signal. Additionally, the heavy ion traces change from carbon (c) to oxygen (d). The dashed lines indicate the location of the proton and q/m = 1/2 parabolas. 116
6.7 The purity, measured as the ratio of the number (black) or total energy (grey) of deuterons to protons observed on the TP with energies above 0.5 MeV, for different timing delays between the heavy water spray and laser pulse arrival on D-Li (Ice) targets. The number ratio approaches the limit of 500, due to impurities in the D_2O, for short timing delays. At longer timing delays the deuterated ice layer sublimates and is contaminated with hydrogenous materials. 117
6.8 MCNPX simulated nToF energy spectrum for mono-energetic neutron beams of 2.54, 10, and 15 MeV for the 9.45 m detector. The downshift is a result of the LiF converter as well as the chamber and shielding materials between the detector and neutron source. . . . 121
6.9 ^{238}U gamma spectrum measured with the HPGe detector. The fission fragment ^{94}Sr is typically used as an indicator of the fission of ^{238}U. The location of the ^{94}Sr line at 1384 keV is indicated with an arrow, and was not observed in this spectrum. 122

LIST OF TABLES

Table

1.1 Global SNM stockpile in metric tons as of the end of 2003. Declared Excess stockpiles have been designated for down blending into low-enriched uranium. 2

1.2 A list of nuclear reactions that have been proposed for active interrogation methods. The resulting radiation, along with the time scale of the radiation indicates the necessary detection methods. 4

1.3 A comparison of various accelerator sources. Each method generates either neutrons or gammas. 8

1.4 A comparison of various laser neutron sources. In results reported by Lancaster *et al.* - Pretzler *et al.* the neutrons were generated through a two-step process where ions were accelerated and then a nuclear reaction produced the neutron. Alternatively, Fritzler *et al.*, Taylor *et al.*, and Ditmire *et al.* reported laser fusion schemes. The lower laser energy and high repetition rate results represent progress toward a practical accelerator for homeland security applications. All results were demonstrated on single shot lasers except for Prezler *et al.* which was performed on a 10 Hz laser. The calculation by Taylor *et al.* relies on the development of Inertial Fusion Energy drivers over the next 20 to 30 years. 15

3.1 Table showing sources along with calibrated activities. All sources were calibrated November 16th, 2000, and the decay of their activity has been taken into account in the listed numbers. 75

4.1 Bremsstrahlung temperature along the $\theta = 0^o$ direction compared to MCNPX simulation results for $T_e = 200$ keV. Note the Z dependence in the MCNPX simulation is not observed experimentally. 89

6.1 Nuclear reactions and target configurations investigated on HERCULES. The (D,D) reaction used the thick target material for the deuteron source and converter. The other reactions used thin target and a LiF catcher. 110

6.2 Nuclear reactions and target configurations investigated on HERCULES. The highest measured flux was observed for the P-Li reaction, and the highest energy was observed for the D-Li (ice) reaction. 118

7.1 A comparison of various laser neutron sources, highlighting the HERCULES results presented in this thesis. The other results are reproduced from Table 1.4 126

LIST OF ABBREVIATIONS

ASE Amplified Spontaneous Emission

CD Deuterated Polyethylene

CPA Chirped Pulse Amplification

CR-39 Allyl Diglycol Carbonate or Columbia Resin 39

CUOS Center for Ultrafast Optical Science

DM Deformable Mirror

FSA Front Side Acceleration

FWHM Full Width at Half Maximum

HERCULES High Energy Repetitive CUos Laser System

HPGe High Purity Germanium

LINAC Linear Accelerator

MCP Microchannel Plate

MCNPX Monte Carlo N-Particle eXtended

MHD Magnetohydrodynamics

NRF Nuclear Resonance Fluorescence

nToF Neutron Time of Flight

OAP Off-Axis Parabolic Mirror

PIC Particle-In-Cell

PMs Plasma Mirrors

PPC Particles-Per-Cell

q/m Charge to Mass Ratio

Regen Regenerative Amplifier

RF Radio Frequency

SNM Special Nuclear Materials

TNSA Target Normal Sheath Acceleration

TP Thomson Parabola Ion Spectrometer

VFP Vlasov-Fokker-Planck

XPW Cross-Polarized Wave Generation

ABSTRACT

Radiation Generation from Ultra Intense Laser Plasma Interactions with Solid Density Plasmas for Active Interrogation of Nuclear Materials

by

Calvin Andrew Zulick

Chair: Karl Krushelnick

The development of short pulse high power lasers has led to interest in laser based particle accelerators. Laser produced plasmas have been shown to support quasi-static TeV/m acceleration gradients which are more than four orders of magnitude stronger than conventional accelerators. These high gradients have the potential to allow compact particle accelerators for active interrogation of nuclear material. In order to better understand this application, several experiments have been conducted at the HERCULES and λ^3 lasers as the Center for Ultrafast Optical Science at the University of Michigan.

Electron acceleration and bremsstrahlung generation were studied on the λ^3 laser. The scaling of the intensity, angular, and material dependence of bremsstrahlung radiation from an intense (I>10^{18} W/cm^2) laser-solid interaction has been characterized at energies between 100 keV and 1 MeV. These were the first high resolution ($\lambda/\Delta\lambda$>100) measurements of bremsstrahlung photons from a relativistic laser plasma interaction. The electron populations and bremsstrahlung temperatures were modeled in the particle-in-cell code OSIRIS and the Monte Carlo code MCNPX and were

in good agreement with the experimental results.

Proton acceleration was studied on the HERCULES laser. The effect of three dimensional perturbations of electron sheaths on proton acceleration was investigated through the use of foil, grid, and wire targets. Hot electron density, as measured with an imaging Cu K_α crystal, increased as the target surface area was reduced and was correlated to an increase in the temperature of the accelerated proton beam.

Additionally, experiments at the HERCULES laser facility have produced directional neutron beams with energies up to 16.8($\pm$0.3) MeV using $^{2}_{1}$d(d,n)$^{3}_{2}$He, $^{7}_{3}$Li(p,n)$^{7}_{4}$Be, and $^{7}_{3}$Li(d,n)$^{8}_{4}$Be reactions. Efficient $^{7}_{3}$Li(d,n)$^{8}_{4}$Be reactions required the selective acceleration of deuterons through the introduction of a deuterated plastic or cryogenically frozen D_2O layer on the surface of a thin film target. The measured neutron yield was up to 1.0 ($\pm$0.5)$\times 10^7$ neutrons/sr with a flux 6.2($\pm$3.7) times higher in the forward direction than at 90^o. This demonstrated that femtosecond lasers are capable of providing a time averaged neutron flux equivalent to commercial $^{2}_{1}$d(d,n)$^{3}_{2}$He generators with the advantage of a directional beam with picosecond bunch duration.

CHAPTER I

Introduction

1.1 Homeland Security

The discovery of subatomic particles in the early 20th century began a chain reaction of scientific breakthroughs leading to the creation of the research fields of nuclear and atomic physics. In the 1940's the Manhattan Project led to the first detonation of a nuclear weapon in the 1945 Trinity test [1]. Nine years later the first civilian nuclear power plant began operation in Obninsk, Russia. In the sixty years that have passed, nuclear proliferation has led to stockpiles of nuclear fuel and weapons across the world, as shown in Table 1.1[2]. Ensuring the security of this stockpile, spread through multiple countries in varying states of political stability, has proven to be a challenging task. In the unfortunate event that Special Nuclear Materials (SNM) is obtained for nefarious purposes, a limited number of pathways exist for transportation of the material into the United States. Every year more than six million cargo containers enter U.S. ports [3], and 15 million trucks cross the Canada-U.S. and Mexico-U.S. borders. Monitoring this traffic has been identified as a critical requirement for homeland security.

The detection of illicit nuclear material presents a difficult challenge. Shielded SNM, in particular ^{235}U which primarily emits a weak 185.6 keV gamma, can be difficult or impossible to detect with passive methods due to the ease of shielding

Table 1.1: Global SNM stockpile in metric tons as of the end of 2003. Declared Excess stockpiles have been designated for down blending into low-enriched uranium.

Category	Plutonium	Highly Enriched Uranium	Total
Civil Stocks	**1,700**	**175**	**1,875**
Reactor Programs	1595	50	
Declared Excess	105	125	
Military Stocks	**155**	**1,725**	**1,880**
Weapons	155	1,250	
Naval and Other		175	
Declared Excess		300	
Total	**1,855**	**1,900**	**3,755**

the radiation. Active interrogation can increase the detection likelihood of shielded materials through induced nuclear reactions. These reactions can exploit delayed radiation decays and characteristic photon energies to increase the signal to noise ratio through time and energy gating, respectively. Complementary techniques such as radiography also exist which take advantage of the energetic photon and neutron beams necessary for active interrogation to map the high density and high-Z areas of containers to identify possible shielded areas. In addition to nuclear material cargo inspection, active interrogation techniques have applications in nuclear safeguards [4], and explosives detection [5]-[6].

In active interrogation schemes, high energy ($>$ MeV) neutrons and photons are used to activate the materials. Generation of energetic photons and neutrons has traditionally been accomplished by accelerating electrons and ions using a Linear Accelerator (LINAC) and generating photons through bremsstrahlung [7] or neutrons through (p,n) reactions [8]. The decay of naturally radioactive material also generates photons and neutrons which can be used for active interrogation, however the use of such a source entails additional security concerns. As the interest in active interrogation has grown over the past 10 years, the need for advanced accelerators has become apparent. Specifically, improved radiation sources are needed which will satisfy speed, detection, and exposure limitations, potentially leading to

the widespread application of active interrogation techniques. Additionally, novel accelerators are needed to enable advanced interrogation methods, such as Nuclear Resonance Fluorescence (NRF), which requires tunable, high flux, narrow bandwidth photon beams.

1.2 Active Interrogation Techniques

Active interrogation schemes utilize high energy (> MeV) neutrons and photons to activate materials due to their increased ability to penetrate air and shielding materials. The resulting nuclear reactions produce photons and neutrons which must escape the container and shielding in order to be detected. Neutrons and photons are intrinsically complementary interrogation methods due to the different ways they scatter and are absorbed in materials. Neutrons primarily interact with atomic nuclei through multiple elastic scattering events, of which the energy lost to the recoil nucleus for each scattering event is:

$$E_R = \frac{2A}{(1+A)^2}(1 - cos(\theta))E_n \tag{1.1}$$

where A is the mass of the target nucleus, θ is the scattering angle of the neutron in the center-of-mass coordinate system, and E_n is the initial neutron energy [9]. As the atomic mass of the scattering nucleus increases, the maximum energy lost per collision decreases and neutrons are able to penetrate further into the material.

Alternatively, photons interact with an atom's electron cloud through photoelectric absorption, Compton scattering, and pair production. The photoelectric absorption cross section is described by the Bragg-Pierce law and is approximately proportional to $\frac{Z^n}{E_\gamma^{3.5}}$ where n varies between 4 and 5. Pair production scales with Z^2 for the conversion of gammas to pairs [10]-[11]. Thus, as the atomic number of the material

Table 1.2: A list of nuclear reactions that have been proposed for active interrogation methods. The resulting radiation, along with the time scale of the radiation indicates the necessary detection methods.

Reaction	Product	Time Scale
Photofission (γ,f)	γ and n	Prompt and delayed
Neutron induced fission (n,f)	γ and n	Prompt and delayed
Nuclear resonance fluorescence (γ, γ')	γ	Prompt
Photoneutron emission (γ,n)	n	Prompt
X-ray fluorescence (γ,γ')	x-ray	Prompt
Inelastic neutron scattering (n,n')	γ	Prompt
Capture neutrons (n,γ)	γ	Prompt and delayed

increases, the photon attenuation increases, in contrast to neutrons.

A large assortment of nuclear reactions can be induced in active interrogation techniques, as seen in Table 1.2. The fission of nuclear material produces fission fragments which decay and emit prompt and delayed gammas and neutrons. The presence of delayed gammas with energies greater than 3 MeV has been identified as a unique characteristic of nuclear materials which can be used to discriminate against background signal resulting from the activation of shielding materials [12]. Delayed gammas also have an order of magnitude larger intensity than delayed neutrons making them easier to detect. Additionally, while the same fission products can be produced by different isotopes, it has been found that the average mass of the lower mass fission fragment scales almost linearly with the material mass, allowing identification of the parent material by examining the ratio of various daughter products [13].

In an active interrogation scheme, fission can be induced by photons (γ,f) or neutrons (n,f). Nuclear materials, specifically fissile and fissionable materials, have lower (n,f) reaction thresholds than normal materials. This difference can be exploited to use neutrons to activate only materials of interest. Thermal neutrons, and fast neutrons that thermalize in the cargo container, can be used to activate fissile materials, which are defined as materials that fission with thermal neutrons. Fissionable

materials, such as ^{238}U which has an (n,f) threshold of 1.5 MeV, can also be selectively activated. In active interrogation schemes that utilize low energy neutrons, the presence of fast fission neutrons can then be used as an indicator of special nuclear material [14]. The threshold for photoneutron reactions in ^{235}U, 5.3 MeV, and ^{239}Pu, 5.65 MeV, is also lower than most benign materials [15]. This allows selective activation of nuclear materials, provided the accelerator source generates photons of the correct energy, or is tunable.

An alternative to induced fission is NRF. NRF is a technique that uniquely identifies isotopes based on their nuclear energy levels through the capture and reemission of a photon in a nuclear energy level [16] [17]. Nuclear resonances in actinides at room temperature have spectral widths on the order of eV's [18] which enables unique identification of specific isotopes with high resolution gamma detectors. NRF techniques can incorporate transmitted photon measurements to directly observe absorption in the target material or indirectly observe absorption through florescence measurements of a reference material [19]. In the second case, a decrease in the NRF signal from the reference material, in combination with a knowledge of the total transmitted photon flux, gives a direct measurement of the amount of reference material in the interrogated container since they have the same resonances [20]. A major drawback of present photon accelerators is the broadband nature of bremsstrahlung photon sources, six orders of magnitude higher than NRF linewidths, which prevents efficient coupling of photon energy into nuclear resonances, increases the amount of dose delivered to the target for the same amount of induced signal, and creates a high background environment that can mask the NRF photons.

X-ray florescence works in a similar manner to NRF, however the highest energy levels that can be excited in the electron shell of a heavy ion are approximately 100 keV, limiting the transmission of the X-ray through container materials. In addition to the other nuclear reactions listed in Table 1.2, radiation sources can be used to

identify materials through other processes such as neutron transmission spectroscopy. Neutron transmission spectroscopy can be used to identify materials by observing the effects of scattering, both elastic and inelastic, on a known neutron spectrum. This technique requires short duration broadband neutron pulses which are suitable for neutron time-of-flight spectroscopy.

1.3 Conventional Accelerators

1.3.1 Photon Sources

Photons can be generated from energetic electrons which are accelerated electromagnetically. One of the most common methods of accelerating electrons is a Radio Frequency (RF) LINAC. A LINAC can operate at 100 kHz repetition rates, creating high power beams. The electron beams are used to produce bremsstrahlung photons by propagating them into a high-Z conversion target. Bremsstrahlung, or braking radiation, photons are produced as the electrons decelerate in the presence of an atomic potential and convert kinetic energy into photons. Bremsstrahlung spectra are continuous and exhibit shapes [21] that can be very roughly approximated as exponentially decreasing with higher energies. The maximum photon energy is the electron energy, and thus is tunable by adjusting the electron energy. Commercially available 9 MeV bremsstrahlung LINAC sources are utilized in some current cargo inspection systems [7].

Nuclear decay gamma sources, utilizing reactions such as ^{19}F(p,$\alpha\gamma$)^{16}O, have also been used as a source of energetic photons to induce nuclear reactions [22]. These sources provide monochromatic photon sources which can be very intense, however they lack energy tunability or directionality. While the narrow linewidth could be exploited for NRF, finding a source that overlaps nuclear resonance levels in multiple types of SNM has proven difficult.

1.3.2 Neutron Sources

The most common conventional neutron accelerators are D-D and D-T generators which take advantage of the reactions:

$$ {}^{2}_{1}D + {}^{2}_{1}D \rightarrow {}^{3}_{2}He + n \tag{1.2} $$

$$ {}^{2}_{1}D + {}^{3}_{1}T \rightarrow {}^{4}_{2}He + n \tag{1.3} $$

to generate energetic neutrons from low energy (few 100 keV) deuterons. Neutron energies can be tuned by accelerating the incident deuterons to higher energies as well as by sampling the beam at different angles.

Photon sources can also be used to create photoneutrons through (γ,n) reactions in materials such as heavy water (D_2O) or Be [23]. Consequently, high energy photon beams can produce directional neutron beams [24]. This is also an effective means of producing broadband neutrons. As an added benefit, photoneutron sources can perform interrogation with both neutrons and photons.

1.3.3 Current Research

New operational modes for existing accelerators are being investigated to improve their applicability to homeland security applications. Specifically, portability, dose reduction, large standoff distances, and efficient coupling into nuclear processes are desired qualities for active interrogation applications. Many of these qualities overlap. For instance, efficient coupling reduces the required interrogation power which reduces dose. Reduced dose then increases the portability of an accelerator as it reduces the

Table 1.3: A comparison of various accelerator sources. Each method generates either neutrons or gammas.

Method	Neutron Rate (n/s)	Photon Rate (γ/s)
T-T[25]	1×10^{11}	n/a
D-T[25]	1×10^{13}	n/a
D-D[25]	1×10^{9}	n/a
D-D (Mini)[26]	1×10^{5}	n/a
Compton Scattering[27]	n/a	5×10^{10}/ev/sr
^{19}F(p,$\alpha\gamma$)^{16}O[28]	n/a	$6 \times 10^{7}/\mu$C/sr
^{13}C(p,γ)^{14}N[29]	n/a	5×10^{8}
^{11}B(p,γ)^{12}C[25]	n/a	$1 \times 10^{5} - 1 \times 10^{6}$

amount of required shielding which has to be located with the accelerator. Recent results are summarized in Table. 1.3

Improved nuclear gamma sources have been developed that are suitable for active interrogation applications [28]. These sources take advantage of the ^{19}F(p,$\alpha\gamma$)^{16}O reaction and produce gammas with energies of 6.129, 6.917, and 7.117 MeV. These gammas have sufficient energy to activate many materials of interest without activating the majority of common cargo materials. Two notable exceptions to this are deuterium, which is present in natural water, and ^{13}C which have photoneutron thresholds of 2.22 MeV and 4.95 MeV, respectively. However these isotopes have not been shown to be a significant obstacle in current homeland security applications. An alternative source utilizes a ^{11}B(p,γ)^{12}C reaction to produce gammas with energies of 11.7 MeV [25]. This type of source has been estimated to be capable of providing greater than 10^5 γ/s.

Compact cyclotrons also offer an alternative to linear accelerators for the acceleration of protons. Cyclotrons capable of accelerating negative H ions to 1.8 MeV energies with 2.5 mA currents and a 0.7 m radius have been used to generate photons through ^{13}C(p,γ)^{14}N reactions[29]. This type of device has an inherent energy spread of ΔE/E = 8% which can be further reduced to 0.1% through the use of a delimiting diaphragm, at the cost of significant loss of beam power. This energy spread

reduces the Doppler shift of the γ-rays which maintains their naturally narrow line width. The loss of beam power can be compensated through the use of a storage ring to integrate charge.

In the area of neutron interrogation, high power axial D-D and D-T generators are being investigated which increase neutron production rates, eliminate exposed high voltage elements and utilize RF induction discharge to generate high plasma density deuterium and tritium sources [26]. Heating of the titanium (deuterium containing) target in a D-D generator leads to desorption of the deuterium, resulting in a decreased neutron flux. Cooling the beam target has been shown to reduce this effect and allow a neutron rate of 10^9 neutrons/s which is an increase in the yield by a factor of 10[25]. Additionally, a D-T generator has been developed with a very high neutron generation rate of 10^{13} neutrons/s. Miniature D-D and D-T generators with a millimeter radius, but reduced yields of 10^5 neutrons/s, have also been reported [26].

Alternatives to D-D and D-T generators are also being investigated. A broadband neutron source can be generated by ^{3}T(T,2n)^{4}He reactions which generate neutrons between 0 and 9 MeV with a neutron generation rate of 10^{11} neutrons/s. This type of neutron source could be used for radiography and absorption measurements, as well as neutron induced fission activation. In order to be able to use time-of-flight energy measurements, the source pulse duration has to be on the order of nanoseconds, which can be accomplished by sweeping the tritium beam across a collimator, achieving neutron pulse duration less than 4 ns [25].

Furthermore, low energy neutron beams are being investigated as a low dose source of interrogation for fissile materials [30]. Specifically, 60 keV neutrons can be produced by the negative Q value reaction:

$$ {}^{1}_{1}P + {}^{7}_{3}Li \rightarrow {}^{7}_{4}Be + {}^{1}_{0}n \tag{1.4} $$

which has the desirable property of producing neutron beams that are directed in a forward cone for proton energies near the 1.88 MeV reaction threshold, producing 20^o half-angle cones with incident proton energies of 1.89 MeV. A benefit of this approach is that prompt neutrons with energies greater than 60 keV can be used as an indicator of fissile material during the interrogating neutron pulse, provided pulse shape discrimination can be used to discriminate the gamma background [31]. The modest proton energy required for this neutron source is possible with a portable 1 meter RF quadrupole accelerator. The low neutron energy leads to significantly reduced penetration depths in hydrogenous materials, but maintains comparable depths in high Z materials.

1.4 Laser Plasma Accelerators

Research is also being performed to study the potential to use laser plasma accelerators as a source for active interrogation techniques. The development of Chirped Pulse Amplification (CPA) in 1985[32] has led to the development of lasers that produce electric fields of >100 TeV/m at their focus. While these fields are not suitable for directly accelerating particles, as their orientation is perpendicular to the k-vector, or direction of travel, of the pulse, they rapidly ionize matter and form a plasma. Coupling of the laser into this plasma can generate a quasi-static TeV/m electric field which is capable of accelerating particles with gradients three to four orders of magnitude higher than conventional accelerators. Additionally, since the extreme fields generated by CPA lasers are a result of compressing the laser pulse to 10's of femtoseconds, very short time duration bursts of radiation can be generated

with a high instantaneous flux. The potential also exists for beam properties, such as monoenergetic Compton photons, which are not currently available from conventional accelerators. These qualities offer an exciting alternative technology to conventional accelerators.

1.4.1 Photon Experiments

The interaction of an ultra-intense ($I\lambda^2 > 1.387 \times 10^{18}$ W/cm$^2/\mu$m) laser with a gas, as first proposed by Tajima and Dawson [33], can accelerate electrons through wakefield acceleration. In wakefield acceleration the ponderomotive potential of the laser accelerates the light electrons away from the laser pulse, leaving the heavier positive ions behind which create a strong electrical potential inside a plasma "bubble". As the electrons are accelerated back toward the positive space charge a trailing plasma wave is formed behind the laser pulse. For sufficient densities and laser parameters, non-linear growth of this plasma wave leads to wave breaking and injection of electrons into the bubble where they can ride the potential behind the laser pulse and be accelerated to MeV-GeV energies in centimeters[34]. In addition to the short acceleration distance, wakefield generated electron beams have the desirable quality of milliradian beam divergence [35].

While this type of beam could serve as a replacement for a LINAC, the demonstration of quasi-monoenergetic electron beams [36] [37] [38] has generated interest in all optical table top accelerators for Compton gamma sources. The desired beam characteristics for NRF are high spectral intensity ($\frac{\gamma' s}{sr*eV*t}$), a tunable energy range, narrow bandwidth, and linear polarization [17]. When a laser pulse collides with a relativistic electron bunch the photons are upshifted by a factor of $4\gamma^2$ with an emission cone angle of $1/\gamma$, where γ is the Lorentz factor of the electrons [27]. If the laser and electron bunch have narrow bandwidths the generated photon beam is also narrow bandwidth. Stable wakefield electron beams with energies ranging between

100 and 800 MeV, 5% energy spreads, and mrad divergences have been demonstrated [39]. For the photon source, Nd:YAG lasers are a mature laser technology capable of providing narrow linewidths ($<nm$) and joule energies in relatively short duration 10 ps pulses. Simulations have predicted very high gamma spectral fluxes of 10^{11} photons/(eV*s*sr) in all optical Compton sources [27]. Additionally, the polarization of the laser beam and resulting photons can be controlled through the use of waveplates. Efforts to demonstrate all optical Compton scattering are underway at several laboratories [40]. In one early result, a modified scheme using a plasma mirror to reflect the electron generating laser pulse back into the driven electron beam has demonstrated broadband photons with energies of up to hundreds of keV [41]. While the use of Compton sources has been shown using large facility scale conventional electron accelerators[42], an all optical laser Compton scattering source is a potentially enabling technology for active interrogation due to its reduced size.

Monoenergetic or broadband wakefield accelerated electrons can also be used to generate photons through the more traditional approach of creating broadband bremsstrahlung photons through a high Z conversion target. Proof-of-principle experiments demonstrated (γ,3n) reactions in Pb and Cu indicating measurable activation with photons > 25 MeV [43]. Photofission of ^{238}U has been demonstrated using bremsstrahlung photons from wakefield generated 100-150 MeV electrons which generated 3×10^7 electrons/s [44]. Similar results, but with a lower efficiency, have also been obtained using bremsstrahlung photons produced during a solid target interaction [45] [46]. An order of magnitude higher efficiency in the conversion of laser energy to fission events has been demonstrated through the use of monoenergetic electron beams when compared to broadband electron beams.

In addition to "replacement" applications where laser accelerated electrons substitute for electrons from more traditional accelerators, the potential exists for new interrogation methods that are not practical with conventional accelerators. The

production of photons from the betatron oscillations of electrons inside the plasma wakefield bubble has been shown to generate broadband photon spectra in the keV range [47]. This method utilizes the naturally occurring transverse focusing fields of the plasma bubble to act as a wiggler, bypassing the requirement of an external magnetic device. The generated photons are spatially coherent with an ultrashort duration, raising the possibility of phase contrast imaging if higher energy photons can be created, which could provide high resolution information about the contents of an interrogated container.

Wakefield electron beams could also be used to generate exotic particles, with rest masses of 100's of MeV or greater, for the detection of SNM. Through the use of preformed plasma contained in capillary waveguides, beam energies of 1 GeV have been demonstrated in 3.3 cm [48]. Recently, electron energies of up to 4 GeV have been demonstrated in experiments without the use of a capillary waveguide[49]. The acceleration of high energy electrons has also been demonstrated through staged acceleration [50]. This approach is being investigated for the generation of 10 GeV electron beams [51].

1.4.2 Neutron Experiments

The direct acceleration of neutrons from laser plasma interactions is not possible due to the neutron's lack of charge. Instead, laser neutron accelerator schemes usually mimic traditional sources by accelerating light ions and initiating nuclear reactions to generate neutrons from light ions. While the technique is similar, laser based neutron sources can have higher instantaneous neutron production rates as they are not limited to ion current densities below the converter target damage threshold. Laser based acceleration of ions is typically accomplished through Target Normal Sheath Acceleration (TNSA) [52], which will be discussed further in section 2.3.1. In this mechanism energetic electrons are generated through the absorption of laser

energy in the short scale length plasma that typically exists on the front side of a solid target laser interaction. These electrons then propagate through the target, but are unable to fully escape the electric potential resulting from the charge separation, and establish a quasi-static electric sheath field at the interface between the solid target and the vacuum. This sheath field provides a potential through which ions are often accelerated up to energies of approximately 50 MeV[53]. TNSA produces exponential ion spectra up to a maximum proton energy. Although, TNSA beams start with a short pulse duration, they slightly spread out in time as a result of velocity differences. However, typical ion pulse durations are still on the order of 100's of ps which is sufficient for time-of-flight spectroscopy techniques. Ions can also be accelerated from the front side of the target, known as Front Side Acceleration (FSA)[54], as a result of the electric potential generated by the acceleration of electrons out of the focal spot. Two neutron generation schemes are possible using the two acceleration mechanisms. In FSA the ions can undergo nuclear reactions inside the bulk of the target material, allowing the target to act as a neutron converter. Alternatively, TNSA requires the ions, which are accelerated from the back of the target, to collide with a second target in a so called pitcher-catcher configuration.

Several experimental results are summarized in Table 1.4. The generation of 7×10^7 neutrons per shot has been demonstrated in bulk C_8D_8 through D-D reactions [59]. A pitcher-catcher configuration using a CH target with a LiF catcher demonstrated the production of 3×10^9 neutrons in a single shot with 69 J of laser energy [55]. A similar experiment using Cu and LiF has inferred the production of 1.8×10^9 neutrons in a single shot with 140 J of laser energy [57]. Neutrons with energies greater than 15 MeV have been reported using the ^{7}Li(d,n)^{8}Be reaction, which has the benefit of a 15 MeV Q value [56] [65].

Neutron generation through nuclear reactions with ions other than protons are typically limited to bulk target configurations. This is a result of proton rich surface

Table 1.4: A comparison of various laser neutron sources. In results reported by Lancaster *et al.* - Pretzler *et al.* the neutrons were generated through a two-step process where ions were accelerated and then a nuclear reaction produced the neutron. Alternatively, Fritzler *et al.*, Taylor *et al.*, and Ditmire *et al.* reported laser fusion schemes. The lower laser energy and high repetition rate results represent progress toward a practical accelerator for homeland security applications. All results were demonstrated on single shot lasers except for Prezler *et al.* which was performed on a 10 Hz laser. The calculation by Taylor *et al.* relies on the development of Inertial Fusion Energy drivers over the next 20 to 30 years.

Publication	Flux (n/sr/shot)	Laser Energy (J)	Intensity (W/cm^2)	Reaction	Year
Lancaster *et al.*[55]	4×10^8	69	3×10^{19}	^{7}Li(p,n)^{7}Be	2004
Higginson *et al.*[56]	8×10^8	360	2×10^{19}	^{7}Li(d,n)^{8}Be	2011
Higginson *et al.*[57]	1.4×10^8	140	1×10^{20}	^{7}Li(p,n)^{7}Be	2010
Willingale *et al.*[58]	5×10^4	6	$(1-3) \times 10^{19}$	^{2}d(d,n)^{3}He	2011
Norreys *et al.*[59]	7×10^7	20	1×10^{19}	^{2}d(d,n)^{3}He	1998
Roth *et al.*[60]	1×10^{10}	80	$(1-10) \times 10^{20}$	^{9}Be(d,n)^{10}B	2013
Pretzler *et al.*[61]	3×10^8	0.2	1×10^{18}	^{2}d(d,n)^{3}He	1998
Fritzler *et al.*[62]	1×10^6	62	2×10^{19}	^{2}d(d,n)^{3}He	2002
Ditmire *et al.*[63]	5×10^9	30×10^3	n/a	^{2}d(d,n)^{3}He	1999
Taylor *et al.*[64]	1×10^{19}	2×10^6	n/a	^{3}t(d,n)^{4}He	n/a

contaminants that are present on all target materials, in the absence of specialized cleaning techniques, which are preferentially accelerated due to their low mass and act to neutralize the sheath field, limiting the acceleration of heavier ions. A comparison between pitcher-catcher and bulk acceleration schemes for the same laser demonstrated a higher D-D reaction yield for bulk targets, attributed to the reduced stopping power for the deuterons in the heated bulk target as well as the parasitic effects on acceleration of the proton contaminant [58].

Alternative ion acceleration schemes have also been proposed and investigated. Radiation pressure acceleration [66][67] holds the promise of monoenergetic beams, although significant effort to observe this acceleration mechanism has proven unsuccessful to date [68]. Recently, collisional shocks in gas jets have demonstrated proton acceleration to up to 20 MeV with 1% energy resolution using a CO_2 laser [69] [70]. While high power CO_2 lasers, which operate at 10 μm wavelengths, are frequently

used for industrial machining and cutting applications, commercially available lasers are not capable of producing the short pulses needed for this acceleration mechanism. Simulation scalings suggest that applying this mechanism to lasers that operate in the visible or near-IR frequencies, and can achieve higher intensities, could raise the proton energy to hundreds of MeV while maintaining the high beam quality.

1.4.3 High Repetition Rate Accelerators

One of the main obstacles facing the implementation of laser based active interrogation is that many current high intensity lasers operate in a single shot mode with minutes to hours between shots, which is insufficient for active interrogation applications. In response to this, research has begun at the University of Michigan Center for Ultrafast Optical Science (CUOS) to demonstrate the feasibility of operation at higher repetition rates. The High Energy Repetitive CUos Laser System (HERCULES) and λ^3 lasers support 30 - 40's fs compressed pulse durations and can achieve relativistic intensities with millijoules to joules of energy, which leads to generation of less heat in the laser crystals allowing higher repetition rates. Demonstration of photofission of ^{238}U has already been performed on HERCULES, as previously mentioned. The λ^3 laser has been used to generate narrow energy spread electron beams [71] and 0.5 MeV protons [72] from solid target interactions at 500 Hz . The generation of low energy neutrons has also been demonstrated through a D-D reaction with a 10 Hz laser system [61]. Developing a better understanding of the generation of radiation with laser based accelerators and demonstrating these techniques on the high repetition rate HERCULES and λ^3 lasers is the focus of this thesis.

1.5 Thesis Overview

This thesis describes work done to systematically study the generation of radiation with CPA high intensity lasers for the purpose of homeland security. After an intro-

duction to the theory of laser plasma interactions and the mechanisms for radiation generation in Chapter II, a description of the laser facilities and experimental diagnostics will be given in Chapter III. A study of electron acceleration and bremsstrahlung generation on the λ^3 laser will be presented in Chapter IV. An experiment investigating the effect of mass limited targets will then be covered in Chapter V, which yields insight into acceleration of the ions used to generate neutrons in Chapter VI. A summary of the results and their implications for homeland security applications, as well as an outlook for the future, will then be given in Chapter VII.

CHAPTER II

Theoretical Background

The study of laser plasma accelerators begins with lasers capable of delivering intensities high enough to rapidly ionize material and create a plasma. The plasma responds to the extreme laser fields, coupling the laser energy into particle motion. A wide variety of physical phenomenon are possible depending on the properties of both the laser and plasma. In this thesis, the experiments investigate the interaction of ultra intense $>10^{18}$ W/cm^2 lasers with solid targets.

2.1 Laser Physics

Ultra intense lasers were first developed in the 1990's. Until that point, laser intensity had been limited to approximately 10^{15} W/cm^2 by the damage threshold of optical materials and the practical limitation of beam sizes. The development of CPA [32] allowed this limitation to be bypassed by temporally expanding a pulse, lowering its power, and allowing further amplification. The combination of spatial and temporal expansion and subsequent recompression has allowed lasers with focused intensities of 10^{22} W/cm^2 [73].

2.1.1 Chirped Pulse Amplification

CPA takes advantage of the large bandwidth of some laser amplification materials, such as Ti:Sapphire, to generate a high power, short duration pulses. The temporal envelope of a perfectly compressed optical pulse can be decomposed into its spectral components through a Fourier transform. This establishes a relationship between the pulse duration, τ, and spectral bandwidth, $\Delta\omega$, which is described by the time-bandwidth product

$$\Delta\omega \cdot \tau \geq 2\pi C_B \tag{2.1}$$

where C_B is 0.441 for a Gaussian pulse. For a 30 fs pulse this requires a laser bandwidth of 30 nm for a central wavelength of 800 nm, typical of Ti:Sapphire lasers. In the more general case of a pulse that has a linear chirp, i.e., the frequency of the pulse changes linearly with time, the pulse can be described by

$$\mathbf{E(t)} = \mathbf{E_0} e^{-at^2} e^{i(\omega_0 + bt)t} \tag{2.2}$$

where $\frac{1}{a} = \frac{\tau^2}{2ln(2)}$ and b is the linear chirp. The time-bandwidth product becomes

$$\Delta\omega \cdot \tau = 2\pi C_B \sqrt{1 + \left(\frac{b}{a}\right)^2} \tag{2.3}$$

where for $b = 0$ Eqn. 2.1 is recovered, and for $b \neq 0$ the pulse duration increases for a fixed bandwidth. Thus, introducing a chirp to an ultrashort pulse stretches the pulse envelope in time, lowering its power. This allows a stretched laser pulse to be amplified to energies that would otherwise destroy optical components. After

the stretched pulse has been amplified, the chirp can be removed, recovering the ultrashort pulse duration.

While it is possible to chirp a pulse by means of passage through material, the most convenient method involves the use of parallel optical grating pairs. The group delay dispersion of a Treacy compressor[74] is given by

$$\frac{d^2\phi}{d\omega^2} = -\frac{G\lambda}{\pi c^2}\frac{(\lambda/d)^2}{\left[1-\left(sin(\gamma)-\frac{\lambda}{d}\right)^2\right]^{3/2}} \tag{2.4}$$

where the variables are as indicated in Fig. 2.1. The group delay dispersion is always negative, which compensates for normal dispersion in typical optical materials at 800 nm. Alternative compressor schemes, such as the Martinez compressor [75], allow both negative and positive dispersion, and can be used to initially stretch the pulse. CPA is used on both the HERCULES and λ^3 lasers.

2.1.2 Nonlinear Optics

As laser intensity increases, but before it begins to strip electrons from atoms, the electric field of the laser pulse can modify the material it passes through. This gives rise to a number of nonlinear optical effects. Some effects, such as self-focusing, can have disastrous consequences causing damage in optical components through unintended ionization of component materials. When controlled, however, nonlinear optics produces a range of effects which can be used to rotate laser polarization, control gain, and generate bandwidth, among other things. Several examples of nonlinear optics will be found in Chapter III and the theoretical background will be introduced below.

Maxwell's equations serve as the basis for the study of electricity and magnetism.

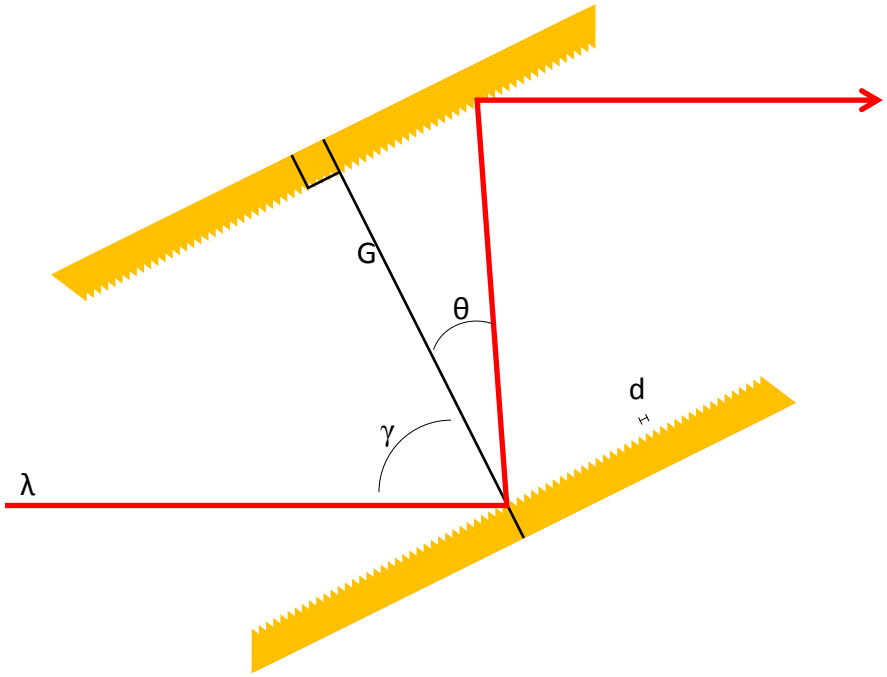

Figure 2.1: Schematic of 1 set of gratings in a parallel Treacy compressor, as used in the HERCULES laser. G is the grating separation, d is the grating line spacing, and the angles γ and θ are as indicated.

In SI units in a material they take the form

$$\nabla \cdot \mathbf{D} = \rho \tag{2.5a}$$

$$\nabla \times \mathbf{E} = -\frac{\partial \mathbf{B}}{\partial t} \tag{2.5b}$$

$$\nabla \cdot \mathbf{B} = 0 \tag{2.5c}$$

$$\nabla \times \mathbf{H} = \mathbf{J} + \frac{\partial \mathbf{D}}{\partial t} \tag{2.5d}$$

with the electric displacement $\mathbf{D} = \epsilon \mathbf{E}$ and $\mathbf{B} = \mu \mathbf{H}$. The wave equation is found by taking the curl of Faraday's law, Eqn. 2.5b, and combining it with Ampere's law, Eqn. 2.5d, in a nonmagnetic material, $\mathbf{B} = \mu_0 \mathbf{H}$, with no free charge and no free current:

$$-\nabla^2 \mathbf{E} + \mu_0 \frac{\partial^2 \mathbf{D}}{\partial t^2} = 0. \tag{2.6}$$

The electric displacement can be recast as

$$\mathbf{D} = (1 + \chi)\epsilon_0 \mathbf{E} \tag{2.7}$$

where χ is the electric susceptibility of the medium. Substituting Eqn. 2.7 into Eqn 2.6 yields

$$-\nabla^2 \mathbf{E} + \frac{1}{c^2} \frac{\partial^2 (1 + \chi)\mathbf{E}}{\partial t^2} = 0. \tag{2.8}$$

In free space $\chi = 0$ and the wave equation for free space is obtained. In a linear material, the refractive index, $n^2 = (1 + \chi)$, can be pulled out of the time derivative

and leads to a modification of the wave group velocity, $v_g = c/n$. The more interesting case occurs when the electric susceptibility of the medium is altered by the electric field of the wave. In this case, the wave equation becomes nonlinear. The nonlinear term can be expanded as a power series

$$\chi \mathbf{E} = \chi^{(1)}\mathbf{E} + \chi^{(2)}\mathbf{E}^2 + \chi^{(3)}\mathbf{E}^3 + ... \tag{2.9}$$

where $\chi^{(1)}$ is the linear susceptibility and $\chi^{(2)}$ and $\chi^{(3)}$ are the second- and third-order nonlinear susceptibilities. Substituting Eqn. 2.9 into Eqn. 2.8 produces

$$-\nabla^2\mathbf{E} + \frac{n^2}{c^2}\frac{\partial^2\mathbf{E}}{\partial t^2} = -\frac{1}{c^2}\frac{\partial^2\left(\chi^{(2)}\mathbf{E}^2 + \chi^{(3)}\mathbf{E}^3 + ...\right)}{\partial t^2} \tag{2.10}$$

which has the linear wave equation on the left hand side and a nonlinear driving term on the right hand side. This serves as the starting point for nonlinear optics.

One of the most straight forward examples of nonlinear optics is found in second harmonic generation, which is a $\chi^{(2)}$ effect. Keeping the $\chi^{(2)}$ term in Eqn. 2.10 and examining the case of a slowly varying amplitude wave of the form $\mathbf{E}_n(z,t) = \mathbf{E}_n(z)e^{(i(k_n z - \omega_n t))}$, a driving wave $\mathbf{E_1}$ interacting with itself creates a second wave $\mathbf{E_2}$ such that

$$-\nabla^2\mathbf{E_2} + \frac{n^2}{c^2}\frac{\partial^2\mathbf{E_2}}{\partial t^2} = -\frac{\chi^{(2)}}{c^2}\frac{\partial^2||\mathbf{E_1}||^2}{\partial t^2}. \tag{2.11}$$

Taking the second order time derivative on the right hand side and using the product rule to expand the Laplacian, and assuming the second order derivative of $\mathbf{E_2}(z)$ can be ignored yields

$$\frac{\partial \mathbf{E_2}(z)}{\partial z} = \frac{i2\omega^2\chi^{(2)}}{k_2^2 c^2}||\mathbf{E_1}(z)||^2 e^{(i\Delta k)} \tag{2.12}$$

where $\Delta k = 2k_1 - k_2$ is the phase matching term.

This example illustrates a few characteristics of nonlinear optics. Phase matching between the driving wave, or waves, and the generated wave often constrains the wave growth, and limits the number of materials capable of supporting nonlinear effects. Birefrigent materials, often crystals, can be used to phase match waves through careful orientation of the waves with respect to the crystal axis. The growth of the generated wave is proportional to the strength of the nonlinear susceptibility and the magnitude of the driving wave or waves. Also, the magnitude of the generated wave increases with interaction length. The interaction length is limited by the length of the nonlinear material or the accumulation of phase mismatch, which ultimately leads to deconstructive interference when the phase mismatch reaches 180^o. In Chapter III several applications of nonlinear optics will be discussed.

2.2 Laser Plasma Physics

As laser intensity further increases, electrons are ionized creating a plasma. For conditions relavent to the upcoming discussions, the dominant ionization mechanism is field ionization. In field ionization the electric field of the laser modifies the atomic potential such that electrons can quantum mechanically tunnel through the potential barrier and escape the atomic potential. Once the plasma has formed, the laser couples into the plasma.

2.2.1 Normalized Vector Potential

An extremely usefull quantity in high intensity laser physics is the normalized vector potential

$$\mathbf{a_0} = \frac{e\mathbf{E}}{m_e c\omega}. \tag{2.13}$$

This quantity relates the energy gained by an electron, $e\mathbf{E} \cdot l$ over a distance $l = c/\omega$, to the rest mass of the electron, m_0c^2. In practical units this equates to

$$a_0 = \sqrt{\frac{I\lambda^2}{1.387 \times 10^{18}}}. \tag{2.14}$$

with I expressed in W/cm^2 and λ expressed in μm. For 800 nm light this means intensities over 2.1×10^{18} W/cm^2 are considered relativistic.

2.2.2 Ponderomotive Force

As electrons oscilate in an intense laser pulse they can traverse the spatial extent of the pulse and experience different field strengths. As a result, an electron that is acclerated out of the peak of a pulse may experience a weaker restoring field during the second half of the laser cycle. This leads to a net motion of electrons out of the region of highest pulse intensity, as a result of the ponderomotive force. The ponderomotive force on an electron can be derived with the convective Lorentz force equation

$$\mathbf{F} = m\left(\frac{\partial \mathbf{v}}{\partial t} + \mathbf{v} \cdot \nabla \mathbf{v}\right) = q(\mathbf{E} + \mathbf{v} \times \mathbf{B}) \tag{2.15}$$

and a generic oscillating electric field of the form $\mathbf{E} = \mathbf{E_0} sin(kz - \omega t)$ where $\mathbf{E_0}$ is the slowly varying envelope and ω is the laser frequency. Ignoring the magnetic field and breaking the electron velocity into a fast oscillation and a slow drift, $\mathbf{v} = \mathbf{v_f} + \mathbf{v_s}$ yields

$$\frac{\partial \mathbf{v_f} + \mathbf{v_s}}{\partial t} + (\mathbf{v_f} + \mathbf{v_s}) \cdot \nabla (\mathbf{v_f} + \mathbf{v_s}) = \frac{q\mathbf{E_0}}{m} sin(kz - \omega t). \tag{2.16}$$

This equation can be simplified by taking advantage of the fact that the fast velocity component, due to the laser, has a much larger amplitude than the slow component, $\mathbf{v_f} >> \mathbf{v_s}$, and also has a larger amplitude than the gradient, $\mathbf{v_f} >> \nabla \mathbf{v_f}$, since the fast electron oscillations have a small spatial gradient. Thus, evaluating Eqn. 2.16 to lowest order yields

$$\frac{\partial \mathbf{v_f}}{\partial t} = \frac{q\mathbf{E_0}}{m} sin(kz - \omega t) \tag{2.17}$$

which can be solved to find

$$\mathbf{v_f} = \frac{-q\mathbf{E_0}}{\omega m} cos(kz - \omega t). \tag{2.18}$$

Subsituting Eqn. 2.17 into Eqn. 2.16 and keeping the next highest order term, $\nabla \mathbf{v_f}$, yields

$$\frac{\partial \mathbf{v_s}}{\partial t} + (\mathbf{v_f}) \cdot \nabla (\mathbf{v_f}) = 0. \tag{2.19}$$

The slow component of the electron velocity can then be found by averaging over

a laser period, denoted by <>, and rewriting the second term using the chain rule such that

$$\frac{\partial \mathbf{v_s}}{\partial t} = -\frac{1}{2}\nabla \left\langle \mathbf{v_f} \right\rangle^2 . \tag{2.20}$$

Substituting Eqn. 2.18 into Eqn. 2.20 and taking the time average yields the ponderomotive force

$$m\frac{\partial \mathbf{v_s}}{\partial t} = \frac{-q^2}{4m\omega^2}\nabla ||E_0||^2. \tag{2.21}$$

The relativistically corrected ponderomotive force[76] can be expressed in terms of the normalized vector potential as

$$F_p = -\frac{m_e c^2}{\langle\gamma\rangle}\nabla \left\langle \frac{a^2}{2} \right\rangle \tag{2.22}$$

where, for a linearly polarized plane wave, $\gamma = 1 + \frac{a^2}{2}$, and $\langle a \rangle = \frac{a_0}{2}$. The ponderomotive energy is then found to be

$$U = m_e c^2 (\gamma - 1) \tag{2.23}$$

which will be a useful quantity in the discussions to follow.

2.2.3 Laser Absorption Mechanisms

The response of a plasma to an electromagnetic wave is given by the dispersion relation

$$\omega_0^2 = \omega_p^2 + (k_0 c)^2. \tag{2.24}$$

where $\omega_p = \sqrt{\frac{e^2 n_e}{\epsilon_0 m_e}}$ is the plasma frequency. The critical density is defined as the plasma density required for the plasma frequency to equal the laser frequency. If the plasma frequency exceeds the laser frequency then k becomes negative and the wave becomes evanescent. If the laser pulse is normally incident upon a plasma with a slowly increasing density, such as is often the case in laser plasma interactions, the pulse propagates through the low density plasma until it reaches the critical density and reflects off of the critical surface.

In plasmas with gentle density gradients, one of the possible laser absorption mechanisms is resonance absorption [77]. Resonant absorption occurs when the laser coherently drives a plasma wave at the critical surface. As the plasma wave grows in amplitude the wave becomes nonlinear and breaks, accelerating electrons. For P polarized light, i.e. light oriented with a component of the electric field vector along the target normal direction, the resonantly driven wave accelerates electrons into the target. For a pulse to be P polarized it must be obliquely incident on the target. A laser pulse that is obliquely incident to the plasma gradient, at an angle θ, will not reach the critical surface and instead become evanescent at the plasma density $n_e = n_c cos^2(\theta)$[77]. However, resonance absorption can still occur, as the laser can couple to the critical surface through the evanescent wave.

While solid target laser plasma interactions typically have a plasma gradient, which is generated by the presence of light ionizing the target before the arrival of the main pulse, ultrafast lasers with high laser contrast, discussed further in Section 3.3, can interact with solid targets that have high density gradients. If the density gradient is high enough that an electron oscillating in the laser field travels far past

the critical surface then the electron will not be decelerated by the electric field of the laser during the second half of the wave cycle. As a result, electrons from the target surface are accelerated into the target with every laser cycle, resulting in an acceleration mechanism known as Brunel[78], or vacuum heating. As with resonance absorption, Brunel heating requires obliquely incident light with P polarization. The optimum angle of incidence is given by the maximum of the absorption fraction[79]

$$\eta_a = \frac{f^2}{\pi} \frac{sin^2(\theta)}{cos(\theta)} \tag{2.25}$$

where $f = 1 + \sqrt{1 - \eta_a}$, which is found near 70^0.

At normal incidence, the electric field oscillates parallel to the plane of the target surface, preventing electrons from being accelerated into the target in the preceding mechanisms. However, for ultra intense laser pulses, the magnetic field is strong enough to rotate the electron velocity vector. This absorption mechanism can be seen by examining the Lorentz force equation, specified earlier in Eqn. 2.15. The electric field of the laser accelerates an electron along the electric field direction. This velocity is perpendicular to the magnetic field vector, and the curl of these two vectors lies in the direction of propagation of the light pulse, i.e. the forward direction. In an analogous situation to Brunel heating, if an electron is accelerated in the forward direction through a high plasma density gradient, the second half of the optical cycle does not decelerate the electron, resulting in the $J \times B$ heating absorption mechanism [79]. The energy of electrons accelerated by this mechanism is given by the ponderomotive potential of the laser.

2.2.4 Scaling Laws

As laser intensity increases, electrons are accelerated to higher energies by the stronger fields. The relative scaling between electron energy and laser intensity is a subject of much interest in the field of laser plasmas. Many theoretical and experimental scaling laws have been developed, but two of the simplest, and most common are ponderomotive, or Wilks, scaling [80]

$$T_{Wilks} = 511(\sqrt{1 + a_0^2} - 1) \quad \text{(keV)} \tag{2.26}$$

and the empirical Beg scaling [81]

$$T_{Beg} = 215(a_0)^{2/3} \quad \text{(keV)}. \tag{2.27}$$

Ponderomotive scaling was first observed in Particle-In-Cell (PIC) simulations and is approximately the ponderomotive energy, as found in Eqn. 2.23. For large a_0 the scaling becomes $m_0c^2a_0$, which is the "un-normalized" vector potential. The simplicity of this model suggests it is unlikely to adequately describe experimental results, but it has proven to be a useful scaling. In practice it often overestimates the electron energy, as it incorporates no energy loss mechanisms.

Alternatively, Beg scaling is an empirical scaling based on results from a variety of picosecond pulse duration experimental results, across a variety of laser systems. Beg scaling differs from ponderomotive scaling primarily in that it scales more slowly with a_0. An analytical model has been developed [82] which matches Beg scaling and includes the effects of plasma shielding and backscattered light. While this scaling law has been successful at describing picosecond pulse duration interactions, different

scalings have been observed with shorter pulses.

An empirical scaling was developed for the λ^3 laser [83]

$$T_{\lambda^3} = 118(a_0)^{1.28} \quad \text{(keV)} \tag{2.28}$$

which scales much faster than Beg scaling. Around normalized vector potentials of 1, where the measurements were made, the λ cubed scaling is slower than ponderomotive scaling, due to the effects of the constants in Eqn. 2.26, but would exceed ponderomotive scaling for large a_0. This scaling is studied in Chapter IV and extended to higher intensities.

2.3 Ion Acceleration

In the preceding discussion, the normalized vector potential was used to quantify the strength of the laser intensity, and the resulting electron acceleration. If a similar quantity were used to measure the response of protons to the laser field the much larger proton mass would increase the relativistic threshold to over 10^{24} W/cm^2, which is not achievable with current laser technologies. Despite this fact, the acceleration of ions with laser plasma accelerators can be accomplished by using electrons as an intermediary between the laser and the protons. Several acceleration mechanisms exist, and even more have been proposed, but the predominant acceleration technique in laser plasma interactions is TNSA [52].

2.3.1 Target Normal Sheath Acceleration

In TNSA electrons accelerated from the front side of the target propagate through the target and exit the rear surface establishing a quasi-static electric field due to the charge separation. This field has a thickness of approximately a Debye length

$\lambda_d = \sqrt{\frac{\epsilon_0 k_B T_e}{n_e e_c^2}}$, where $T_e = T_h$ is the fast electron temperature, and a maximum electric field strength of $E_0 = \frac{T_h}{e\lambda_d}$ at the rear surface[84]. This field acts to ionize and accelerate ions from the rear surface in a direction normal to the surface plane. As ions are accelerated from the surface of the target they neutralize the field. Light ions, typically hydrogen, are accelerated to higher velocities, screening the heavier ions from the full field potential. Efficient acceleration of heavy ions can only be achieved by removing light ions from the target surface, and one such method will be discussed in Chapter VI.

The maximum proton energy at a time t is given by[84]

$$\varepsilon_{max} = 2E_0 \left[ln \left(\frac{2\omega_p t}{\sqrt{2exp^1}} \right) \right]^2 \tag{2.29}$$

where, for the final energy, t is of the order of the pulse duration. This illustrates the importance of understanding electron scaling laws, as T_e is proportional to the maximum ion energy.

2.4 Photon Generation

The generation of photons with laser plasma accelerators can be accomplished through many different mechanisms. The production of harmonics of the fundamental laser frequency has been shown to generate photons with 10's of eV [85]. The ionization of electrons also leads to photon generation through K-shell radiation and bremsstrahlung, which will be discussed below. Bremsstrahlung, and to a lesser extent K_α radiation, can result in photons with energies of 10's of keV to MeV which are appropriate for homeland security applications. Because they are generated by the energetic electrons accelerated during an ultra intense laser interaction, they also provide information about the energy, position, and direction of the electrons. In

Chapter V K_α radiation is used as a diagnostic of the electron propagation through targets with complex shapes, and in Chapter IV bremsstrahlung is characterized as potential radiation source, as well as a diagnostic for the electron behavior.

2.4.1 K-shell Radiation

Energetic electron beams can induce atomic electron transitions from the n=1 quantum level, or the K-shell, through collisional excitation and ionization. As electrons from higher levels replace the vacated inner shell electrons they radiate photons with energies up to hundreds of keV. Electrons that de-excite from the n = 2 quantum level to the n = 1 are known as K_α transitions, while electrons originating in the n = 3 quantum levels are referred to as K_β transitions, as shown in Fig. 2.2. Observation of K_α radiation in solid target laser-plasma interactions is particularly useful because it can penetrate solid density materials allowing measurements in the densest regions of plasmas. A material's K-edge is a sharp increase in photon absorption that occurs at the electron binding energy. This corresponds to the energy required to fully ionize a K-shell electron, and is always above the K_α energy. As a result, materials are relatively transmissive to their own K-shell radiation, allowing K-shell photons to serve as a diagnostic of the interior of materials. Additionally, K-shell radiation from the target material is easily discriminated from background sources since the K_α energy is specific to the material Z.

2.4.2 Bremsstrahlung Radiation

Bremsstrahlung radiation occurs when energetic electrons interact with the Coulomb field of an ion. As the electron is accelerated in the field, photons are produced with energies up to the initial electron energy. These photons beams can also have strong directionality, which is highly desirable for homeland security applications.

Understanding bremsstrahlung generation also provides insight into the electron

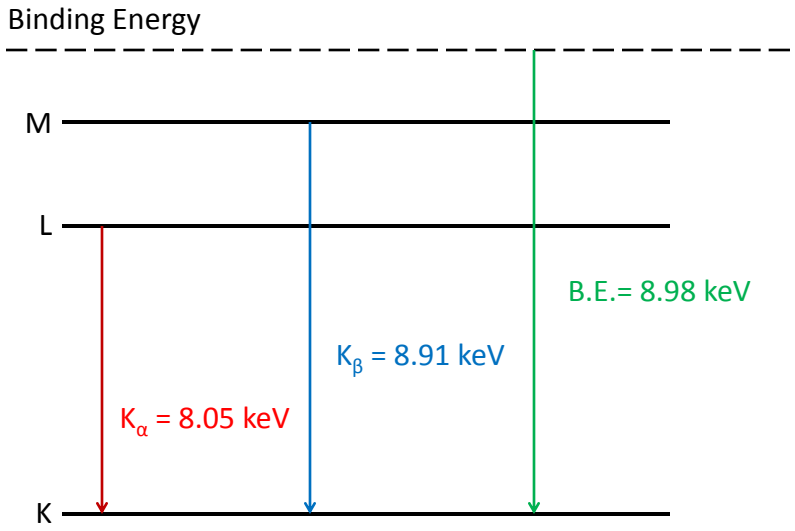

Figure 2.2: Energy level diagram of Cu showing the Cu K$_\alpha$, CuK_β and binding energy.

behavior. The quantity of interest for the experiments described in Section IV is the doubly differential cross section

$$\frac{d^2\chi}{d\omega d\Omega} = \frac{d\chi}{d\omega} \cdot \frac{d\chi}{d\Omega}. \tag{2.30}$$

The radiation cross section per unit frequency, taken from Jackson [86], of an electron of charge e, and initial velocity $c\beta$ in the Coulomb field of a massive, fixed, ion of charge Ze, is

$$\frac{d\chi}{d\omega} = \frac{Z^2e^2}{c}\left(\frac{e^2}{m_oc^2}\right)^2 \cdot \frac{1}{\beta^2}\int_{Q_{min}}^{Q_{max}} \frac{dQ}{Q} \tag{2.31}$$

or

$$\frac{d\chi}{d\omega} = \frac{Z^2e^2}{c}\left(\frac{e^2}{m_oc^2}\right)^2 \cdot \frac{1}{\beta^2} ln\left(\frac{Q_{max}}{Q_{min}}\right) \tag{2.32}$$

where eZ is the charge of a fixed point charge and

$$Q = |\mathbf{p}' - \mathbf{p} - \mathbf{k}| \tag{2.33}$$

is the magnitude of the momentum transfer between the electron and ion for an electron of initial momentum $\mathbf{p}$, final momentum $\mathbf{p}'$, and a photon with momentum $\mathbf{k}$. The range of the integral in Eqn 2.31 is defined by the minimum and maximum possible momentum transfer. In the nonrelativistic electron case Eqn. 2.33 can be simplified to

$$Q^2 = (\mathbf{p}' - \mathbf{p})^2 \tag{2.34}$$

by ignoring the photon momentum. The limits are then simply $Q_{max} = p + p'$ and $Q_{min} = p - p'$, such that

$$\frac{Q_{max}}{Q_{min}} = \frac{(\mathbf{p}' + \mathbf{p})}{(\mathbf{p}' - \mathbf{p})} = \frac{\left(\sqrt{E} + \sqrt{E - \hbar\omega}\right)^2}{\hbar\omega} \tag{2.35}$$

by taking advantage of the conservation of energy which sets $E = E' + \hbar\omega$. Plugging Eqn. 2.35 into Eqn. 2.32 yields the nonrelativistic bremsstrahlung cross section

$$\frac{d\chi_{NR}}{d\omega} = \frac{Z^2e^2}{c}\left(\frac{e^2}{m_oc^2}\right)^2 \cdot \frac{1}{\beta^2} ln\left[\frac{\left(\sqrt{E} + \sqrt{E - \hbar\omega}\right)^2}{\hbar\omega}\right]. \tag{2.36}$$

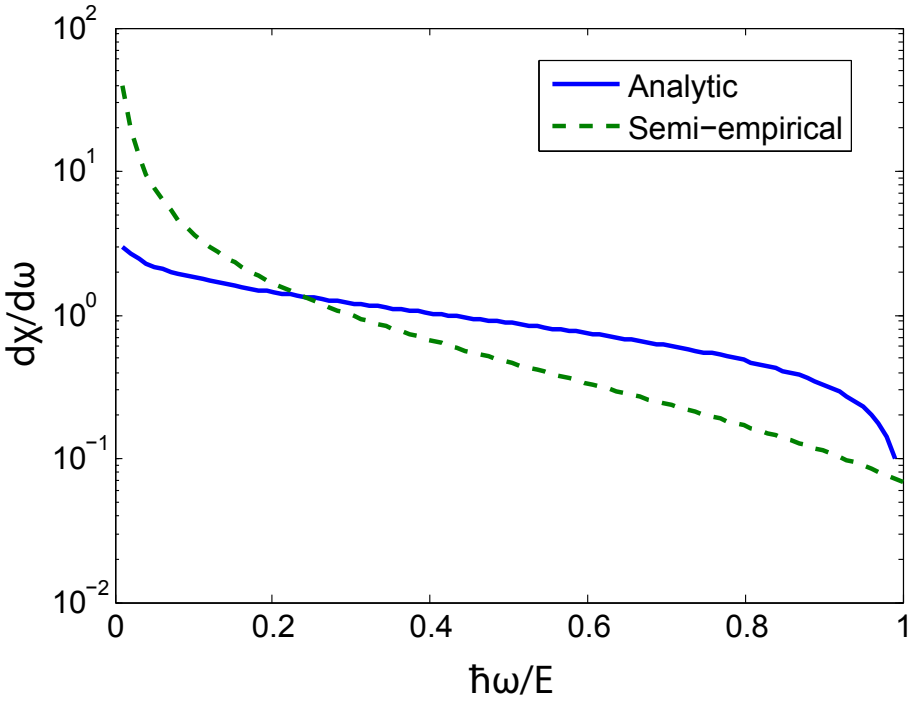

Figure 2.3: Plot of the nonrelativistic bremsstrahlung cross sections as a function of the ratio between the photon and electron energy. The analytic cross section peaks at low photon energies drops to zero for a photon energy equal to the electron energy. The semi-empirical cross section captures the overall behavior.

Eqn. 2.36 can be cast in terms of the ratio of the photon energy to the incident electron energy, $\frac{\hbar\omega}{E}$ which has been plotted in Fig. 2.3.

For relativistic bremsstrahlung the minimum and maximum Q values change because the photon momentum can no longer be ignored. The resulting limits are $Q_{max} = 2Mc$ and $Q_{min} = p - p' - k$ which yield a relativistic bremsstrahlung cross section of

$$\frac{d\chi_R}{d\omega} = \frac{Z^2e^2}{c}\left(\frac{e^2}{m_oc^2}\right)^2 \cdot \frac{1}{\beta^2} ln\left[\frac{E_{total}E'_{total}}{m_0c^2\hbar\omega}\right] \tag{2.37}$$

where E_{total} is the total energy, i.e. $E^2 = (pc)^2 + (m_0c^2)^2$. This equation retains a factor of order $\frac{\hbar\omega}{E}$ in the logarithm, although it can no longer be rewritten simply

in terms of this ratio. Eqn. 2.37 along with the angular term

$$\frac{d\chi_R}{d\Omega} = \left[\gamma^2 \frac{1+\gamma^4\theta^4}{(1+\gamma^2\omega^2)^4}\right] \tag{2.38}$$

gives the complete doubly differential radiation cross section. This equation is only valid in the limit that the electron energy before and after the collision is relativistic.

For the situation of interest in Chapter IV, the electron energy ranges between relativistic and nonrelativistic, as does the photon energy which was measured between 100 keV and 1 MeV. As an alternative approach, a semi-empirical description of bremsstrahlung radiation at the relevant energies has been developed by Findlay[87] with radiation cross sections described by

$$\frac{d\chi}{d\omega} \cong Z^2 \left(\frac{1}{\hbar\omega} - \frac{0.83}{E}\right) \tag{2.39}$$

and

$$\frac{d\chi}{d\Omega} \cong \frac{1}{\pi\theta_e^2(x)} exp\left(-\frac{\theta^2}{\theta_b^2}\right). \tag{2.40}$$

where $\theta_b = m_e c^2/(E + m_e c^2)$ is the width of the Gaussian describing the photon emission cone. These equations are plotted along with the analytic derivations in Fig. 2.3 and Fig. 2.4.

Many interesting qualities of bremsstrahlung emerge from the preceding equations. The total cross section scales with the material atomic number Z^2. As a result, efficient bremsstrahlung conversion occurs in high Z materials. The photon energy scales with the energy of the incident electron. Also, the direction of the emitted

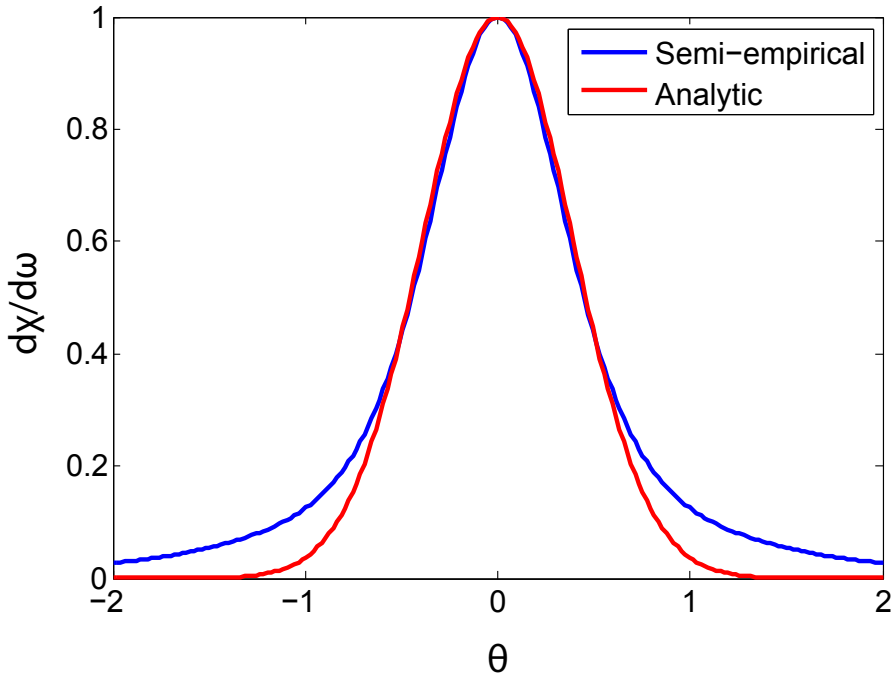

Figure 2.4: Plot of the analytic and semi-empirical formulations of the angularly resolved bremsstrahlung cross sections. The shape of the two curves deviate for large angles.

photons becomes more tightly constrained to the forward direction, as Eqn. 2.38 reduces to $\frac{1}{\gamma^2\omega^4}$ for large γ. This allows bremsstrahlung to be used as a diagnostic of electrons, since the highest energy bremsstrahlung photons will be aligned to the direction of the highest energy electrons. This relationship was exploited in Chapter IV, as will be discussed.

CHAPTER III

Methods

The experiments discussed in this dissertation were conducted at the laser facilities of the University of Michigan CUOS. The majority of work was performed on the ultra-high intensity HERCULES laser, while one experiment required the 500 Hz repetition rate λ^3 laser. Accordingly, most of diagnostics that will be discussed were employed in the HERCULES solid target experimental area. In many cases, the same diagnostics were used at both facilities, as will be noted. In addition to physical experiments, the use of simulations was critical to understand both the laser plasma interactions and meaning of the diagnostic signal.

3.1 Experimental Facilities

3.1.1 HERCULES Laser System

The HERCULES laser was a CPA Ti:Sapphire laser with 300 TW peak power [73]. The laser consisted of multiple amplification stages, each pumped by frequency doubled neodymium doped lasers, as shown in Fig. 3.1. The seed pulse was generated in a Kerr-lens modelocked oscillator which took advantage of self-focusing, as discussed in Section 2.1.2, as a result of the change in index of refraction of the Ti:Sapphire crystal. Light that did not undergo self-focusing was dumped from the laser cavity, while higher intensity short pulses were focused along the correct optical

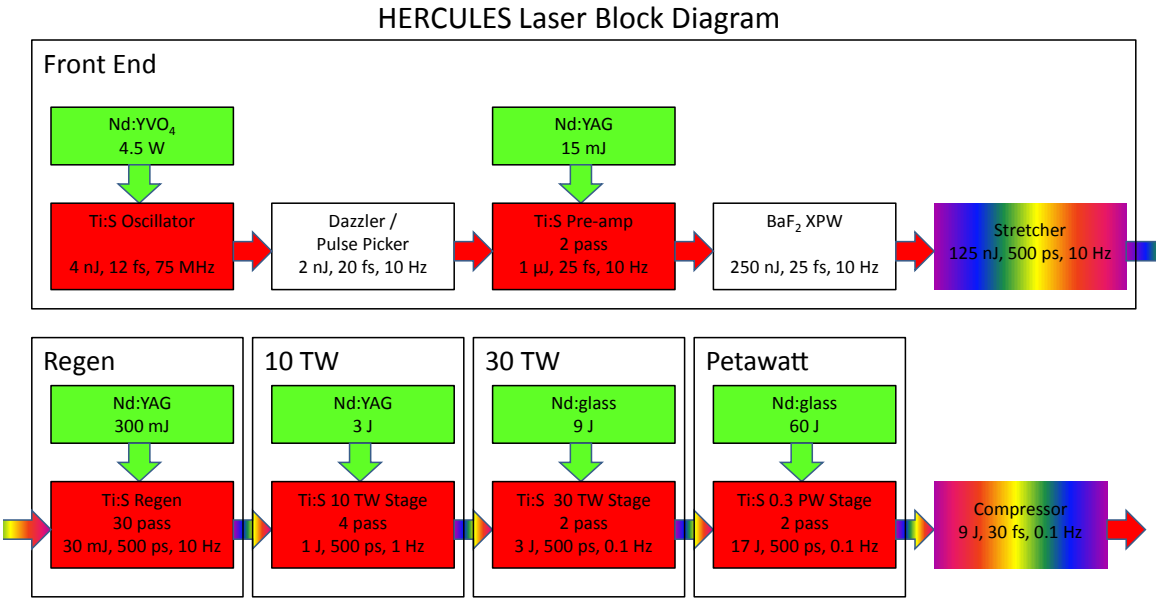

Figure 3.1: Block diagram of the HERCULES laser system. Red blocks represent 800 nm laser amplification stages, while green blocks represent 532 nm pump lasers. Each stage is identified by its colloquial name. The post-compressor pulse is directed to the target chamber.

path and experienced gain. The high amplification bandwidth of Ti:Sapphire (typically $50 - 60$ nm) allowed the generation of bandwidth-limited pulse durations of 12 fs at the oscillator.

Pulses from the 75 MHz oscillator were selected opto-electronically by a combination of polarizers and rotation of the pulse polarization through electrically induced birefringence, in Pockels cells, to reduce the pulse rate to 10 Hz The pulse was then amplified in the pre-amp stage to 1 μJ to achieve sufficient intensity for the Cross-Polarized Wave Generation (XPW) pulse cleaner. The XPW functioned similarly to a Pockels cell, except that an intensity dependent rotation of the pulse polarization was achieved through χ^3 four-wave mixing [88]. The pulse cleaning technique reduced Amplified Spontaneous Emission (ASE) by focusing the laser such that only the main pulse had sufficient intensity to rotate, while the pre-pulse was attenuated by the polarizer. In the HERCULES XPW two BaF_2 crystals were used to optimize the conversion efficiency. This was advantageous because the optimum conversion ef-

ficiency occurred when the angle between the laser and crystal polarization was 22.5 degrees. In the two crystal scheme the second crystal was then rotated to compensate for the polarization rotation from the first crystal.

The cleaned pulse was then stretched to 500 ps to allow further amplification without damaging laser optics, in the CPA scheme. The chirped pulse was then amplified of the order 10^6 times in energy during 10's of passes through the Regenerative Amplifier (Regen). Due to the large gain in the Regen, amplification of ASE from the first few passes of Regen was the dominant contribution to the laser pre-pulse. An additional benefit of the XPW technique was that use of the pre-amp stage reduced the required gain in Regen, and thus reduced the amplification of ASE in Regen. The nanosecond contrast, expressed as a ratio of the laser intensity nanoseconds before the main pulse to the main pulse, was 10^{-8} without XPW and 10^{-11} with XPW[89]. The laser contrast, and additional pulse cleaning techniques will be discussed in Section 3.3.

The laser pulse then entered three multi-pass Ti:Sapphire amplification stages known as 10 TW, 30 TW, and Petawatt, which were capable of amplifying the pulse to energies of 1 J, 3 J, and 17 J, respectively. Each amplification stage was protected from back reflections by a combination of spatial filters, Faraday isolators, and Pockels cells. The amplified chirped pulse was then recompressed in a Treacy compressor to a Full Width at Half Maximum (FWHM) pulse duration of 40 fs. The laser was delivered to the target chamber in a 10 cm beam polarized in the horizontal plane.

The recompressed pulse was not as short as the initial oscillator pulse, 12 fs, due to gain narrowing and high order pulse dispersion. While the system was originally designed to compensate for dispersion up to the fifth order, several changes have been made to system over its lifetime. However, this was only a minor contributor the pulse duration, as the main limitation was gain narrowing. Gain narrowing, or reduction of the pulse bandwidth, in the amplification stages occurred due to inefficient

pump power extraction at the low intensity leading and trailing edges of the pulse and pump depletion. Pump depletion affected the chirped pulse bandwidth as the longer wavelength light arrived at the gain crystal first, and experienced maximum gain, while the shorter frequencies were amplified less after the pump energy had been reduced. This effect led to red-shifting of the central frequency and reduction of the overall bandwidth. Additionally, because the temporal profile of the pulse mimics the Gaussian frequency profile, the highest power portion of the chirped pulse was around the central wavelength and the higher power led to more efficient amplification of central wavelengths, leading to bandwidth narrowing. The post-compressor bandwidth was typically 25 nm, as discussed in Section 3.2, which corresponded to a bandwidth limited pulse duration of 37 fs, although, as discussed in Section 3.2.2 the optimum pulse duration was measured to be 40 fs as a result of high order dispersion.

3.1.2 λ^3 Laser System

The λ^3 laser system was also a Ti:Sapphire CPA laser and shared many similarities with HERCULES. The primary difference between the two lasers was that λ^3 provided a smaller pulse energy, 12 mJ, at a much higher repetition rate, 500 Hz. This was accomplished by excluding additional amplification stages after the Regen, which limited the repetition rate of HERCULES due to the build-up of heat in the laser crystals.

Pulses were generated in the oscillator and selected by the pulse picker, shown in Fig. 3.2, in the same manner as the HERCULES pulses, but with a 500 Hz repetition rate. The pulse was then sent through a "Dazzler" and stretched to 250 ps before being sent into the regenerative amplifier with a pulse energy of 1 nJ. In the Regen the pulse was amplified to 5 mJ in 6 passes before it was cleaned using a Pockels cell pulse cleaner to remove ASE on the nanosecond time scale. Then, the pulse was then sent through a final 3 pass amplification stage to achieve a final amplification

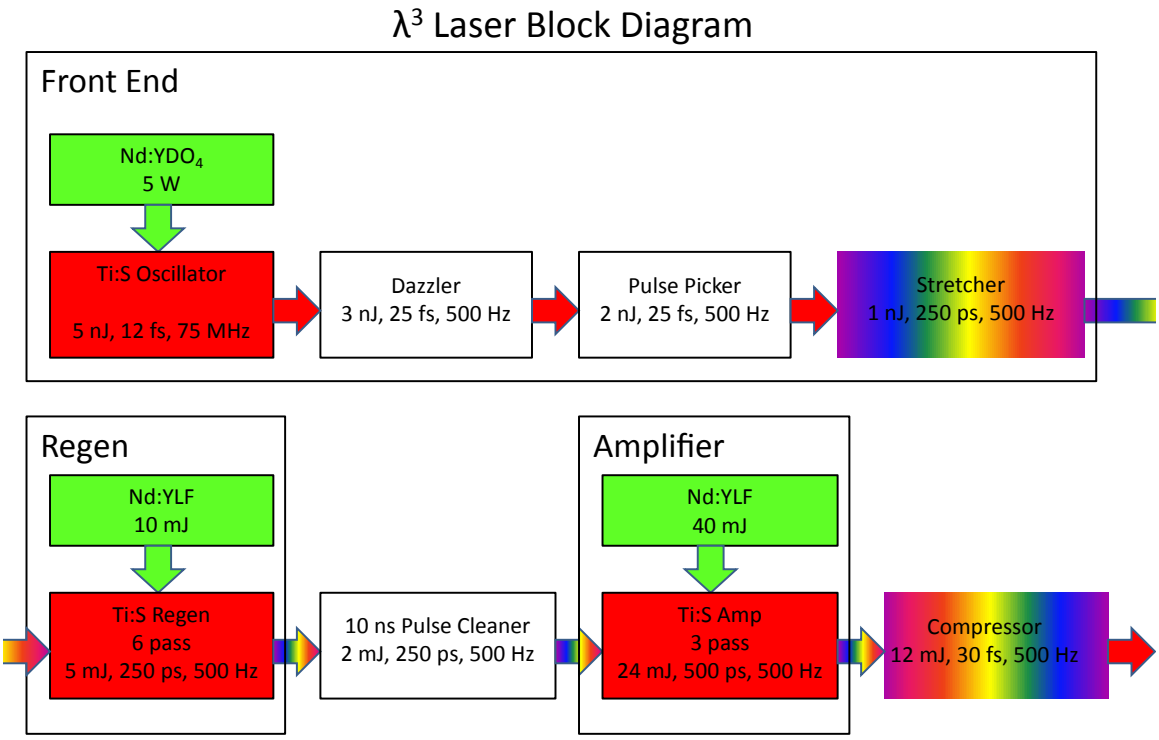

Figure 3.2: Block Diagram of the λ^3 laser system. Red blocks represent 800 nm laser amplification stages, while green blocks represent 532 nm pump lasers. Each stage is identified by its colloquial name. The post-compressor pulse was directed to the target chamber.

energy of 24 mJ. Recompression of the pulse produced a 12 mJ, 30 fs pulse. The 30 fs pulse duration was possible without the bandwidth gain narrowing that occurred in HERCULES.

3.2 Laser Diagnostics

Several laser diagnostics were employed in the solid target experimental area of HERCULES to monitor the beam quality throughout the course of an experimental run. A 1% leak-through mirror was used to allow a portion of the beam to be diverted to a diagnostic area located outside of the experimental chamber. The beam near-field profile was recorded with a CCD to measure the beam profile. The far-field was also measured to monitor the shot-to-shot and longer term drift of the beam pointing,

which could alter the focal quality if not corrected. The total beam energy, as well as the backscattered energy, was also measured using fast diodes. The backscatter measurement was primarily a precautionary diagnostic intended to prevent damage to the laser from amplification of light backscattered into the crystals of the amplification stages, but in some cases also served as a diagnostic of the reflectivity of the target.

Additional diagnostics were necessary to characterize the pulse contrast and intensity. These diagnostics were typically not employed during full power shots either due to their size and complexity, or inability to be run concurrently with experimental shots. However, measurements were performed at least once at full power to validate the low power measurements.

3.2.1 Diffraction Limited Focusing

Tight focusing of the laser was critical to achieving high laser intensity, as $I = \frac{E_L/\tau}{a}$ where E_L was the energy of the laser pulse, τ was the pulse duration, and a was the area of the focal spot. The diameter of the first null for a diffraction limited Airy disk was given by $d = 2 * 1.22 * \lambda * D/F$ where D/F was the focusing optic diameter over the focal length. A short focal length, $f/\# = 1$ or 3, Off-Axis Parabolic Mirror (OAP) was used to minimize the potential spot size and maximize the laser intensity. The use of an $f/1$ OAP required a 90^o off-axis angle to produce a focus sufficiently far away from the incoming beam to allow the positioning and manipulation of a target. The $f/1$ parabolas had peak-to-valley wavefront aberrations of approximately 0.5λ due to their large curvatures and the fabrication process, which utilized diamond turning and left grooves on the optical surface. High quality glass parabolas with high damage threshold dielectric coatings could have been utilized to reduce optical aberrations, however the close proximity of the parabola to the target interaction led to damage of the parabola surface, necessitating replacement of the parabola after several hundred shots. The high cost of dielectric parabolas prevented this from being

a realistic possibility.

In the presence of wavefront aberration, which primarily originated in the final focusing optic, but was also a result of other optics up-stream, a diffraction limited spot could not be achieved. In order to correct the aberration an adaptive optic Deformable Mirror (DM), manufactured by Xinetics, was employed in the solid target chamber. The DM was a thin dielectric mirror with 177 piezoelectric actuators which bent the mirror when a voltage was applied. The displacement of the surface of the mirror allowed the optical path length to be adjusted to correct for wavefront aberration. The DM was paired with a Shack-Hartmann HASO wavefront sensor manufactured by Imagine Optics, which was used to measure the wavefront aberration at the surface of the DM. While the DM was upstream of the final focusing OAP, the aberration of the OAP was also measured as it was a component of the imaging system. The HASO software calculated a response matrix by altering each actuator by $+/-$ 5 V and recording the change in the wavefront. A Zernike polynomial decomposition of the wavefront was then used to calculate a voltage correction for the DM which was iteratively applied over $5 - 10$ steps. It was typically only necessary to repeat a wavefront correction when an optical element in the experimental area or laser system was changed. The intensity of the focal spot was typically increased by at least an order of magnitude, as shown in Fig. 3.3 for an $f/3$ parabola. This allowed focal spots with very nearly diffraction limited profiles, as shown in Fig. 3.4, with a 1.18 μm FWHM from a DM corrected $f/1$ parabola.

A DM was also used in λ^3 to achieve nearly diffraction limited focal spots with an $f/1$ parabola. A genetic algorithm routine was used to optimize the λ^3 DM [90] by optimizing second harmonic light generation at the focal spot, which increased with higher laser intensity. The optimization routine was performed before every shot run.

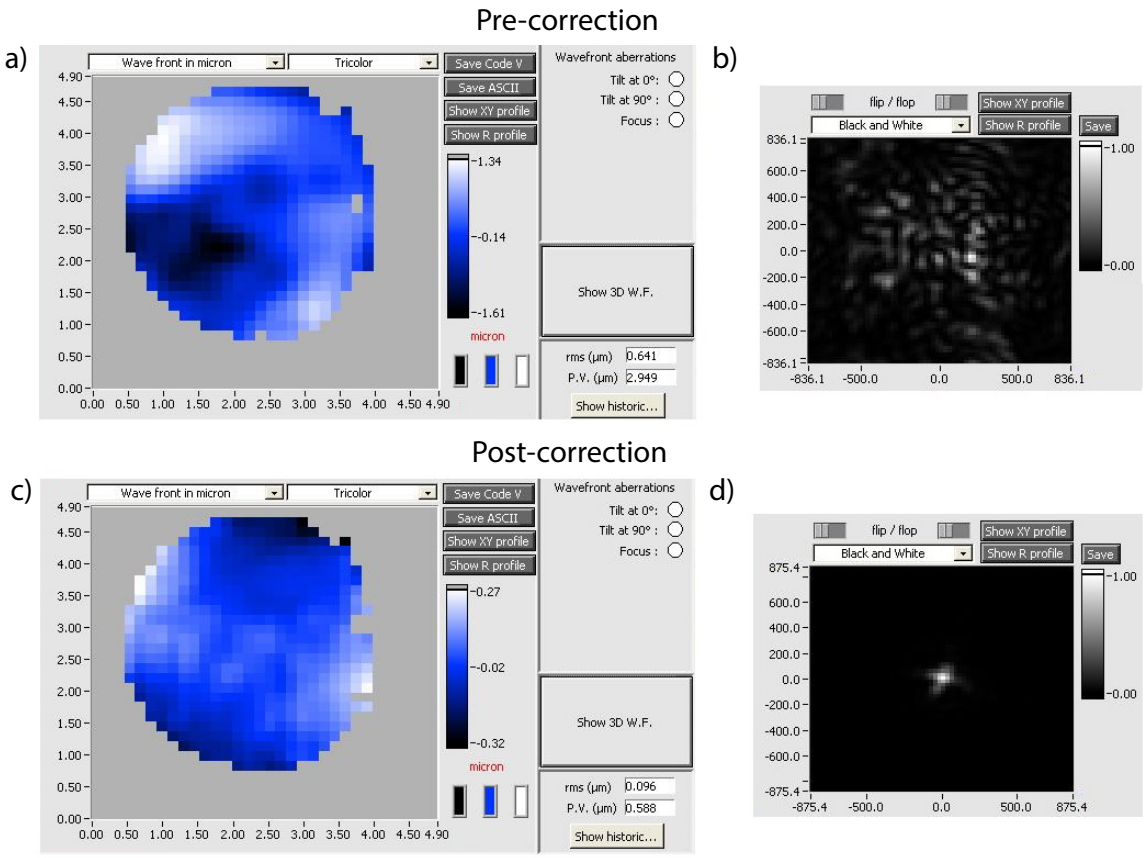

Figure 3.3: Screen captures of the HASO diagnostic showing the (a) pre-correction wavefront aberration, (b) pre-correction calculated focal spot, (c) post-correction wavefront aberration, and (d) post-correction focal spot. The wave front aberration is a spatially resolved measurement of the aberration in the incoming laser pulse measured at the DM surface. The color bar shows the magnitude of the wavefront aberration while the peak-to-valley and root-mean-squared values are shown on the bottom right. The focal spot image is a calculated optimum distribution of the light at focus given the wavefront measured at the surface of the DM.

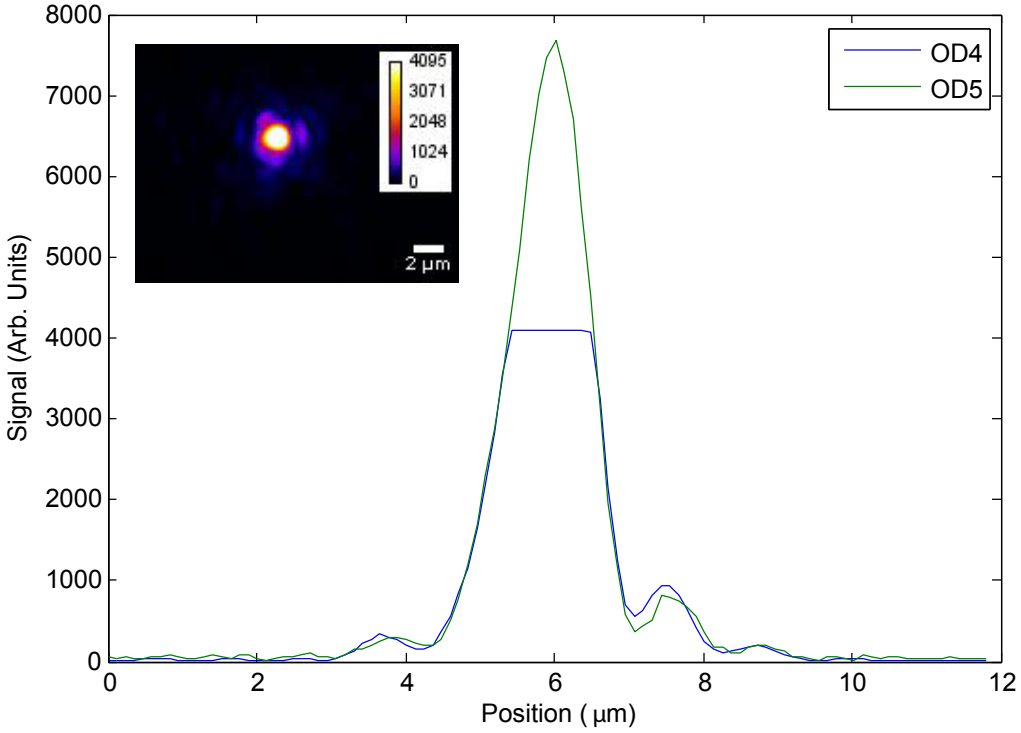

Figure 3.4: Focal spot from an F/1 parabola after DM correction with a 1.18 μm FWHM. The OD4 (blue) and OD5 (green) profiles show the spot with two filter configurations, increasing the dynamic range of the measurement. The OD5 plot has been scaled by an order of magnitude, compensating for the increase filter attenuation, to match the OD4 plot. (Inset) False color image of the focal spot with OD4 filtering showing the structure around the beam while the central portion is saturated.

3.2.2 Pulse Duration Measurements

Short pulse duration was also critically important to achieving high intensity. Measuring the pulse duration of a compressed Ti:Sapphire pulse was non-trivial due to the femtosecond pulse duration. Electronic measurements, i.e., a fast diode or streak camera, could not resolve the temporal evolution of the compressed pulse. Instead, a second order autocorrelator[91] was used to measure the compressed HERCULES pulse duration. A block diagram of the autocorrelator setup is shown in Fig. 3.5. The second order autocorrelator performed an autocorrelation of the pulse with itself by splitting the pulse and recombining it in a χ^2 crystal, which generated a second-harmonic as described in Section 2.1.2. The second harmonic light was then imaged to a CCD, as shown in Fig. 3.6. The delay stage was used to ensure temporal overlap of the recombined beams. The pulses were recombined with a slight angle between the two portions of the beam which introduced a temporal-spatial dependence on the beam overlap. The temporal-spatial calibration was performed by placing a glass slide of known thickness in one half of the incoming beam, providing a known temporal delay, and then measuring the spatial shift of the second harmonic light.

The pulse duration was measured as a function of the grating position, as shown in Fig. 3.7. The measured pulse duration had a minimum of 39 fs. This measurement includes a factor of $\sqrt{2}$ to account for the discrepancy between the autocorrelation intensity measurement and the desired Gaussian pulse FWHM measurement. Group delay dispersion for a parallel grating pair is always negative and compresses the pulse by compensating for the positive chirp introduced by normally dispersive material. The negative optimum grating position was a result of the need for correction of less total positive chirp in the laser system when it operated with XPW. The non-symmetric shape of the compression plot indicates high order dispersion, likely third, was present in the pulse.

Ideally, the Ti:Sapphire laser had enough bandwidth to achieve a compressed

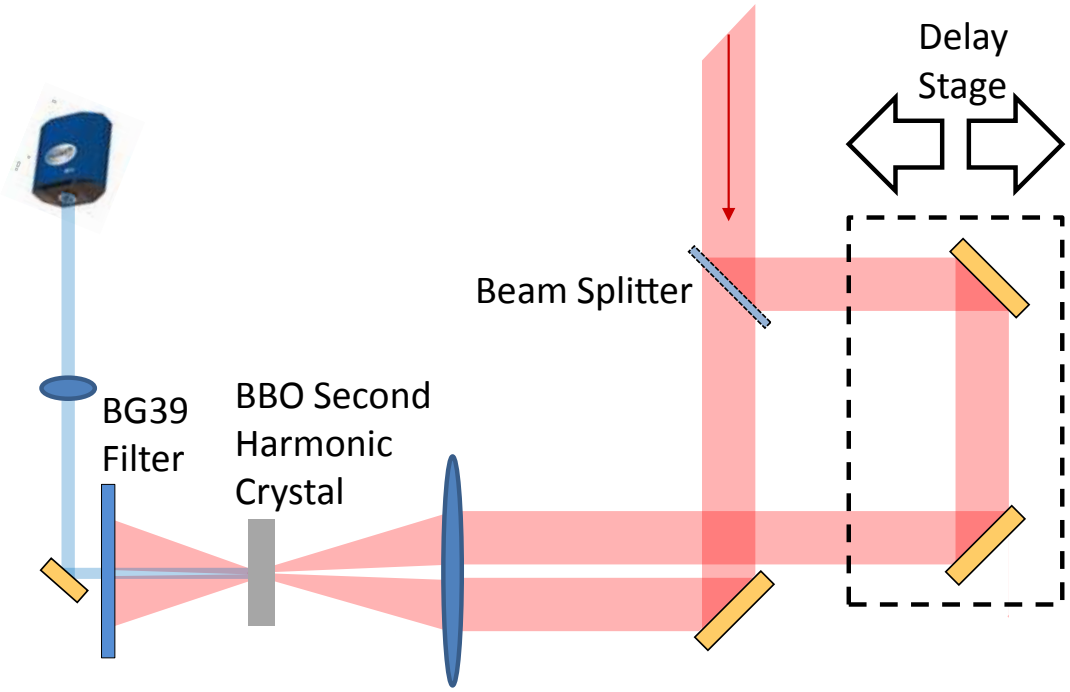

Figure 3.5: Schematic for a single shot second order autocorrelator. The beam was split and then recombined and focused into a BBO crystal. The second harmonic light was imaged to a CCD while the first harmonic was removed with a BG-39 filter.

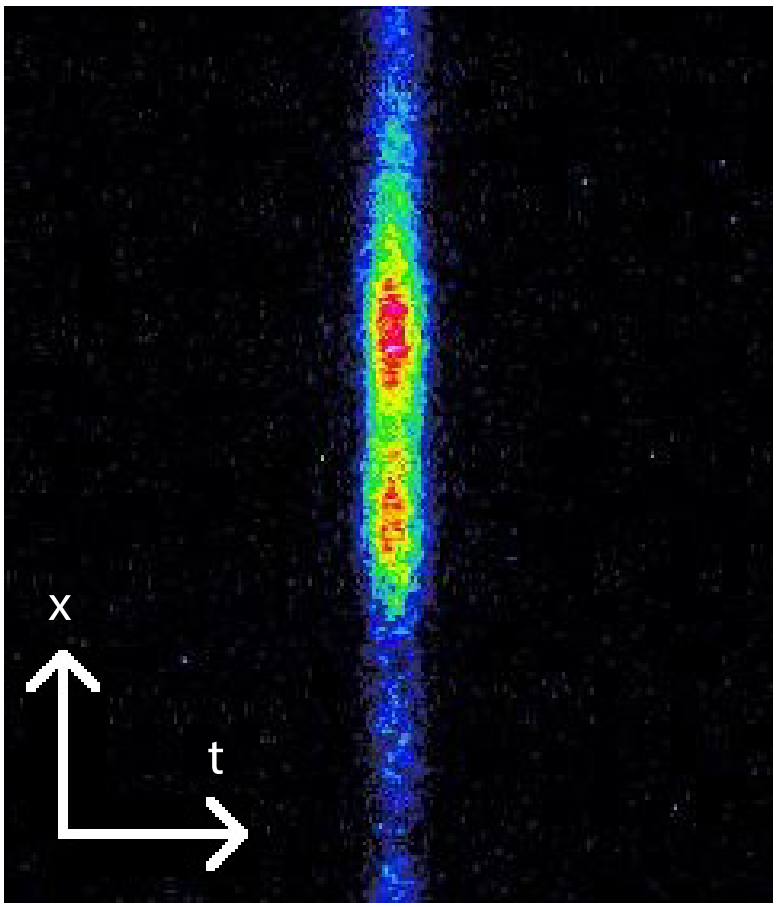

Figure 3.6: False color image of the autocorrelation light produced in the second harmonic crystal. A rotation of 2^o was performed to measure the pulse duration to account for the tilt of the pulse, which was a result of the imaging system.

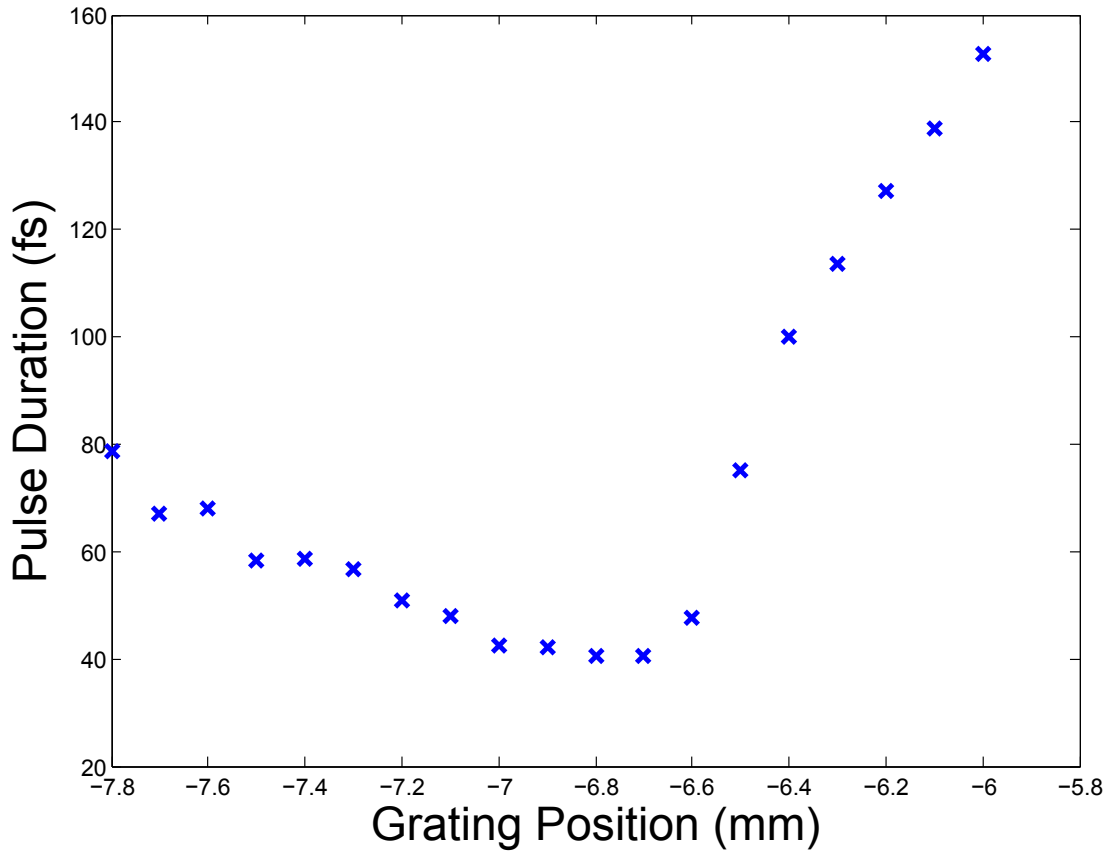

Figure 3.7: Pulse duration measurement of the HERCULES compressed pulse from second order autocorrelation showing a minimum pulse duration of 39 fs. The measurement was performed with XPW under vacuum. The grating position was relative to the approximate best compression position for the non-XPW pulse. Negative grating positions correspond to less negative chirp when compared to the reference position of zero.

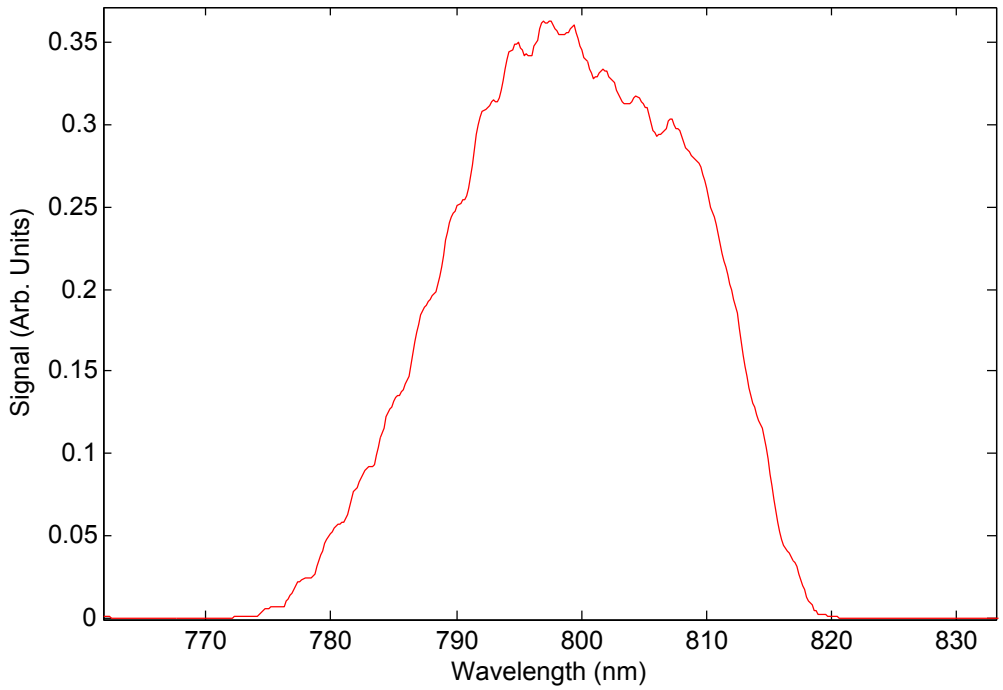

Figure 3.8: Pre-compressor optical spectrum of the HERCULES pulse showing a FWHM of 25.5 nm. The spectrum was recorded for every shot by collecting leak-through light from a 7 inch high reflectivity dielectric mirror located in the pre-compressor periscope. The light was focused into an optical fiber, through a diffuser, and delivered to a CCD Spectrometer.

pulse duration of 30 fs. The bandwidth of full energy shots was measured with a CCS175 Thorlabs Compact CCD Spectrometer by taking a leak-through from one of the precompressor mirrors. The FWHM bandwidth was typically measured to be around 25 nm, as shown in Fig. 3.8, however variations of up to 50% were observed on some shots. The 39 fs pulse duration measured by the autocorrelator was close to the bandwidth limited pulse duration of 37 fs from $\tau\Delta\omega \geq 2\pi c_B$ where $c_B = 0.441$ for a Gaussian pulse shape. The difference was attributed to higher order dispersion, as previously mentioned.

3.3 Laser Contrast

For solid target interactions the presence of ASE or pre-pulse dramatically altered the scale length of the plasma and, correspondingly, the laser interaction. As discussed in Section 2.2.3, the scale length of the plasma could shift the laser interaction between different absorption mechanisms. This change could result in differences in the fraction of laser energy absorbed by the target, the electron temperature, and even the energy spectrum of accelerated ions [92]. In extreme cases, especially for sub-micron thickness targets, the entire focal area of the target could expand below critical density before the arrival of the main pulse resulting in transmission of the pulse. It was necessary to characterize the laser ASE and prepulse in order to understand and control the target scale length.

The amount of light that arrived before the main pulse was characterized by the laser contrast, quantified as the ratio of the energy or intensity of the light arriving before the main pulse, to the energy or intensity of the main pulse itself. As even a perfect theoretical Gaussian pulse had a ramp from zero up to the peak, the contrast changed as a function of time and lower contrast was expected closer to the peak. In actual lasers, the ramp tends to have a flat pedestal that starts nanoseconds before the main pulse which is the result of ASE and pre-pulses which occur picoseconds before the main pulse, as seen in the black trace in Fig. 3.9. As a result of these two different physical processes, laser contrast was often quantified as nanosecond or picosecond contrast to differentiate the source of the light. As discussed in Section 3.1.1, HERCULES had several Pockels cells which optoelectrically filtered ASE nanoseconds before the main pulse. Additionally, XPW provided a three order of magnitude improvement in nanosecond laser contrast, as shown in the red trace in Fig. 3.9 [89].

However, additional contrast improvement was needed to allow experiments to be performed with sub-micron foil targets, and to provide better control of the pre-

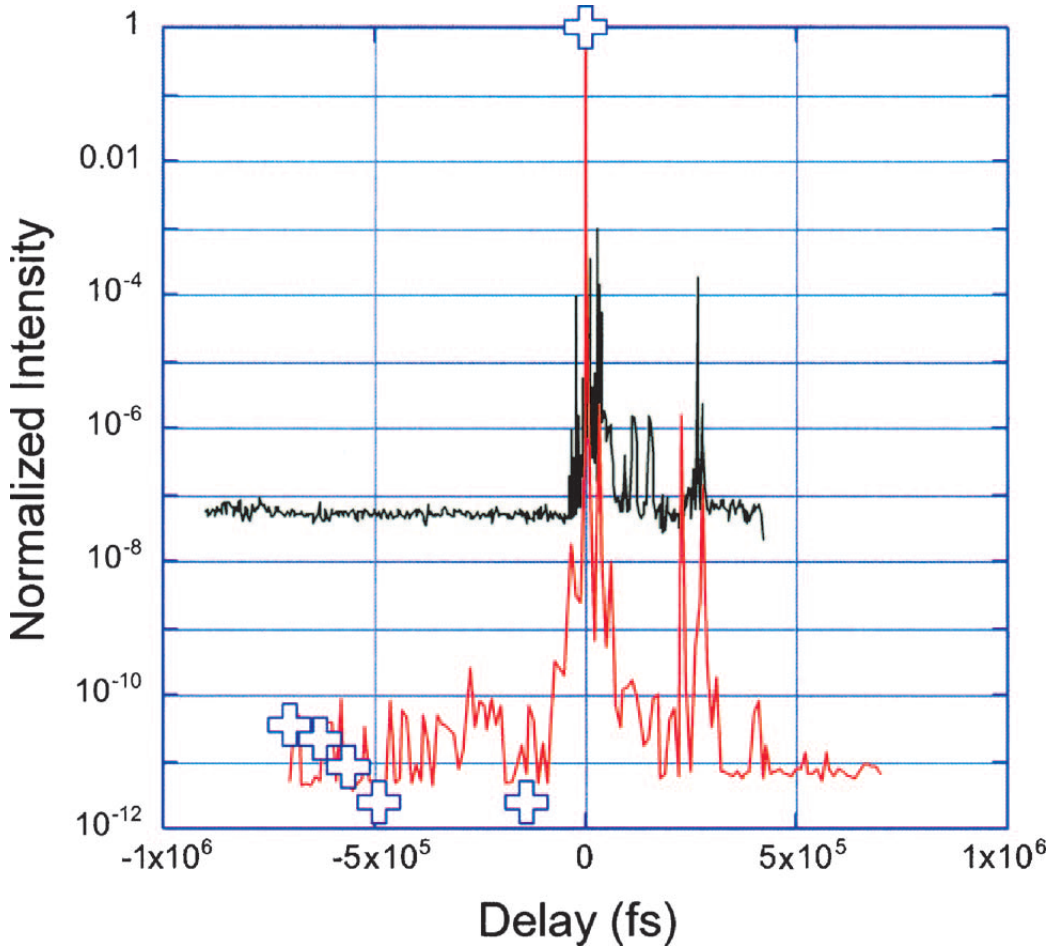

Figure 3.9: (Reproduced from V. Chvykov *et al.* [87]). Third-order autocorrelation with XPW (red) and without (black). The peaks of the red curve at the $10^{-10} - 10^{-11}$ level are due to single photoelectrons.

plasma scale length. This was accomplished by using two Plasma Mirrors (PMs)[93]. The PMs were anti-reflection coated optically flat glass slabs which reflected light after the pulse intensity reached the threshold for plasma formation. Prior to the formation of the plasma the anti-reflection coating reflected less than 1% of the incoming light into the correct optical path, while the rest was transmitted through the glass. Once the plasma was formed, s-polarized light was reflected with up to 70 % efficiency, measured experimentally. This was consistent with previous characterization of plasma mirrors [94], as seen in Fig. 3.10. While this plot shows that reflectivity increased with increasing fluence, a trade off existed between the reflectivity of the mirror and the contrast improvement of the mirror. Tighter focusing on the surface of the PMs resulted in earlier plasma formation, transmitting more of the early portion of the pulse. Additionally, formation of plasma on the surface of the PMs had to be restricted to several picoseconds prior to the main pulse arrival to ensure that plasma did not have enough time to hydrodynamically expanded, which would have introduced beam aberration by altering the optical path length.

Extensive details of the HERCULES PMs are available in the thesis of F. Dollar[95], including reflectivity characterization, measurements of the contrast improvements, and hydrodynamic modeling of the plasma formation. The contrast improvement result is reproduced[96] in Fig. 3.11. The nanosecond intensity contrast was improved about 4 orders of magnitude, as expected by the double pass $\leq 0.15\%$ anti-reflection coating, as shown in Fig. 3.11 (a). The dynamic range of the diagnostic limited the measurement of intensities below 10^{-8}. The laser energy flux ramp, which could have caused preplasma formation at the J/cm^2 level, is shown in Fig. 3.11 (b). The use of dual plasma mirrors (DPM) limited the preplasma formation to a few picoseconds before the main pulse.

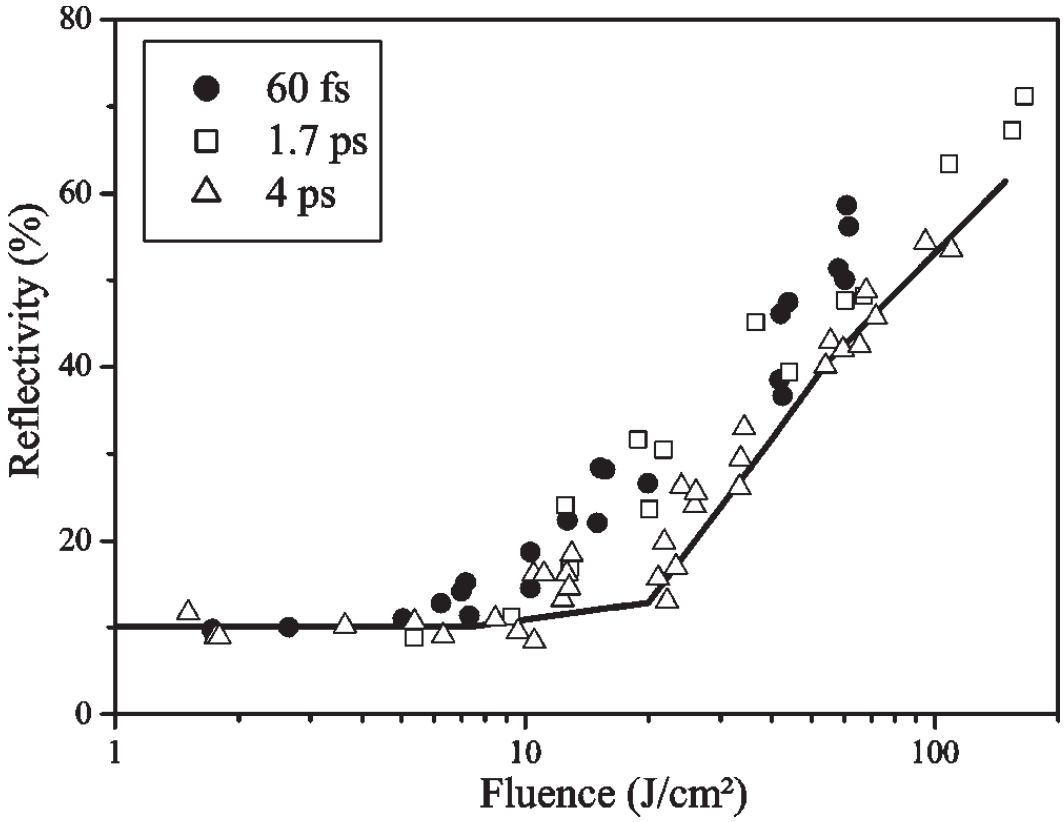

Figure 3.10: (Reproduced from Doumy, G. *et. al.* [91]). Reflectivity of bulk quartz as a function of incident fluence for three pulse durations. The fit shows good agreement with the developed theoretical model for the 4 ps pulse.

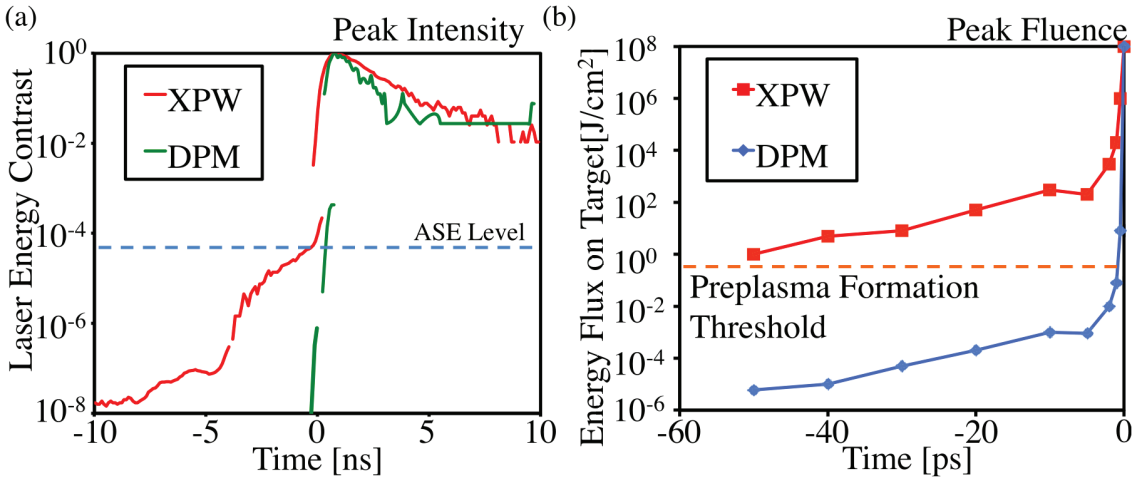

Figure 3.11: (Reproduced from Dollar, F. *et. al.* [93]). (a) The normalized laser energy as a function of time as measured by a fast diode. The XPW only (red) and post-DPM (green) traces were taken simultaneously. (b) 30 TW laser power flux measurements (red) as measured by a third order autocorrelator. Inferred DPM contrast is shown (blue) along with the preplasma formation threshold fluence. Lines are shown for visual aid only.

3.4 Radiation Diagnostics

One of the simplest, but most important experimental diagnostics was a combination of x-ray diodes and a NaI scintilator which were used to measure the strength of the laser-plasma interaction. These detectors measured bremsstrahlung photons produced by electrons accelerated from the interaction and were employed on both HERCULES and λ^3. These detectors were used to find the optimal focal position of the target by scanning the target through a variety of positions and observing the maximum signal. Additionally, they provided shot-to-shot confirmation of the stability of the interaction and laser.

The primary goal of each experiment was the production of energetic radiation, as discussed in Chapter I. The radiated quanta varied from neutrons to photons to light ions. In all cases measuring the energy spectrum and flux of the generated radiation was critical to the success of the experiment. To accomplish this task with, with both neutral and charged particles, as well as photons, several types of detectors were used.

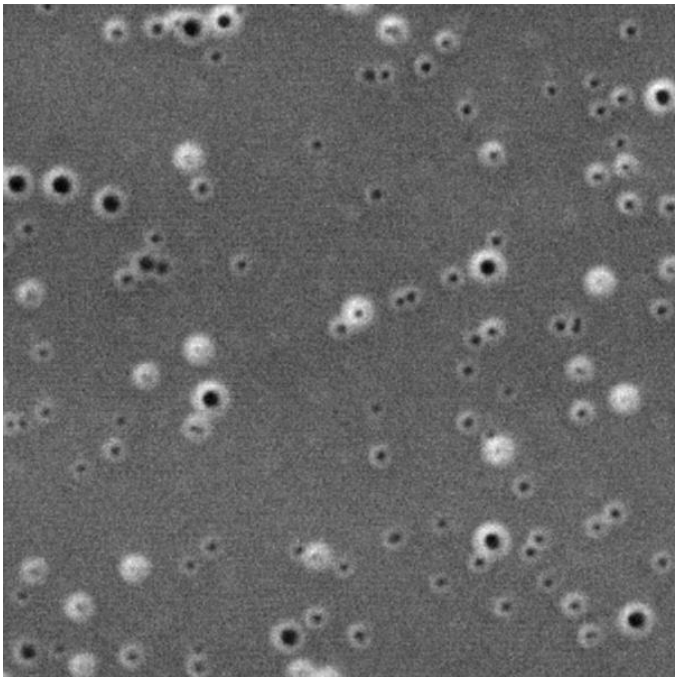

Figure 3.12: Microscope image of CR-39 exposed to a proton beam. Pits with two distinct sizes are visible.

3.4.1 CR-39

Allyl Diglycol Carbonate or Columbia Resin 39 (CR-39) was used as a nuclear track detector which provided absolute proton flux. The CR-39 was a thermoset plastic which was very sensitive to heavy-ion damage, amorphous, optically transparent, and insoluble [97]. Ions deposited their energy in their Bragg peak which broke chemical bonds and led to a localized chemical change in the plastic. The etchant, typically NaOH, degraded the weakened polymer instead of dissolving the material, leading to the etching of a circular track, or pit, in the surface of the CR-39 as shown in Fig 3.12.

Under well controlled temperature and chemical etching conditions the pit size could be used to determine ion energy, for a known ion. However, ion energy could also be determined through the use of filter stacks which set a low energy threshold for ions that could reach the CR-39. This was the preferred method for ion measurement as it was a more robust system. Filter stacks were typically encased in 12.5 μm of

Al foil which stopped protons with energies less than 1 MeV. Additional filtering was accomplished with layers of Mylar foil, stacked to provide energy bins up to 5 or more MeV. The stopping range of ions through combinations of Al and Mylar was calculated with SRIM [98].

Counting of the ion pits was performed by capturing images of regions of interest with an optical microscope and applying a particle counting algorithm using ImageJ (imagej.nih.gov/ij/). The image was converted to a 16-bit greyscale image and a threshold value was selected to convert to a binary image, as shown in Fig. 3.13. A built-in ImageJ function was used to identify continuous regions and filter them based on area and circularity which eliminated contributions from single hit noise and large pits that were the result of heavy ions. The 70 identified pits identified in Fig. 3.13 are shown in Fig. 3.14. One of the main advantages of using this technique over manual counting was the ability to apply the algorithm to different portions of a given image to verify the accuracy of the measurement through statistical checks such as pit density.

While CR-39 was an invaluable ion diagnostic, the need to etch and count pits prevented timely analysis of the data, while the single exposure nature of the diagnostic typically limited the number of shots that could be measured during a single experimental run on HERCULES. CR-39 was still employed in many experiments as it was a small, versatile diagnostic that could be placed anywhere inside the experimental chamber. Additionally, large pieces of CR-39 could be used to measure the divergence of ion beams.

3.4.2 Thomson Parabola Ion Spectrometer

A Thomson Parabola Ion Spectrometer (TP) [99] was the preferred ion diagnostic for real time measurements of ion energy and flux. The TP used parallel electric and magnetic fields, as pictured in Fig. 3.15, to disperse ions horizontally by energy,

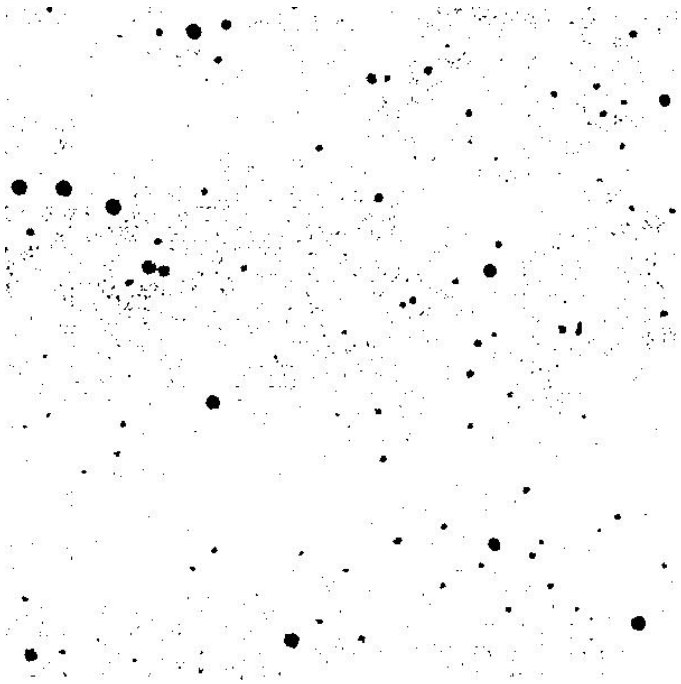

Figure 3.13: Image of the CR-39 after a binary conversion has been performed using a threshold value to highlight the dark centers of the pits. The two pit sizes are still distinguishable through size variation.

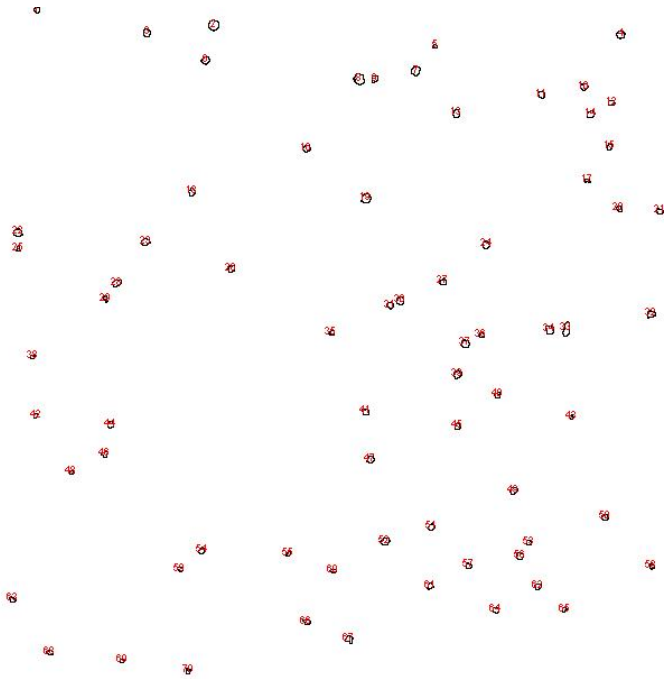

Figure 3.14: Result of applying the Image-J particle counting algorithm to the binary image which shows 70 identified pits. Only circles with areas between 10 and 70 pixels were counted. This rejected false positives from single pixel noise and the larger heavy ion pits.

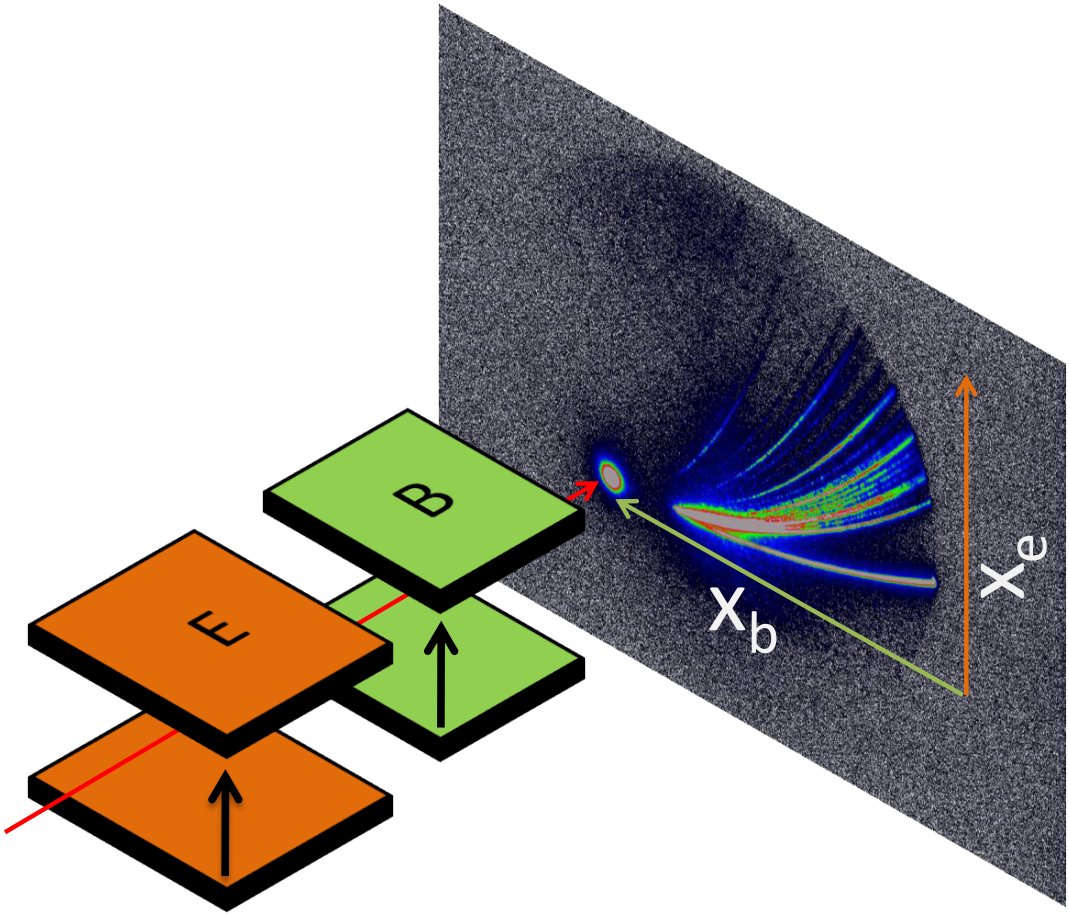

Figure 3.15: Diagram depicting the geometry of the Thomson Parabola. The electric field (orange) separates ions by q/m with lower ratios dispersed further from the axis. The magnetic field (green) disperses in the orthogonal axis with higher energy particles closer to the straight-through.

and separate different Charge to Mass Ratio (q/m) ratios vertically. The horizontal displacement at the detector plane was given by

$$x_e(v) = \frac{ZeEL_e}{Av^2m_p}(\frac{L_e}{2} + l_e) \tag{3.2}$$

where L_e was the length of the electric field, l_e was the distance from the end of the electric field to the detector, and $\frac{Z}{A}$ was q/m[100]. The magnetic deflection dispersion relation was similar and given by

$$x_b(v) = \frac{ZeBL_b}{Avm_p}(\frac{L_b}{2} + l_b) \tag{3.3}$$

where L_b was the length of the magnetic field, and l_b was the distance from the end of the magnetic field to the detector. These two equations were combined to give the parabola of a given ion species by solving for v which yielded

$$x_e = \frac{Am_pEL_e}{ZeB^2L_b^2}(\frac{L_e}{2} + l_e)(\frac{L_b}{2} + l_b)^{-2}x_b^2. \tag{3.4}$$

The parabolas defined by this equation, along with experimental data, are shown in Fig. 3.16 for each charge species of Al (magenta), C (yellow), and H (green). This diagnostic provided a full energy spectrum and flux measurement for each charge species as long as ions with the same q/m did not overlap. The detector was a micro-channel plate paired with a phosphor screen. The phosphor light was imaged to the face of a CCD. This detector allowed data to be acquired after every shot which provided shot-to-shot feedback and allowed optimization of the proton signal during an experimental run.

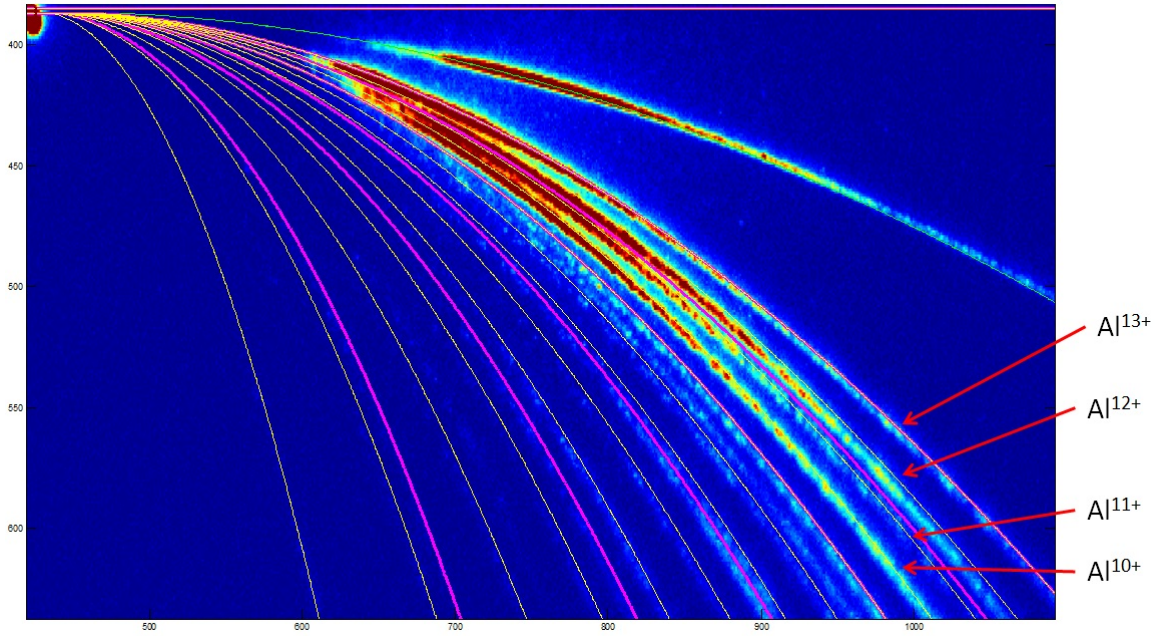

Figure 3.16: Thomson data from 1.8 μm Al overlaid with parabolas for different charge states. The three species are shown in different colors with the lowest charge ratios to the bottom left. The parabola for each charge species of H (green), Al (yellow), and C (magenta), is plotted according to Eqn. 3.4. The presence of Al^{13+} indicates a laser intensity of $>= 7 \times 10^{20}\ W/cm^2$.

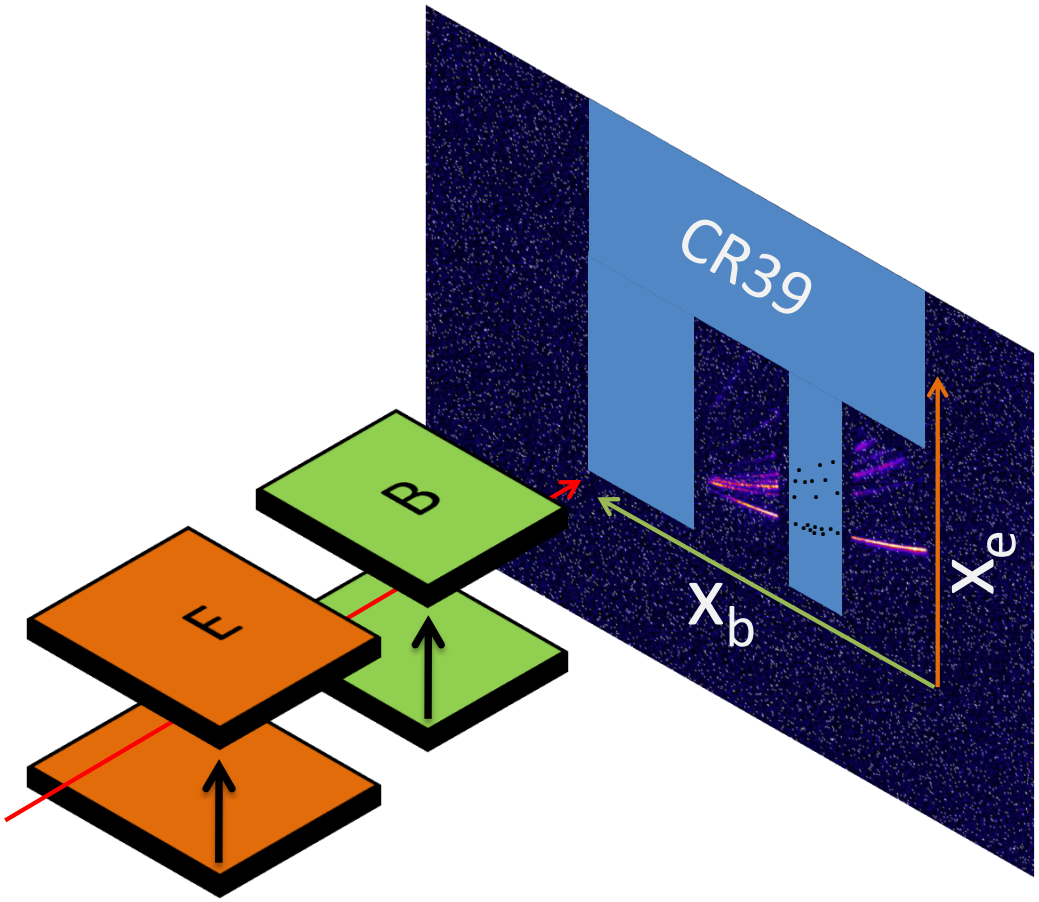

Figure 3.17: Schematic depicting the placement of CR-39 to measure the proton flux allowing a calibration of the TP. The "finger" cut-outs allow simultaneous single-shot measurement of the proton trace on the MCP and CR-39.

It was necessary to perform a calibration of the detector to obtain quantitative information from the CCD measurement. This was accomplished by measuring the ion flux of a single shot with both the TP diagnostic and CR-39 as depicted in Fig. 3.17. The ion parabola was partially intercepted by CR-39 which provided an absolute measurement of proton flux and provided a cross-calibration point with the CCD measurement, under the assumption the spectrum was smooth.

This measurement was repeated for two to three shots, for both protons and deuterons, and the collection of data points were used to determine a response curve of the TP diagnostic. A scaling factor between Microchannel Plate (MCP) counts and ions was determined using a best fit of the form[101]

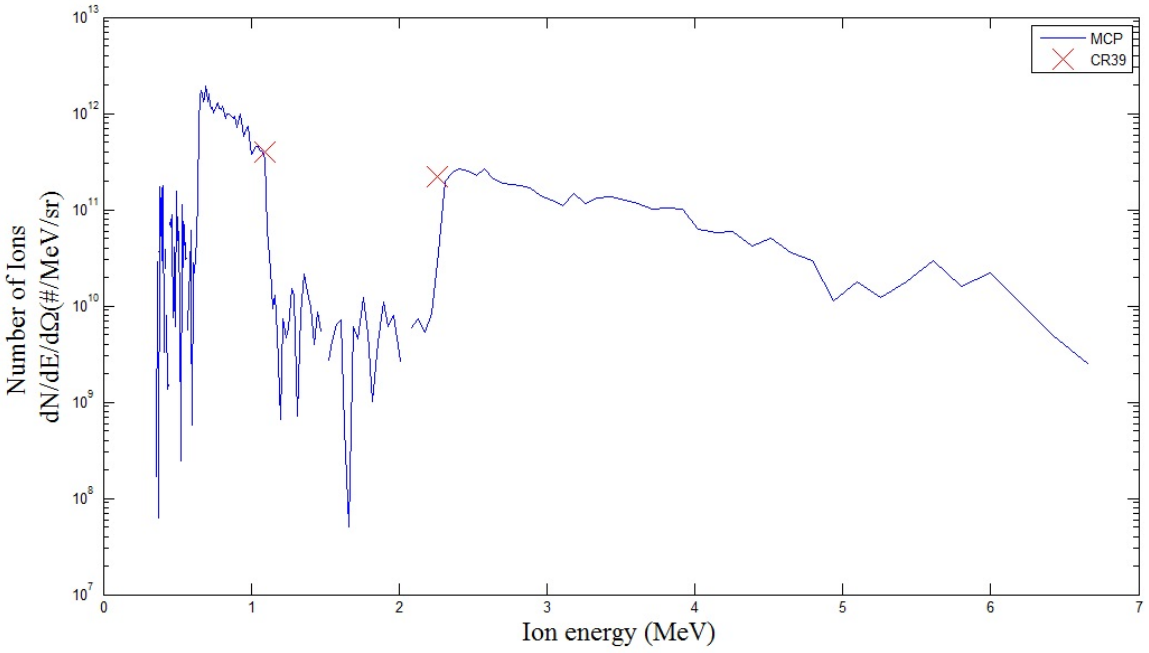

Figure 3.18: Calibrated TP spectrum showing MCP signal (line) and CR-39 (crosses) data points demonstrating consistency between the two methods. The target was 6 μm Al shot with the $F/1$ parabola and 150 TW laser power.

$$= A \times E^2 + B \tag{3.5}$$

where A was 5×10^{-4} for protons and 1×10^{-4} for deuterons, and B was 8.3×10^{-3} for protons and 1.3×10^{-2} for deuterons. A calibrated Thomson trace using this result is shown in Fig 3.18 along with two CR-39 data points, depicted as red crosses.

The TP was located behind the target and used to measure ion spectra from normal incidence targets. The MCP required a vacuum pressure of lower than 1×10^{-4} mTorr. This was accomplished by differentially pumping the TP chamber with its own turbo-pump. This requirement, along with the overall size of the diagnostic, constrained the TP to one of two ports on the solid target chamber. Therefore, measurements of charged particles in other directions had to be performed by CR-39.

3.4.3 Neutron Time-of-Flight

Measuring the energy of energetic neutrons required different types of diagnostics from those used for ions. While protons and light ions deposited their energy in a Bragg peak and could be stopped in a few microns of material, uncharged neutrons could pass through centimeters of material without depositing their energy. One potential method for detecting neutrons was initiating nuclear reactions and detecting the resulting charged particles. This could be done with $^3He(n,p)^3H$, $^{10}B(n,\alpha)^7Li$, or $^6Li(n,\alpha)^3H$. However, the cross section of these reactions peaked at thermal neutron energies making it inefficient for energetic neutron detection. Alternatively, elastic collisions between neutrons and light ions produced energetic ions which could be easily detected due to their charge. An elastic collision with an ion of atomic mass A at rest produced a maximum recoil energy of

$$E_{Rmax} = \frac{4A}{(1+A)^2} E_n \tag{3.6}$$

where E_n was the initial energy of the neutron. The energy transfer was maximized for hydrogen ($A = 1$) which minimized the number of collisions required to fully deposit the energy of the neutron. To take advantage of this, organic scintillators were used as the primary neutron detectors for experiments in HERCULES, as pictured in Fig. 3.19. Organic scintillators were available in large sizes and scintillators of up to 35.5 cm diameter were used to improve detection efficiency. When energy was deposited in the scintillator molecular energy levels were excited which decayed with a time constant τ_d and emitted light. The light was collected and directed to the photocathode of a photo-multiplier tube where photoelectrons were created and then multiplied. The collected electron signal provided a measurement of energy deposited in the scintillator. While this potentially could have been used to measure

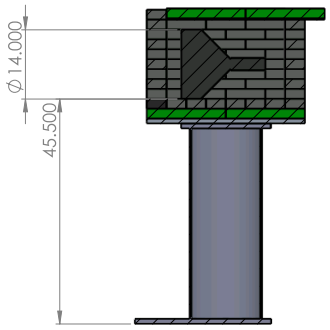

SECTION B-B

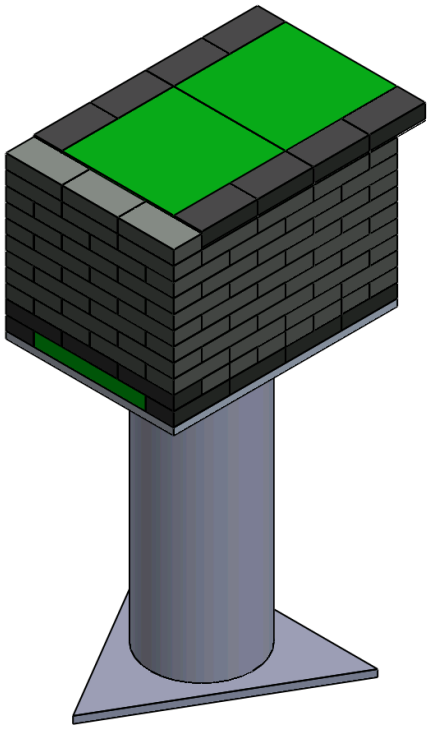

ITEM NO.	PART NUMBER	DESCRIPTION	QTY.
1	pedestal		1
2	metal_plate		1
3	borated_plastic		4
4	carbon_brick		19
5	14_inch_scintilator		1
6	lead_brick		120
7	metal_plate_thin		1

Figure 3.19: Schematic of the 35.5 cm nToF detector showing the Pb blocks used to shield the detector from photons. The detector was positioned on top of a pedestal to keep it in the interaction plane.

the energy of a single neutron, experiments in HERCULES produced neutrons with high instantaneous flux such that multiple neutrons arrived at the detector before any measurements could be performed.

Alternatively, the production of many neutrons in a short temporal burst, <1 ns, allowed measurement of neutron energy by determining the neutron speed in a Neutron Time of Flight (nToF) detector. The speed was measured by determining the time required for the particle to arrive at the detector, given the known time of creation, and distance. The energy was then given by

$$E_k = (\gamma - 1)m_0c^2 \tag{3.7}$$

where $\gamma = 1/\sqrt{(1 - v_n^2/c^2)}$. The energy range for neutrons measured in the reported experiments (a few MeV) was between the fully classical regime and the relativistic regime. Eqn. 3.7 recovers the classical kinetic energy equation, Eqn. 3.8, under the condition $v << c$ such that the binomial expansion can be used to expand γ, but the relativistic version was used for accuracy in data analysis.

$$E_k = ((1 + \frac{v_n^2}{2c^2}) - 1)m_0c^2 = \frac{m_0v_n^2}{2} \tag{3.8}$$

The neutron velocity, v_n, was found by using the known distance to the detector, D, which was $5 - 10$ m in the reported experiments, and the time delay between the gamma arrival and the neutron arrival, T_δ, such that

$$v_n = \frac{D}{D/c + T_\delta} \tag{3.9}$$

which accounts for the travel time of the gammas to establish the total travel time of the neutrons. This is pictured in Fig. 3.20 with experimental data. A region without any signal between the gamma burst and neutron peak was necessary to differentiate the signals. This was possible due to the short decay constant of the EJ-200 organic scintilator, $\tau_d = 2.1ns$.

Typically, several neutrons contributed to the neutron peak. A calibration was performed to determine pulse area of a single neutron in order to extract quantitative information about the neutron spectrum. The neutron detectors were calibrated at the Neutron Science Laboratory at the University of Michigan. A D-D generator (Thermo Scientific MP320-DD) provided a source of high duty cycle pulsed 2.45 MeV neutrons. The calibration used the same Pb shielding configuration as the experiments to replicate energy loss in the Pb bricks. The neutron generator produced

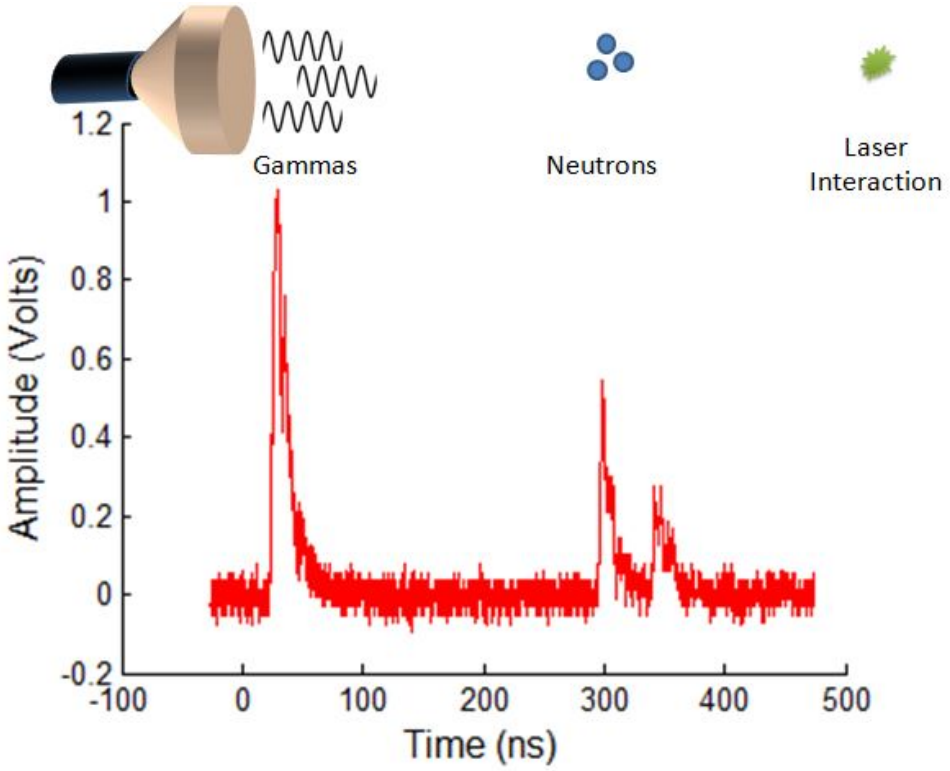

Figure 3.20: Sample oscilloscope trace from the plastic scintillator for a laser interaction creating photons and neutrons together. The gammas travel from the laser interaction at the speed of light and arrive at the detector first. The neutrons travel slower and arrive later yielding a measurement of their energy through the measured speed. A region of no signal between the gamma spike and the neutron arrival, as pictured in this trace, is very important for a quantitative measurement of the neutron flux.

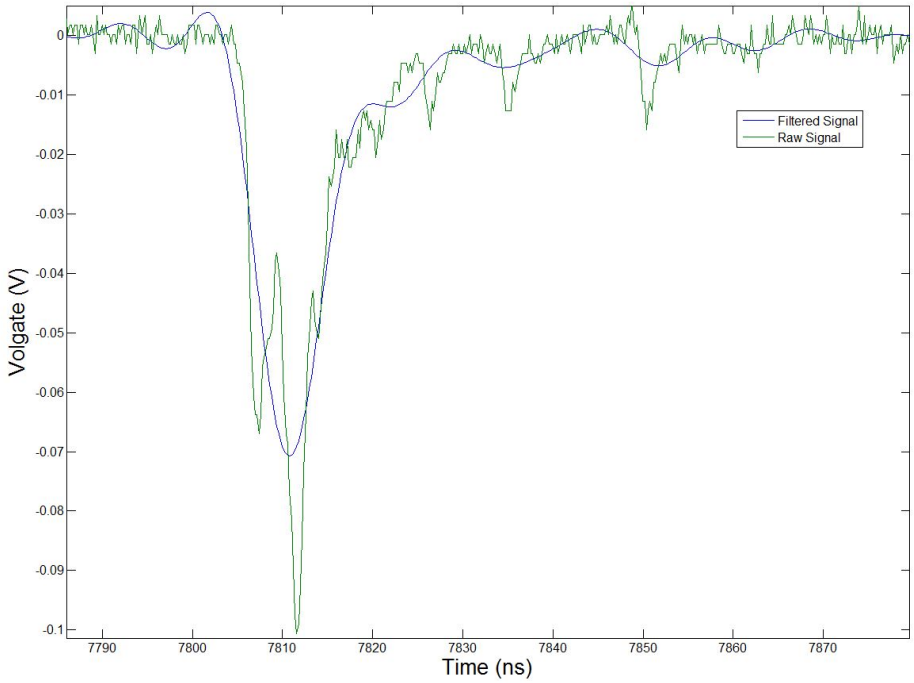

Figure 3.21: Sample oscilloscope trace from the plastic scintillator for a single D-D neutron hit.

2×10^6 neutrons per second with a 20 kHz shot rate. The large detector was placed 26 cm from the neutron source with 10 cm of Pb shielding placed 1 cm from the scintillator. The detector efficiency was measured at 20 percent behind 10 cm of Pb. This was consistent with previous measurements of detector efficiencies of 60 percent and 30 percent behind 1 cm and 6 cm of Pb, respectively. Single neutrons were measured using the nToF detectors and the signal was recorded on an oscilloscope as shown in Fig. 3.21.

The neutron events were interspersed between cosmic ray events which varied in pulse amplitude due to the random nature of the cosmic radiation. The neutrons were signaled out by identifying peaks with consistent areas and pulse heights, as shown in Fig. 3.22. A threshold voltage of 0.02 V was chosen to include the largest number of peaks without contaminating the data with noise, which was evident from the large increase in counts below thresholds of 0.02 V. This calibration was used for

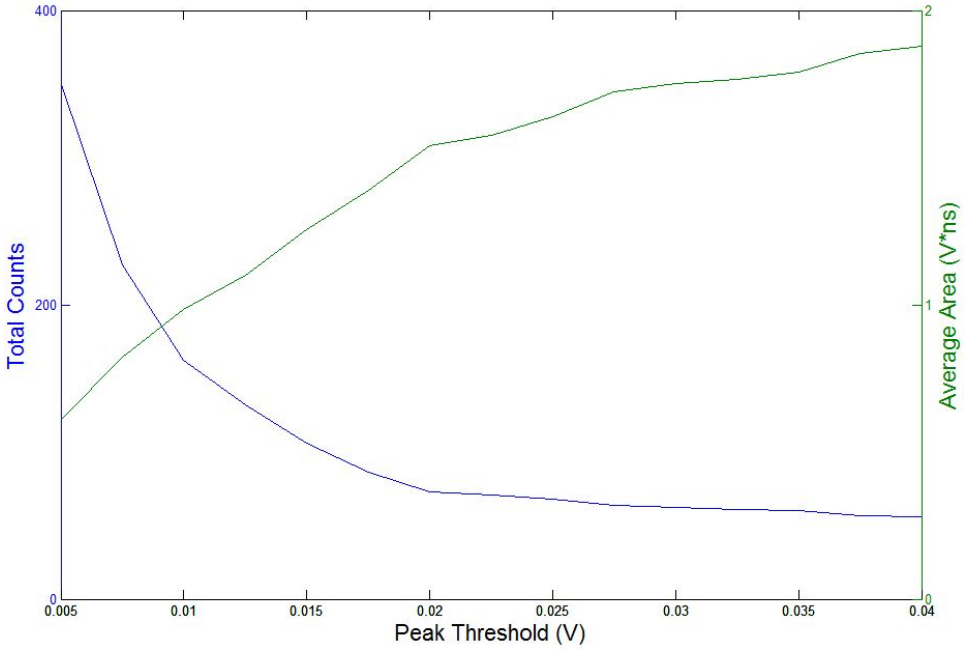

Figure 3.22: Plot showing the number of counts as a function of the peak voltage threshold. The average peak area is also shown as a function of the threshold voltage. The optimum threshold voltage was found to be 0.02 V. At this threshold the average area of a detected neutron peak was 1.5 V×ns.

all data analysis.

3.4.4 High Purity Germanium Detector

The detection of 100 keV photons, colloquially referred to as gamma-rays, could have been accomplished by scintillators or solid state detectors. High Purity Germanium (HPGe) detectors were used as they combined a small bandgap (0.7 eV) with the relatively high-Z material Germanium (32) to achieve high resolution and collection efficiency. Gamma rays interacted with the Ge in three ways. At low energies (100's of keV or less) the dominant interaction mechanism was photoelectric absorption. During such an interaction an atomic electron was ionized when it overcame the atomic Coulomb potential by absorbing the incident photon energy. The kinetic energy of the freed electron could be calculated from energy conservation considerations as

$$E_\beta = \hbar\omega - E_p \tag{3.10}$$

where E_p was the ionization potential of the electron. For relevant photon energies photoelectric absorption occurred primarily with K-shell electrons, which had the highest ionization potential. The probability of photoelectric absorption scales with Z^{4-5} and with photon energy as $E_\gamma^{-3.5}$.

At higher energies (up to MeV's) the predominant interaction mechanism was Compton scattering. Compton scattering involved the scattering of a high energy photon from an electron which resulted in the transfer of energy and momentum to the electron. Conservation of momentum yielded a governing equation for the scattered photon energy [9]

$$h\nu' = \frac{h\nu}{1 + \frac{h\nu}{m_0 c^2}(1 - cos\theta)} \tag{3.11}$$

where θ was the angle the photon is scattered from its original direction. The scattered photon energy ranged from the original photon energy (at $\theta = 0$) to half of the rest mass of an electron (at $\theta = \pi$). The resulting scattered electron energy was between zero and $E_\gamma - m_o c^2/2$. The fact that this energy range did not reach the original photon energy meant it was possible for the photon to escape the detector before depositing its full energy, resulting in a Compton gap below the photopeak.

The final gamma ray absorption mechanism was pair production. Gammas with energies higher than $2m_0c^2$ could produce a β^-/β^+ pair when they interacted with the Ge atomic nucleus. The produced positron annihilated with an electron producing two 511 keV photons which could subsequently interact with the detector material, through Compton scattering and photoelectric absorption, or escape the detector

material. Pair production scaled strongly with material Z and photon energy. As a result, the efficiency of capturing the full photon energy in all three absorption mechanisms was improved with the use of HPGe.

The theoretical limit of the energy resolution of HPGe detector was determined primarily by statistical considerations in the fluctuation of charge carriers. Since the average energy required to form an electron-hole pair in Ge was $\epsilon = 2.96$ eV, which was the lowest value of common detector materials, it had the highest possible number of signal carriers, and therefore the best theoretical energy resolution, as given by

$$FWHM_{lim} = 2.35\sqrt{FE\epsilon} \tag{3.12}$$

where $F = 0.1$ was the Fano factor, E was the photon energy[9].

Energy calibration of the HPGe detector was accomplished by using a least-square fitting of a polynomial of the form

$$E(c) = \sum_{n=0}^{N} a_n C^n \tag{3.13}$$

where N was the order of the polynomial and C was the discrete channel in which the photon was recorded. The HPGe detector was exceptionally linear and was adequately described by a second order polynomial.

The liquid nitrogen cooled Ortec model number GM45P4 HPGe detector was calibrated with a 3220 V bias. One drawback of HPGe detector was that due to the small bandgap it was necessary to cryogenically cool the detector with liquid nitrogen to prevent thermal excitation of carriers which led to signal noise or detector damage. A DSpec pro multi-channel analyzer was used to provide the bias voltage and discretize the output signal of the detector into 16000 channels. The Maestro32 software package was used to control the instrument and record the experimental

Source	Activity (μC)	Peak (keV)	Relative Strength
^{133}Ba	0.565	276.4	0.073
^{133}Ba	0.565	302.8	0.19
^{133}Ba	0.565	356	0.62
^{137}Mn	0.767	661.6	0.85
^{60}Cd	0.152	1173.3	1
^{60}Ba	0.152	1332.5	1

Table 3.1: Table showing sources along with calibrated activities. All sources were calibrated November 16th, 2000, and the decay of their activity has been taken into account in the listed numbers.

data. The HPGe active detector volume was cylindrical with a 70 mm diameter.

Several calibrated radiation sources, listed in Table 3.1 were located 7.5 cm from the face of the detector at the detector height. In this geometry the detector occupied a 54 msr solid angle. A second calibration was done at a distance of 4.3 cm to verify the calibration. The measurements were taken for ≈ 3 hours each.

The detectors intrinsic photopeak efficiency, i.e. the efficiency of measuring the full energy of a photon that arrived at the detector active volume, was calculated by comparing the expected number of counts from the nuclear sources, to the recorded counts. The efficiency curve peaked at about 100 keV and fell off for lower and higher energies as a result of the varying efficiencies of three types of gamma ray interactions.

For the region of experimental interest, 200 keV to 1 MeV, it was sufficient to model the efficiency curve as a power function. The measured efficiency and the power function fit are shown in Fig. 3.23. It should be noted that this calibration was done with the detector inside of a lead shielding enclosure with >4 inches of lead in every direction. While this reduced the natural background it effectively increased the collection efficiency of the detector by introducing the potential for low energy photons to be scattered from the shielding into the detector. Additionally, it introduced K-shell peaks from lead with energies between 72.1 and 85.5 keV. These two effects contaminated a ^{133}Ba line at 81.0 keV which was measured to have an efficiency of 2.5 or 250% and was therefore not included in the efficiency calibration.

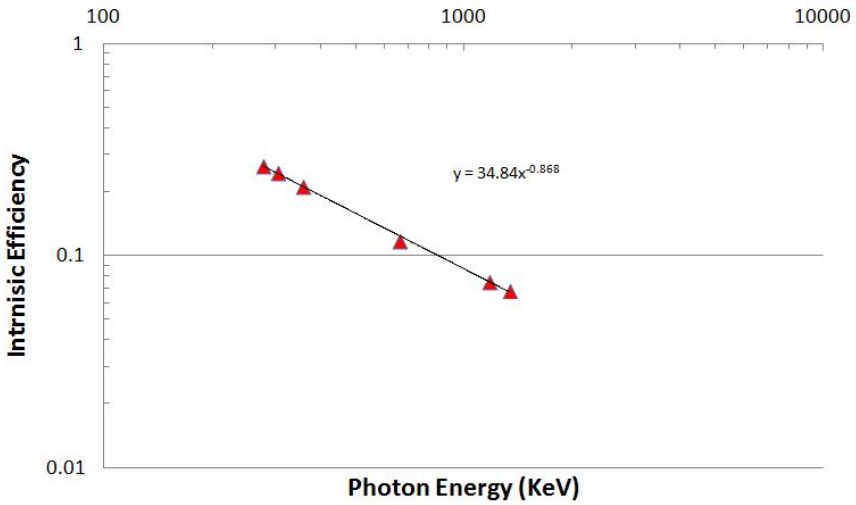

Figure 3.23: The HPGe detector's intrinsic photopeak efficiency was measured using 6 peaks that spanned the energy range from 274 keV to 1.33 MeV. The efficiency fits a power function over this range which is dominated by Compton scattering. Below 100 keV the efficiency drops as the dominant energy transfer mechanism becomes photoelectric absorption.

3.5 Computational Modeling

The small spatial scales, fast temporal evolution, and high density of solid target laser plasmas limited direct experimental access to the conditions of the system. Probing the plasma conditions of typical experiments required particles or photons with keV to MeV scale energies, which under certain conditions could be self-generated through the laser plasma interactions or generated with the use of a second laser. A few examples of experimental techniques that probe plasma conditions include proton[58] and electron[102] radiography, and optical polarization measurements [103]. In addition to experimental measurements, numerical simulations were an invaluable tool in understanding the complex transient behavior of laser produced plasmas and resulting physical processes. Simulations offered insight into individual particle trajectories and the fine spatial structure and evolution of electric and magnetic fields. Simulations could also be used to infer information about the interior of a plasma through modeling of the escaping radiation. For example, the modeling

of bremsstrahlung to infer the details of electron behavior inside a solid target will be discussed in Section 2.4.2. Monte Carlo and PIC codes were used extensively to model the experiments presented in this thesis.

3.5.1 Monte Carlo N Particle Transport Code

Monte Carlo simulations model a wide variety of stochastic processes through repeated random sampling. In particular, Monte Carlo methods were employed to model the behavior of particles in materials. Elastic and inelastic scattering, particle slowing, and nuclear reactions were a few of the processes of interest that could be modeled statistically. Several Monte Carlo codes were regularly employed in support of laser plasma experiments including SRIM [98], used to calculate the stopping range of protons in Mylar and Al for the CR-39 stacks described in Section 3.4.1, GEANT4 [104], and Monte Carlo N-Particle eXtended (MCNPX)[105].

MCNPX was originally developed to model nuclear reactions, including reactor criticality, but now also models particle interactions such as bremsstrahlung. MCNPX modeled three dimensional space composed of continuous volumes. Each volume had material properties allowing specification of material type, isotopic composition, and density. This allowed complex experimental geometries and detector configurations to be modeled. In Chapter VI, MCNPX was used to model the scattering of neutrons during their flight from the laser plasma interaction to the nToF detectors, including the effects of the vacuum chamber wall, detector shielding materials, room walls, air, and additional material in the flight path of the neutrons. In Chapter IV, the bremsstrahlung modeling of capabilities of MCNPX were used to simulate the generation of bremsstrahlung photons by electrons accelerated into a bulk target. MCNPX calculated the behavior of one particle at a time. For electrons the time step was chosen such that multiple collisions occurred during every step, which ensured the validity of multiple-scattering models, but the total energy loss per per

was still small. During each step the cross-sections for all modeled processes were evaluated through random statistical sampling. The results from each step for each particle were compiled and used to evaluate the behavior of the system. This statistical method intrinsically required a large number of particles to ensure the accuracy of the result, and as such several accuracy checks were integrated into the output of the code. The cross-sections were a compilation of experimentally measured data tables and analytic models. The primary analytic model was based on the Bethe-Heitler Born-approximation[106]. The model was well established and detailed reference papers were available that summarized the model[21] and discussed its implementation [107] in MCNPX.

A similar approach was used to model the generation of neutrons in a LiF slab in the results reported in Chapter VI. A Monte Carlo code developed by Davis *et al* [65] was used, which utilized double-differential cross sections (energy and angle) [108] to calculate angularly resolved neutron spectra from an input deuteron spectrum. The input deuteron spectrum was calculated using a PIC code.

3.5.2 OSIRIS

Simulation of a laser produced plasma could be accomplished through several computational approaches depending on the time scales and physics of interest. For example, Magnetohydrodynamics (MHD) methods were typically used to model shock dynamics over nanosecond time scales, Vlasov-Fokker-Planck (VFP) methods were appropriate for modeling collective plasma processes in high density plasmas where collisional processes and material resistivity influence plasma behavior, and PIC methods were possible for small systems and short time scales. Both MHD and VFP formulations treated plasmas as fluids, which allowed macroscopic treatment of collisional effects such as resistivity, but were based on assumptions which limit their validity (i.e. MHD codes often did not treat or resolve electron dynamics). Alter-

natively, PIC codes modeled plasmas as kinetically evolving individual particles, or macro-particles which represent multiple particles, which did not require the same assumptions as fluid methods. In PIC simulations fields were calculated on an artificial grid by weighting each macro particle to the spatial grid points and calculating the fields from Maxwell's equations. The particle motion was then calculated using the Lorentz equation. The spatial resolution, number of macro particles, and time step had to satisfy both the Nyquist theorem, the sampling rate must be $>2f_{max}$, and the Courant condition, $\frac{1}{d_t^2} \leq \frac{1}{d_x^2} + \frac{1}{d_y^2}$ to achieve numerical stability and capture the correct physics. The high density of solid targets, 100's of n_{crit}, and the corresponding high plasma frequency, required spatial resolution on the order of nanometers. For a 10 μm $\times$ 10 μm simulation space this requires around 10 thousand spatial grid points in each spatial direction. For typical PIC codes which require 10's of macroparticles per grid point, also known as Particles-Per-Cell (PPC), macroparticle numbers in the billions were not uncommon. This sets requirements on computer memory, was it required 1 GB of memory to store 6 dimensional information for tens of millions of particles, and processing speed for the immense number of calculations, which scaled as $\approx 10N_{particles}$. Fortunately, PIC methods were well suited for distributed computing methods, where the simulation space and particles were segmented and simulated separately on individual nodes of a super computer. After each time step the boundary information was shared between each node with minimal overhead, resulting in close to linear scaling of simulation speed with processor number.

The OSIRIS PIC code was the main simulation tool used to model the experiments discussed in the following chapters. OSIRIS was a fully relativistic, massively parallel plasma simulation code developed by the OSIRIS consortium[109]. The code could be run in one, two, or three spatial dimensions with three dimensional velocity space, but due to the limitations previously described, was typically only run with two spatial dimensions. Simulations were performed using the University of Michigan's super-

computing facilities at the Center for Advanced Computing, allowing simulations to be run on up to 192 nodes.

CHAPTER IV

Bremsstrahlung Generation

4.1 Introduction

Homeland security applications require photons with energies of 100's of keV to 10's of MeV, as discussed in Section 1.2. High intensity ultrafast lasers allow the direct acceleration of electrons to MeV energies in laser-solid target interactions [80] providing an MeV source of electrons and bremsstrahlung photons. In addition to homeland security applications [110], bremsstrahlung sources have been investigated for applications in medicine [111] and nuclear physics [45, 46, 112]. Very high resolution gamma ray measurements are needed for nuclear physics experiments, including very short half-life isotope and isomer identification. A detailed understanding of the qualities of the generated electrons and photons is critical to evaluate their potential use for applications.

Previous efforts to characterize laser driven bremsstrahlung sources over 100 keV have generally relied on experimental measurements using low resolution absorption filters [113] and nuclear activation stacks [114], as well as simulations [115]. In a few cases, high-resolution measurements have been performed using crystal spectrometers at energies of 100's of keV [116], but in a relatively narrow spectral range. As an alternative, this chapter presents the first high-resolution bremsstrahlung measurements using an HPGe detector, which was capable of measuring photons from 30 keV

to 3 MeV with a resolution of $E/\Delta E$>200, with a 500 Hz repetition rate, high power laser system [117]. The bremsstrahlung spectra was acquired by operating the HPGe detector in a single-hit regime and integrating up to 1.9 million shots. This novel application of an HPGe detector had not been practical previously due to the low repetition rates of typical high intensity lasers.

The measurements were performed at multiple positions around the target to determine the directionality of the generated radiation. Previous work to characterize the hot electrons generated by laser-solid interactions on λ^3 found that a beam of energetic electrons escaped from the front, or laser side, of a bulk target near the direction of the specular light reflection [83]. This beam was also observed during the present work and was observed to have a 7 degree FWHM. It was postulated in reference [83] that a significant fraction of the electrons were also accelerated into the target, however the target thickness made a direct measurement of the forward accelerated electrons impossible. In this work, the accumulated high resolution photon spectra provided a measurement of the bremsstrahlung as well as insight into the behavior of the electrons, both inside and outside of the target, through modeling of the bremsstrahlung process.

This was possible because the spectral and angular emission characteristics of bremsstrahlung are tied to the electron kinematics. The angular component of the differential bremsstrahlung cross section for an electron in a solid can be modeled as a Gaussian [87]

$$\frac{d\sigma}{d\Omega} = \frac{1}{\pi(\bar{b}\theta_b)^2} exp(-\frac{\theta^2}{(\bar{b}\theta_b)^2}), \tag{4.1}$$

with a FWHM angle given by

$$\theta_b = \frac{m_e c^2}{E_e + m_e c^2} \tag{4.2}$$

where E_e is the electron energy, $\bar{b}$ is a fitting constant ≈ 1, and the angle θ is the angle between the electron and bremsstrahlung photon. The angularly integrated cross section can be described with [87]

$$\frac{d\sigma}{dE} = \frac{aZ^2}{E}(1 - bE/E_e) \tag{4.3}$$

where E is the energy, $a \approx 11$ mb, b is a fitting constant ≈ 0.83 based on the results of Seltzer and Berger [118], and E_e is still the electron energy. As a result, the most energetic electrons produce the highest energy bremsstrahlung photons with a well-defined directionality. This enables an indirect measurement of the electron energy distribution and direction through the correlation between the direction of the high energy electrons and high energy photons. For distributions of electrons the bremsstrahlung spectra is a summation of the bremsstrahlung spectra from electrons of each energy which has no compact analytical form. In this work, bremsstrahlung modeling of the full three-dimensional experiment was accomplished using the Monte Carlo code MCNPX, and will be discussed in the simulation section.

4.2 Experimental Setup

The experiment was performed using the λ^3 laser facility at CUOS. As discussed in Section 3.1.2, λ^3 is a 0.5 kHz Ti:sapphire system ($\lambda \simeq 800$ nm) producing laser pulses with $\tau = 30$ fs FWHM pulse duration and an amplified spontaneous emission-to-peak intensity contrast of 10^{-8}. The laser was focused to a 1.3 μm FWHM focal spot by

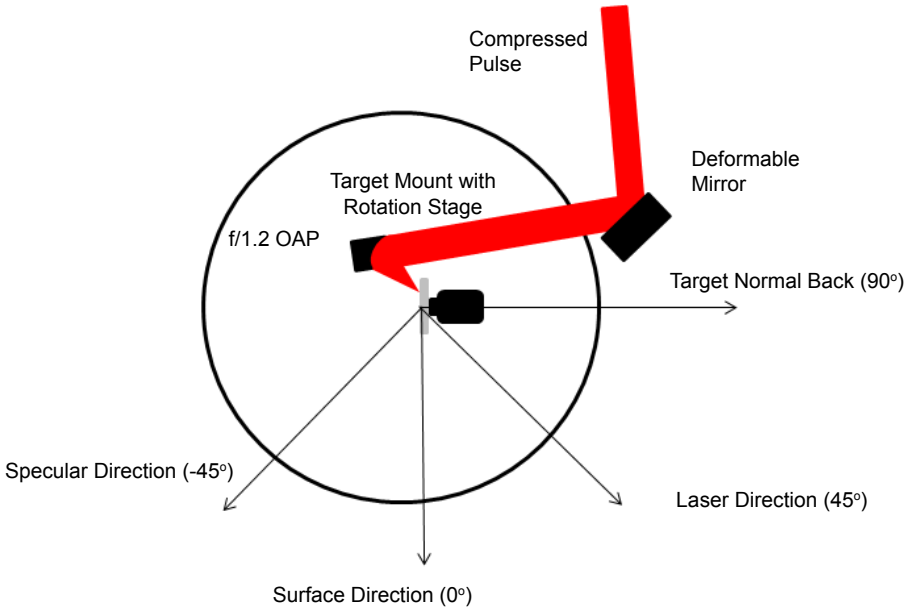

Figure 4.1: Experimental setup of the target chamber. The bremsstrahlung observation angles are shown.

an $f/1.2$ off-axis parabolic mirror in conjunction with a deformable mirror (Xinetics Inc.) optimized by a genetic algorithm [90]. Each laser pulse contained between 2 and 10 mJ producing focused intensities of 2.5×10^{18} W/cm^2 to 1.2×10^{19} W/cm^2. This corresponded to a peak normalized vector potential $a_0 = \frac{eE}{m_e c \omega_0}$ of 1.1 to 2.4. P-polarized light was incident at 45^0 after passing through a 2 μm thick nitrocellulose pellicle used to protect the paraboloid from the target ablation debris. The pellicle was necessary to prevent the ablated material from accumulating on the paraboloid as a result of the large number of shots. The high repetition rate required the target surface to be rapidly refreshed which was accomplished by rotating and translating the target so that each shot interacted with a fresh area in an inward spiral pattern. Each target was a 10 cm diameter bulk Eu_2O_3, SiO_2, or Mo disk with a thickness of 1.2 ± 0.2 cm. Special care was taken to align the target surface with a Mitutoyo $513 - 405T$ dial gauge to maintain the surface peak to valley deviation over a full rotation of ± 2 μm, significantly smaller than the Rayleigh range ($2z_r = 11\mu$m). Target focus was

optimized by maximizing the x-ray signal on a Si x-ray diode. The spot separation of 120 μm allowed $5(\pm 1.5) \times 10^5$ shots per target. The 7^o FWHM half angle specular electron beam was measured experimentally by imaging the electron distribution with Fujifilm BAS-MS image plate. The electron distribution was observed to be much lower in energy and more uniform at other angles in front of the target, and energetic electrons were not observable through the target due to the thickness.

The HPGe detector was an Ortec GMX55P4 − 83 PopTop detector described in Section 3.4.4. The detector was experimentally measured to have a resolution of 1.7 keV at 661.33 keV, typical for HPGe detectors, which results in a resolution $E/\Delta E$>200 over the entire range of the measurement. Most bremsstrahlung spectrum were accumulated over 90 or 120 thousand shots with a count rate of 75 to 125 counts/s, or equivalently, a detection event probability of 15% to 25% of the shot rate. The HPGe detector was located 7.7 m from the interaction and the detector element was shielded with >5 cm of lead, except for a variable aperture limiting the detector solid angle to 6×10^{-5} to 9×10^{-7} sr. The low detection probability and the large detector distance were required to prevent photon pile-up. Photon pile-up is the collection of multiple photons in the detection volume in a time period shorter than a μs, which records the sum of the photon energies as a single, more energetic, photon. The HPGe line of sight passed through the 3.5 mm stainless steel chamber wall which blocked photons with energies lower than 30 keV and allowed 66% to 85% of the photons in the energy range of interest to reach the detector, which was accounted for in the measured spectra. The removal of the low energy photons was critical to prevent pile-up from photons below the energy range of interest. At the experimental detection probability 8% to 14% of the detected photons were due to pile-up. The Appendix A contains the details of how this pile-up affects the measured photon spectrum, and how the combined effects of detector efficiency and photon pile-up, were accounted for.

The bremsstrahlung spectrum was recorded at four angles relative to the target as shown in figure 4.1. This was accomplished by rotating the target stage and steering the beam inside the chamber so as to maintain the line of sight through, and outside of, the chamber. No significant attenuation of the bremsstrahlung signal as a result of the target stage was observed for the observation angles through the target.

4.3 Bremsstrahlung Spectrum

Bremsstrahlung spectra for all angles and materials demonstrated a consistent shape as seen in figure 4.2. The high resolution of the measurement was evident in figure 2 (a) which resolves Pb $K_{\alpha,\beta}$ lines as well as a 511 keV positron annihilation line. This was the first measurement of positron production with a 10 mJ laser pulse. The spectral shape was fit as a two effective temperature distribution with exponential effective temperatures of the form $dN/dE = a \times exp(-E/T_b)$ as demonstrated in figure 2 (b). The lower effective temperature, T_{b1} (blue), was fit using a least squares approach between the energies of 120 and 500 keV, while the higher effective temperature, T_{b2} (red), was fit using the same approach between 500 keV and 1 MeV. The highest effective temperatures were observed on an Eu_2O_3 target in the $\theta = -45^o$ specular direction with a normalized vector potential of $a_o = 2.3$ yielding $T_{b1} = 300$ ($\pm$30) keV and $T_{b2} = 550$ ($\pm$60) keV.

Photon pile-up was one of the sources of error in this measurement. A Monte Carlo code was used to model the effect of the detection of multiple photons at the experimental detection rate, and it was shown that the two temperature spectral shape was not a result of pile-up. The details of the effects of photon pile-up on the measurement are provided in the appendix. The error bars were primarily a result of the spectra noise and the effect of photon pile-up. The background signal comprised less than 4% of the total counts in a typical spectrum, and was uniformly distributed across the energy range of 120 keV to 1 MeV. The variation in the signal

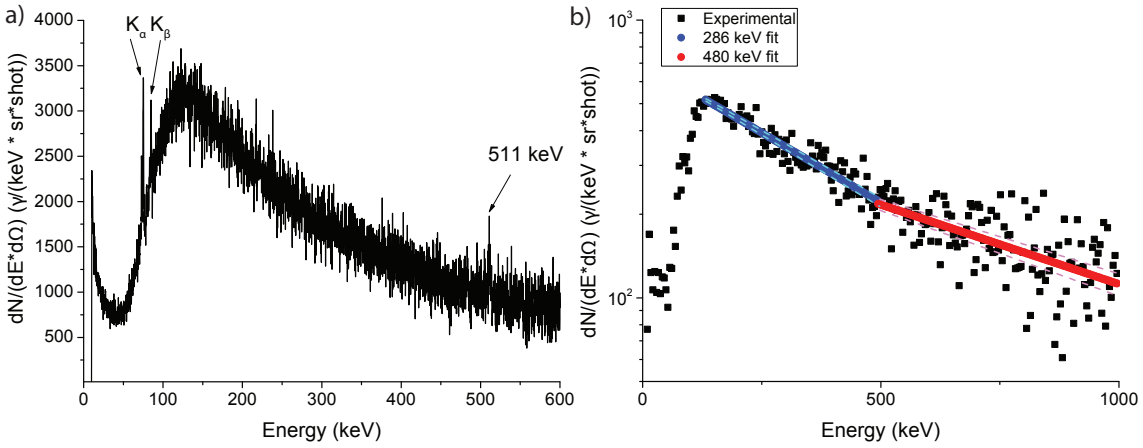

Figure 4.2: a) Eu_2O_3 spectrum accumulated over 1.9 million shots. The resolution is sufficient to resolve nuclear peaks (511 keV) and Pb $K_{\alpha,\beta}$ peaks. b) Bremsstrahlung spectrum showing the characteristic two effective temperature spectral shape for SiO_2 along the specular direction. T_{b1} = 286 (±9) keV (blue) and T_{b2} = 480 (±31) keV (red) are shown along with the 95% confidence fits (dashed lines). The data was taken with $a_0 = 2.3$ over 180k shots. Data is summed into 10 channel bins for clarity.

at high energies was a product of the decreasing signal and the decreasing collection efficiency of the HPGe germanium crystal leading to low count numbers per channel.

The bremsstrahlung temperatures were observed to scale with laser intensity as shown in figure 4.3 (a) with the two temperatures exhibiting similar scalings as a function of the normalized laser vector potential. The temperature scalings exhibited least squares power law fits of $T_{b1} = 101 \times a_0^{1.16}$ keV and $T_{b2} = 149 \times a_0^{1.31}$ keV. The scalings were determined using a linear regression of the measured data in the logarithmic domain. The error bars on each point indicate the standard deviation of the measured temperatures of multiple experimental runs with the same laser parameters, but in some cases different materials. Using a relationship found with MCNPX simulations, $T_e = 0.73 \times T_b^{1.09}$, the experimental electron temperature scaling was calculated from the bremsstrahlung scaling, $T_{e1} = 110 \times a_0^{1.26}$ keV and $T_{e2} = 168 \times a_0^{1.42}$ keV, and compared to existing electron temperature scaling laws as shown in figure 4.3 (b). The slope of the electron scalings was closest to the $T_e = 145 \times a_0^{1.28}$ scaling observed previously on λ^3 [83]. In comparison, Wilks' ponderomotive scaling

has a steeper growth rate in this region of intensity. Alternatively, Beg scaling [81], which was experimentally derived from a variety of picosecond duration laser systems, was also plotted and exhibited a growth rate that was lower than our femtosecond results.

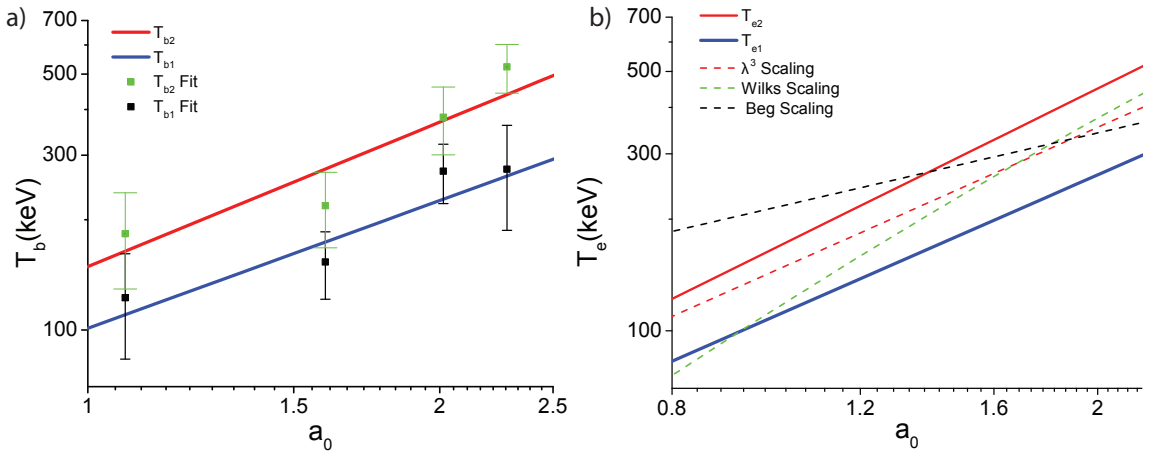

Figure 4.3: a) The T_{b1} (black) and T_{b2} (green) experimental bremsstrahlung temperatures, observed from $\theta = 0^o$ on Eu_2O_3, with the power law fits for T_{b1} (blue) and T_{b2} (red). b) The calculated T_{e1} (blue) and T_{e2} (red) experimental electron temperatures from the bremsstrahlung temperatures in (a) with the Beg (black), λ^3 (red) and ponderomotive (green) theoretical scalings (dashed). The calculated scalings use the relationship between T_e and T_b determined from MCNPX.

The angular distribution of the bremsstrahlung temperature was observed to peak in the specular direction, $\theta = -45^o$, and fall off to a minimum temperature behind the target at $\theta = 90^o$, as shown in figure 4.4. This directionality indicates the specular beam of electrons contained the most energetic electrons, as discussed previously with equation 4.2. The bremsstrahlung and electron directionality was also observed in particle-in-cell simulations and MCNPX modelling, as discussed in the simulation section. This angular distribution is in contrast to previous results with picosecond lasers which have shown highly directional bremsstrahlung signals between $\theta = 45^o$ and $\theta = 90^o$[114].

The experimental bremsstrahlung temperature was observed to be independent of the target material as demonstrated in table 4.1. The measurements were made

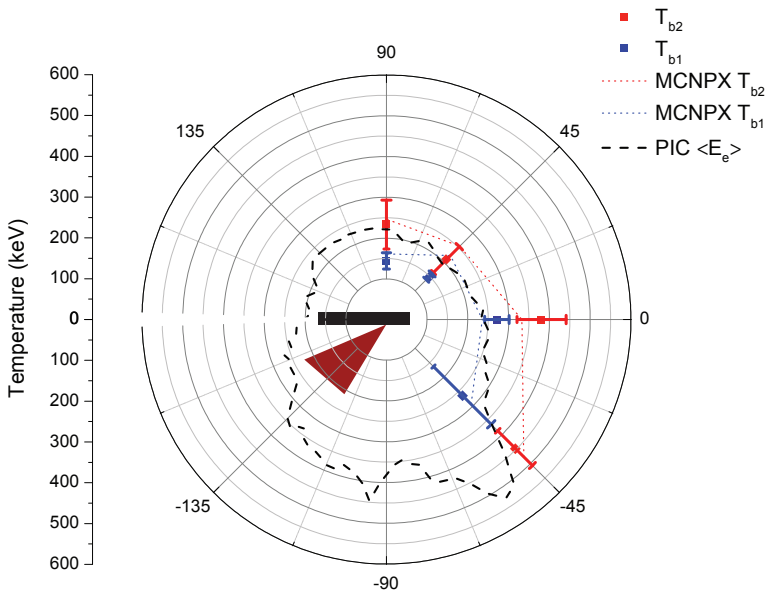

Figure 4.4: Experimental (data points) bremsstrahlung temperatures as a function of observed angle compared to MCNPX predictions (dotted lines). T_{b2} (red) and T_{b1} (blue) are shown, along with the target geometry and laser direction for clarity. The heavy dashed line (black) shows the average electron energy as a function of angle, PIC $< E_e >$ taken from a particle-in-cell simulation.

Material	T_{b1} (keV)	T_{b2} (keV)	MCNPX (keV)
SiO_2	200 ($\pm$30)	292 ($\pm$35)	101
Mo	236 ($\pm$30)	351 ($\pm$30)	121
Eu_2O_3	219 ($\pm$30)	321 ($\pm$30)	144

Table 4.1: Bremsstrahlung temperature along the $\theta = 0^o$ direction compared to MCNPX simulation results for $T_e = 200$ keV. Note the Z dependence in the MCNPX simulation is not observed experimentally.

along the surface ($\theta = 0^o$) direction with $a_0 = 1.6$, and the temperatures from each target material were similar, within the error bars. The temperatures did not exhibit the weak linear scaling with target material observed in MCNPX simulations.

4.4 Simulations

To simulate the absorption of laser energy and generation of the hot electron distribution, 2D particle-in-cell simulations were run using the OSIRIS 2.0 framework [109] under conditions similar to the experiment. The charge density profile was

constructed piecewise from a rectangle function with exponential ramps on the front and rear surfaces. The peak electron density was $n_0 = 30n_c$, where $n_c = \omega_0^2 m_e \epsilon_0 / e^2$ is the critical density for the laser of frequency ω_0, the target thickness was $L = 20c/\omega_0$ and the scalelength of the plasma density was $\lambda_{pp} = 6c/\omega_0$. The target was at a 45 degree angle with respect to the simulation box. A gaussian laser pulse with $a_0 = 1$ was initiated propagating in the x_1 direction, linearly polarized in the x_2 direction with a waist of $w_0 = 8c/\omega_0$ (1 μm) and a 5th order polynomial temporal shape with a duration of $\omega_0 t_0 = 65$. Two particle species were used; species 1 with charge to mass ratio $q/m = -|e|/m_e$ initiated with a thermal velocity of $v_{th} = 0.01c$ and species 2 with $q/m = +10|e|/28m_p$ initiated at rest, where m_p is the proton mass. 64 PPC with cubic weighting were used for species 1 and 4 PPC with linear weighting were used for species 2. The domain, of dimensions $x_1 \times x_2 = 30 \times 15$ μm^2 was divided into 5000×2496 grid cells, yielding cell sizes $\Delta x_1, \Delta x_2 = 0.048c/\omega_0$. The simulation was run for $\omega_0 t = 1000$ in steps of $\omega_0 \Delta t = 0.033$. Compensated binomial smoothing was applied to fields and currents on the grid.

Fig. 4.4 shows the electron average energy as a function of angle, (PIC $< E_e >$) taken from the particle-in-cell simulation. For a 2D velocity distribution, the average energy and temperature are equivalent for a Maxwell-Boltzmann velocity distribution. The mean energy was used to allow a quantitative comparison between the simulation electron energies and the experimental bremsstrahlung temperature because the electron distribution was non-Maxwellian. The average energy was calculated by taking the average of electron energies E for each angle above a cut off energy E_{lower} from the momentum phase space, i.e., the numerical equivalent of $\int_{E_{lower}}^{\infty} \int_{\theta-\Delta\theta/2}^{\theta+\Delta\theta/2} f(\theta, E) E d\theta dE$, where $\Delta\theta$ is the bin width. The figure shows the average energy of electrons above a 100 keV cut-off. The simulated electron distribution shows two populations of electrons, a near isotropic component of heated electrons and a population with higher average energy that is accelerated in the near specular

direction in a chaotic direct laser acceleration mechanism by the reflected/incident waves interacting with the surface plasma, as previously observed at lower intensity [83].

The Monte Carlo code MCNPX [119] was used to simulate the relationship between the electron and bremsstrahlung spectra. MCNPX uses tabulated bremsstrahlung production tables based on the Bethe-Heitler Born-approximation [106] and applicable models have been developed in the literature [21, 107]. While the model emphasizes the MeV region, subsequent improvements have been made for the keV region [120]. The MCNPX simulations modeled the target, chamber wall, air and detector locations with the appropriate geometry. A multiplication factor of 100 was used for bremsstrahlung production in the electron physics model to reduce the simulation run time by increasing the photon production per simulated electron. The accuracy of this method was validated by a run without multiplication which showed no discernible difference in effective bremsstrahlung temperatures. Photons were recorded with surface current tallies at the detector positions, which were located at the same distance and angle as the experimental detectors. All runs used 1.4×10^8 electrons with standard Maxwellian energy distributions which were directed in isotropic spheres, 7^o half angle cones, or both. The cone source contained a uniform flux through all angles encompassed by the 7^o half angle. Half angle beams were modeled in the specular (-45^o), laser (45^o) and target normal (90^o) directions. MCNPX simulations confirmed the correlation of the bremsstrahlung directionality with the electron direction, as predicted by the analytical model. This reinforced the conclusion that the highest energy electrons were contained in the specular beam.

The two electron populations observed in the PIC simulations were investigated and compared to the experimental results. Fig. 4.5 shows the calculated bremsstrahlung signal from separate sources of an isotropic sphere (T_e = 200 keV) and a cone (T_e = 900 keV) from a Eu_2O_3 target. The combination of the two signals can accu-

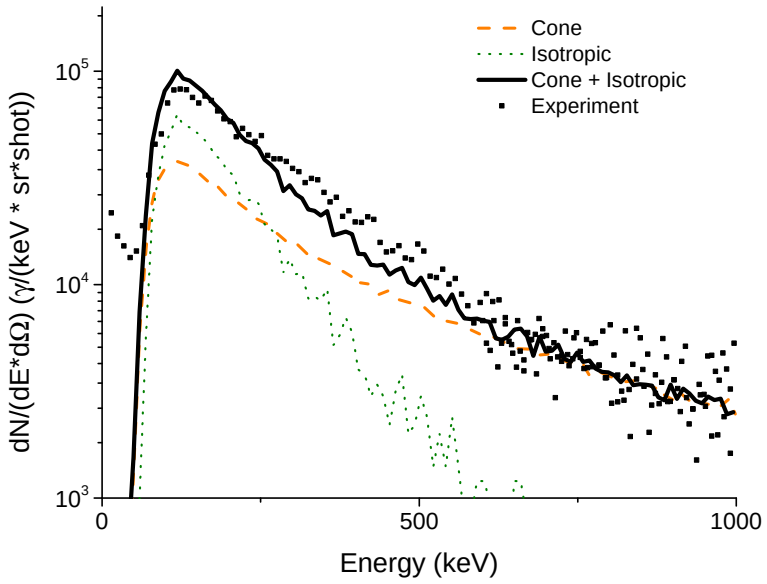

Figure 4.5: MCNPX results demonstrating the effect of two electron sources. The combination of two sources with different temperatures reproduces the two temperature bremsstrahlung signal observed experimentally.

rately reproduce the experimentally observed two temperature spectra for Eu_2O_3 at $a_o = 2.4$ by providing different effective temperatures from the two electron populations. This demonstrates the importance of measuring the electrons accelerated in all directions, both into and out of the target, in order to fully characterize the electron behavior.

The angular characteristics of the bremsstrahlung radiation shown in figure 4.4 were reproduced in MNCPX using the PIC electron distribution. The electron source was modeled as a combination of an isotropic source with a Maxwellian temperature of 200 keV and a beamed source with a temperature of 700 keV directed in the -45^o direction. It was observed that the result was very sensitive to the beamed source temperature, but only weakly dependent on the isotropic distribution. This can be attributed to the larger number of measurable photons from the higher energy source, whereas the photons from the isotropic source tended to be absorbed on the way to the detector.

In order to compare the scalings of the bremsstrahlung and electron tempera-

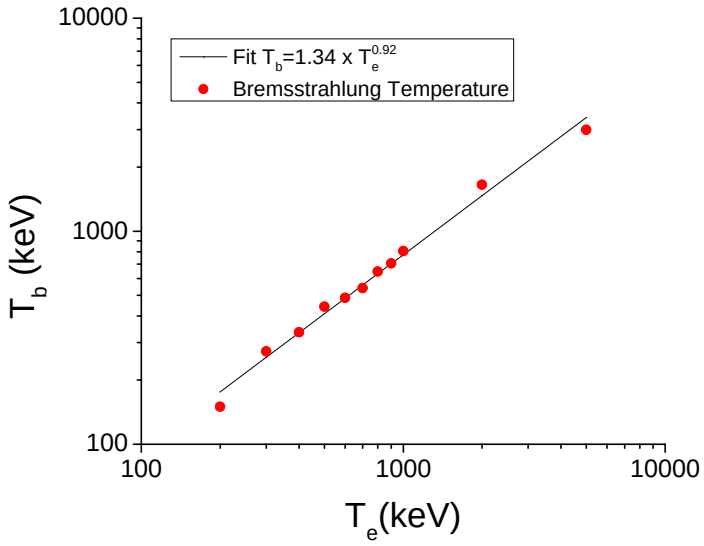

Figure 4.6: MCNPX results showing the relationship between T_b and T_e for 3.5 mm of stainless steel.

tures, the relationship between the Maxwellian electron temperature and the effective bremsstrahlung temperature was determined for electron temperatures spanning the range 200 keV to 5 MeV. The relationship was observed to scale as $T_b = 1.34 \times T_e^{0.92}$ keV , as shown in figure 4.6, for an electron beam directed into a 3.5 mm steel slab and observed through the slab. MCNPX was also used model the effect of different target materials on the bremsstrahlung temperature. A weak linear material scaling of the temperature with target material atomic number was observed when electron beams were propagated through a slab of material. This further reinforces the fact that the experimental bremsstrahlung signal temperature was predominantly influenced by the specular electron beam, which did not interact with the target material, leading to no observation of temperature scaling with different target materials.

4.5 Activation

A ^{238}U sample was placed in the specular beam direction in an attempt to measure (γ, n) activation. The 3.8 g sample was irradiated for 60 thousand shots. The sample

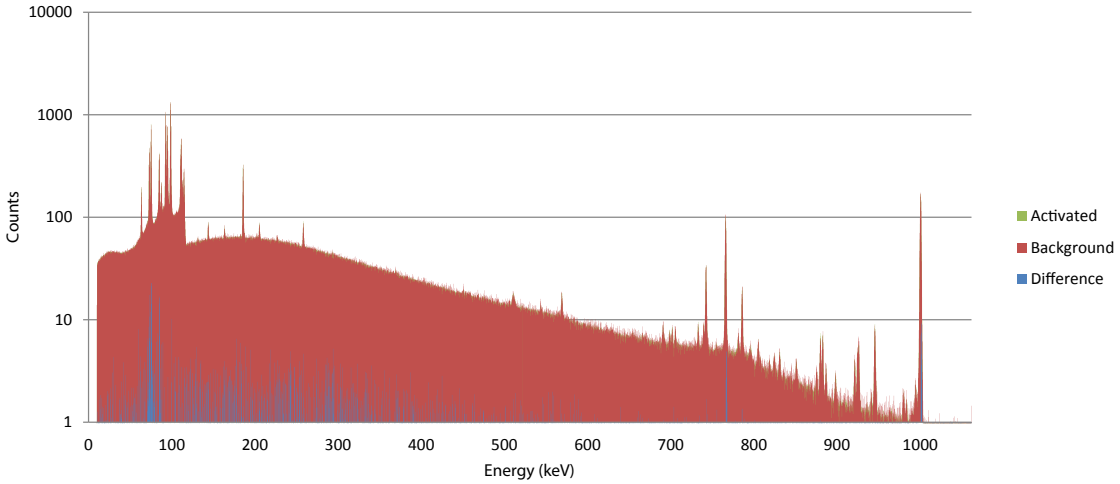

Figure 4.7: ^{238}U spectra measured with the HPGe detector. The activated (green) spectrum is nearly overlapped with the background (red) spectrum. The difference between the two spectra (blue) shows a slight increase in K_α signal, mostly from Pb.

was then placed in front of the HPGe detector to measure the gamma spectrum over a 3 hour time period. The spectrum, shown in Fig. 4.7, was nearly identical to a reference background spectrum that had been measured prior to activation of the sample. If measurable activation of the sample had occurred, the spectrum would have contained new peaks that resulted from the decay of the fission fragments generated by the laser activation of the sample. A small increase in Pb K_α and K_β radiation, from the shielding, was observed. No increase in the U K_α or K_β radiation was observed. This was attributed to the much larger mass of the shielding Pb (10's of kg), as compared to the small ^{238}U sample.

4.6 Conclusion

The results of a systematic high resolution measurement of bremsstrahlung scaling in ultrafast laser-solid interactions with thick targets have been presented. The high resolution HPGe detector measurement was shown to be able to resolve nuclear linewidths which may allow the detection technique to be used to measure short lived

isomers and isotopes. The bremsstrahlung spectrum exhibited a characteristic two temperature shape. The two temperatures, T_{b1} and T_{b2}, were observed to scale with the λ^3 scaling. The effective bremsstrahlung temperature was not observed to depend on the target material, which was corroborated with MCNPX simulations.

The MCNPX and PIC results confirm the overall population of electrons was well characterized by an isotropic source with a high energy beam directed in the specular direction. The importance of accounting for both the electrons that escape the target and the electrons that propagate into the target, as well as the sensitivity of this measurement technique to both populations, was shown through MCNPX simulations. These results lead to the conclusion that the isotropic population produces the T_{b1} temperature through the ponderomotive expulsion of electrons from the focal spot of the laser, while the specularly beamed electrons experience chaotic acceleration, as previously mentioned, and produce the T_{b2} temperature. The scaling was also observed to be slower than Wilks ponderomotive scaling, which is consistent with theoretical works that postulate lower temperatures [83] [82] [121] [71].

The electron directionality, along with the higher observed intensity scaling than Beg scaling, suggest a significant difference between the coupling of laser energy into electron motion for picosecond and femtosecond duration interactions. This also suggests that the discrepancy between femtosecond and picosecond electron directions can be attributed, in part, to the specular acceleration mechanism, which can not be supported during picosecond duration interactions due to the distortion of the critical surface. Additionally, the presence of a higher temperature scaling, consistent with previous femtosecond laser interactions, suggests further studies of the bremsstrahlung scaling at higher intensities may yield higher temperatures than picosecond lasers.

This has several implications for homeland security applications. The specularly directed beam suggests the optimal location of a interrogation target is along the

specular direction. Additionally, since the electrons accelerated in this direction leave the solid target it may be possible to optimize the bremsstrahlung conversion efficiency by placing thin high Z targets in the path of the electrons. Activation of ^{238}U, which requires >4 MeV photons, was not observed. Increasing the number of higher energy photons would require higher laser intensity, without reducing the repetition rate, which should be possible with laser systems in the near future.

CHAPTER V

Proton Acceleration from Structured Targets

5.1 Introduction

Understanding the propagation of energetic electrons from short-pulse laser matter interactions with solid density targets is critical for particle accelerator applications. The electron induced sheath field, as described in Section 2.3.1, has been observed to extend millimeters from the interaction point in foil targets[122]. As the sheath extends across the target surface the field strength decreases. Confinement of the sheath to a target with a limited surface area has the potential to increase the field strength, and therefore the proton energies. The effect of three dimensional target perturbations on the electron sheath and proton acceleration was investigated through the use of foil, grid, and wire targets using HERCULES.

Mass limited targets have previously been used increase proton energies by decreasing the volume of the target and thereby increasing the hot electron density within the target. Refluxing, or recirculation, of electrons in thin foils has been shown to increase electron [123] [124] and proton energies [125] [126]. Computational studies have also predicted new acceleration mechanisms in spherical mass limited targets leading to the generation of quasimonoenergetic proton beams [127] and electron beams [128]. While it is straightforward to simulate an isolated, limited mass target, it is quite difficult to reproduce this situation experimentally. To date, ap-

proaches have included suspending small targets on glass stalks [129] [130] or ultrathin wires[131], and using micron scale droplets[132][133][134].

In short pulse interactions hot electrons primarily move along surfaces, as a result of confining electric fields, and lose energy to the fields. Computational studies have investigated the effect of mass limited targets on proton energies for pulse durations long enough to allow transversal electron recirculation [135] leading to enhanced ion acceleration from additional acceleration of electrons. Improved conversion efficiency [131] and enhanced proton energies have been observed in experiments [136] with laser pulse durations of 100's of fs. For laser pulse durations of 10's of fs enhanced proton energies have been predicted as a result of the concentration of hot electrons [137]. However, this has not been observed experimentally [138], which has been attributed to preplasma formation effects on small targets due to insufficient laser contrast [139].

While the benefits of mass limited target would be highly desirable, the use of more traditional targets would be beneficial for applications. Here we consider the effect of controlling the surface area of the targets, without limiting the target mass through isolation, and observe the effects of the changing the ratio of the surface area to the target volume.

5.2 Experimental Setup

The experiment was performed using the HERCULES laser facility at the University of Michigan. The chamber schematic is pictured in Fig. 5.1. The laser delivered 1.7 ($\pm$0.2) J to the target in a 2.7 μm FWHM focal spot via an $f/3$ off-axis parabolic mirror. This resulted in an average on-target intensity of 7.6×10^{20} W/cm^2 ($a_0 = 19$). A near diffraction limited spot size with a Strehl ratio of 0.6 - 0.8 was attained by using a deformable mirror (Xinetics) and a Shack-Hartmann wave front sensor. The HERCULES laser operates at a 0.1 Hz repetition rate, although the experiment was conducted at 0.01 Hz.

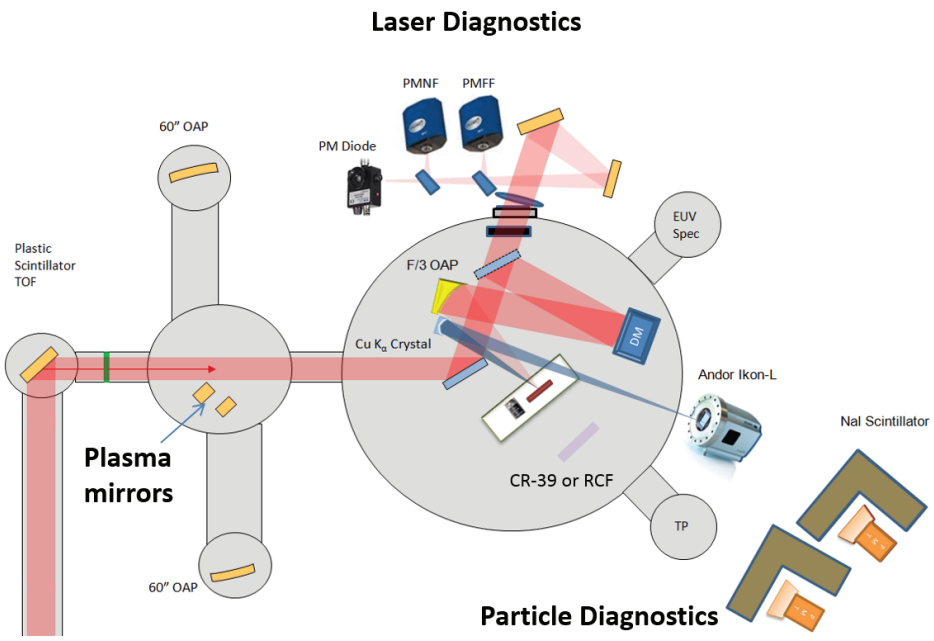

Figure 5.1: HERCULES solid target area chamber schematic. Plasma mirrors were not used in this experiment.

In this experiment three target geometries were investigated. The effect of different target shapes was measured by varying the target geometry while maintaining the approximate target thickness. The three targets were selected to approximately maintain the target thickness. The foil target was 12.5 μm thick copper. The mesh target was a square copper grid target purchased from SPI supplies (SPI# 2140C). The mesh had a 62 μm pitch with 8 μm bar width and was measured to be 9 $\pm$1 μm. The wire target was 15 μm diameter copper. Transverse alignment of the mesh and wire targets required few micron precision to overlap the focal spot and the 8 μm width mesh bars. This was accomplished by imaging the location of the focused low energy regenerative amplifier laser seed pulse on the target.

The primary ion diagnostic was CR-39 located normal to the target on the rear side. Mylar filter stacks were used to measure proton flux in multiple energy bins, allowing the measurement of a proton energy spectrum. Each bin acted as a high pass filter yielding a proton signal above the energy cut-off. CR-39 was placed at

distances of 1 or 5 cm from the target to measure the proton beam profile or 45 cm from the target to measure the energy and flux.

Cu K_α emission from the targets was imaged using a spherically bent Quartz[21**3**1] crystal with a $2d = 3.082\mathring{A}$ lattice spacing. The crystal, which had a 400 mm bending radius, was placed 242 mm from the target and produced an image at 1260 mm, yielding a magnification of 5.2. An Andor iKon-M BR-DD was used to detect the imaged photons. The CCD had 13 μm pixels and a quantum efficiency of 45% at the Cu K_α energy. The imaging system was aberration limited to a resolution of 15 μm with a 25.4 mm aperture. The absolute photon yield was calculated using the manufacturer specified CCD response and crystal's integrated reflectivity.

5.3 Ion Acceleration and Electron Dynamics

The Cu K_α images measure the relative magnitude and location of hot electrons within the target material as shown in Fig. 5.2 (a)(b)(c). The total Cu K_α flux was remarkably consistent between targets, varying from 9.5×10^9 to 1.07×10^{10} photons in the three images in Fig. 5.2, which is consistent with laser shot-to-shot fluctuations. The total conversion efficiency into Cu K_α was 1×10^{-5}, consistent with previous results [140] [141]. The observation that the spatial extent of the Cu K_α was approximately equal for each target indicated the hot electrons lost their energy to field, as opposed to collisions within the target.

Previous studies of the effects of reduced volume on Cu K_α yield have shown a reduction in K_α yield for lower volume targets [142] [143]. This was partially attributed to broadening and shifting of the K_α emission as a result of heating. However, this was observed for longer pulse durations (10 ps) and higher pulse energies (>75 J) than in the present experiment, for the same volume targets, which would lead to more target heating. A reduced K_α signal was not observed for the investigated targets, indicating the target heating was insufficient to alter the K_α emission.

The confinement of K_α signal in the mesh and wire targets led to a higher signal density since approximately the same total Cu K_α signal was observed for the targets with smaller surface areas. The vertically integrated profile (d) of the images shows the wire and mesh are very similar since they have the same horizontal profile. The mesh target has higher signal at the vertical segments and lower signal in between, but yielded approximately the same overall signal. This was an important result because it showed the conversion efficiency of electrons into each target was approximately the same and that any difference in the proton signal was a result of how the electrons were confined to the target and then influenced sheath fields.

The proton spectra, shown in Fig. 5.3, were well characterized by exponential fits. The lines of best fit were $Y_{foil} = 3 \times 10^8 \times exp^{-0.496*E}$, $Y_{mesh} = 6 \times 10^6 \times exp^{-1.238*E}$, and $Y_{wire} = 3 \times 10^9 \times exp^{-2.481*E}$, where E was the energy of the protons. The effective temperature of the spectra increased as the target volume was reduced from the foil to the mesh to the wire. This result indicated that as the electrons were confined to a smaller target the field strength increased, accelerating protons to higher energies.

While the effective temperature demonstrated a clear trend, the total proton flux was lowest for the mesh target and approximately equivalent for the foil and wire targets. As the surface area of the target decreased it was expected that, while the sheath fields were stronger in magnitude, the overall area, and thus the number of accelerated protons would decrease. While this partly explains the mesh data, a reduced flux was not observed for the wire target. The expected reduction in flux for the wire target was counteracted by an azimuthal magnetic field which created a line focus in the proton spatial distribution, as shown in Fig. 5.4 (b). The line focused protons were observed 1 cm and 5 cm from the target, with the same 7^o full-width-full-angle vertical divergence. This focused divergence was considerably smaller than the full beam 54^o full-width-full-angle divergence for the protons that were not focused. It was also much smaller than the 40^o full-width-full-angle proton

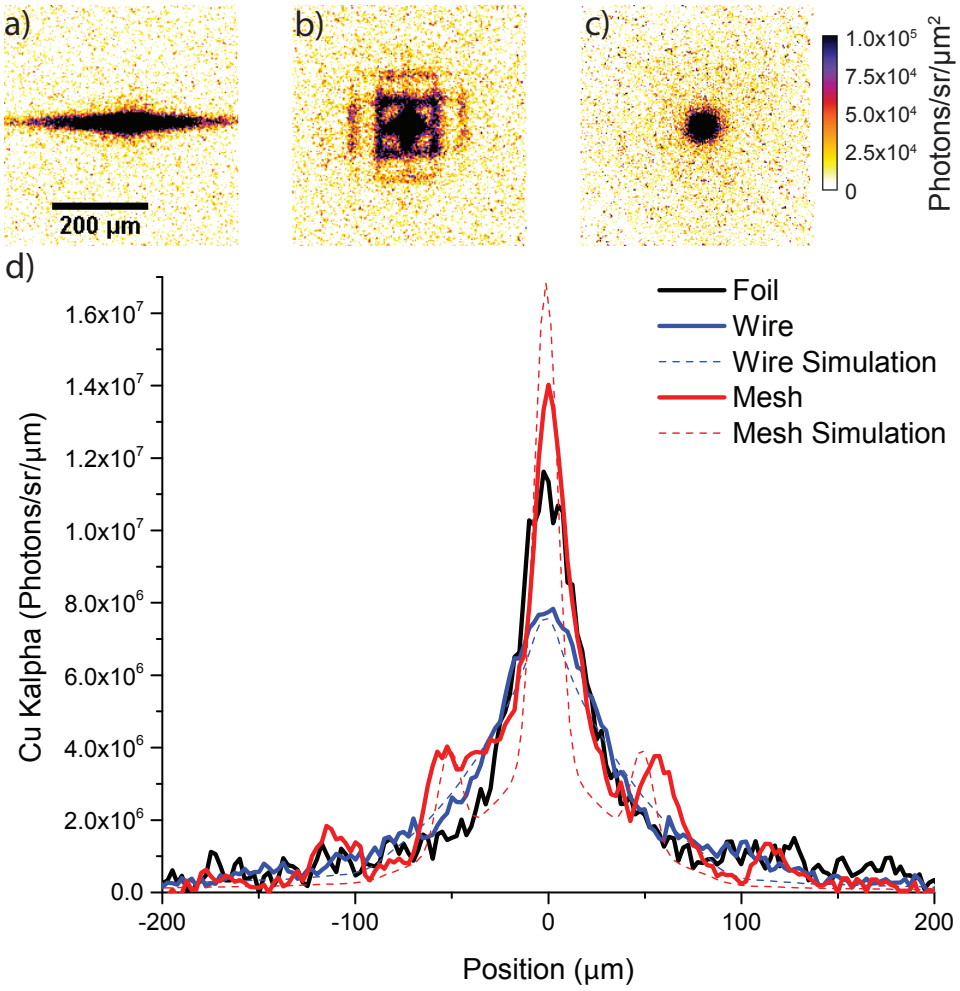

Figure 5.2: Cu K_α images of (a) wire (b) mesh and (c) foil targets. The confinement of electrons due to the target geometry leads to strong electron currents that illuminate the target. Vertically integrated profiles of the images (d) show how the signal is distributed. Dashed lines represent the scaled simulation results and show excellent agreement.

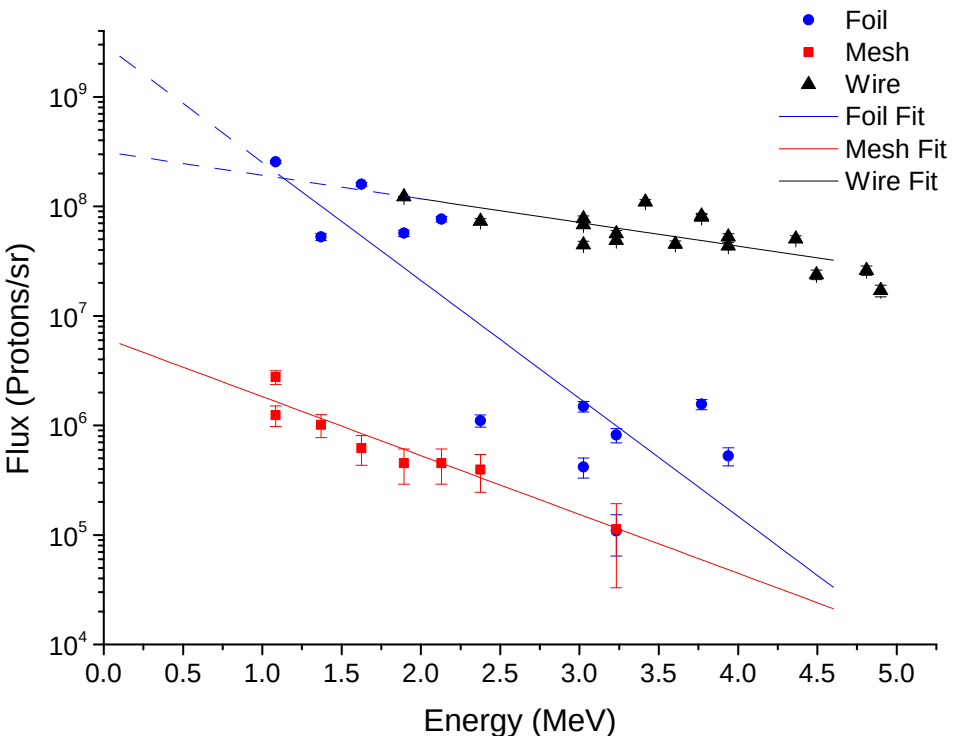

Figure 5.3: Ion spectra from (triangle) wire (square) mesh and (circle) foil targets. The values represent the flux of protons above the threshold energy for the filter stack. The slope of the lines of best fit decreases from the foil to mesh to wire target. The dashed portions of the fits continue to fluxes higher than the saturation point of the CR−39 detector.

beam observed from flat targets. The focused protons were sampled for the energy spectra.

The target mesh pattern was observed in the proton flux on CR-39 placed 1 cm behind the target, as shown in Fig. 5.4 (a). This image was interesting because it confirmed that the electrons that produced Cu K_α on neighboring segments of mesh around the focal spot were also accelerating protons. Additionally, it confirmed that the extent of the Cu K_α signal was approximately the extent of the sheath field that contributes to proton acceleration.

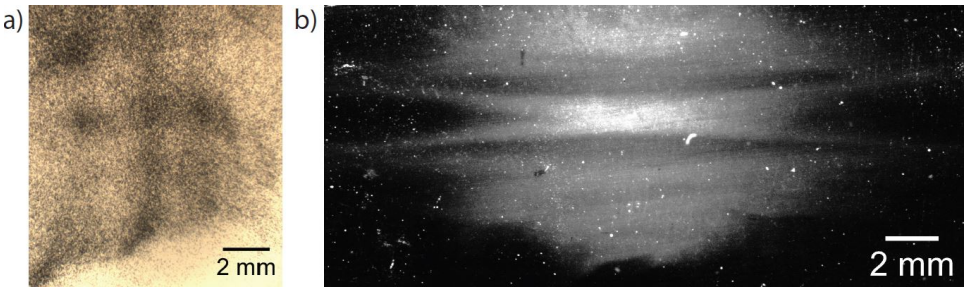

Figure 5.4: Microscope image of CR−39 located 1 cm from a mesh target (a) showing mesh pattern in the proton distribution. Scan of CR−39 from a wire target (b) showing a line focusing feature in the proton distribution 1 cm behind the target. The orientation of the focused line was perpendicular to the orientation of the wire target. This feature was also observed 5 cm behind the target with the same angular divergence.

5.4 Simulations

To help understand the experimental results simulations were performed for two different target geometries using the hybrid Vlasov-Fokker-Planck code, FIDO [121]. Excitation of K shell vacancies was calculated from collisions between the fast electron population and the background fluid [144]. The simulation domain consisted of a box of dimensions $L_y = 100$ μm by $L_x = 200$ μm in an (x, y) 2D slab geometry. The copper targets were represented by piecewise hyperbolic tangent functions. The initial temperature of the bulk target was $k_B T_e = 400$ eV. A cut-off was introduced such that $\ln \Lambda_{ei} = 2$ if the calculated value would be less than 2. The boundary conditions were reflecting and the last few grid points had an exponentially increasing step size.

An isotropic population of electrons were injected into a 5 μm region at the center of the domain with a full width at half maximum temporal duration of 40 fs. The electron beam momentum distribution was defined as in ref. [121] with p a shifted Gaussian with center momentum $p_0 = \left(\sqrt{1 + a_0^2} - 1\right) 2 m_e c^2/3$ [80]. a_0 was chosen to be representative of a laser with an intensity of 2×10^{19} W cm^{-2}, but with a larger focal area in order to match the laser energy from the experiment, with the injected electron beam number density being calculated using the effective laser energy with

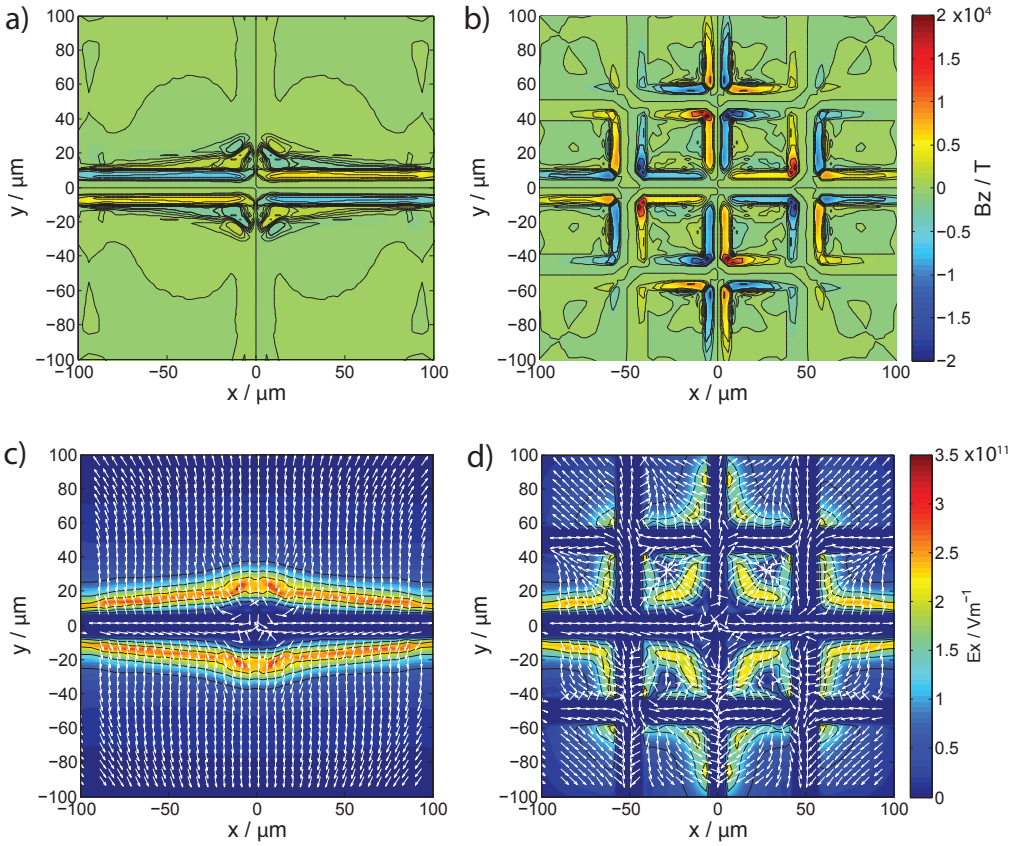

Figure 5.5: Data from Vlasov-Fokker-Planck simulation for representations of (a,c) wire and (b,d) mesh targets. The (a,b) magnetic fields are shown at 500 fs and the (c,d) electric fields are shown at 600 fs . Arrows indicate the direction of the electric fields.

an assumed 0.3 absorption fraction.

An azimuthal magnetic field was observed around the wire target, as seen in Fig. 5.5 (a). The field switched orientations around the interaction point due to the change in current directions. This field geometry was consistent with the observed proton focusing. In the grid target azimuthal fields were also observed. However, the crossing segments broke up the collective focusing structure.

The spatial extent of the fields was also observed to be consistent between the wire and the mesh, as observed experimentally. The wire target electric field strength, shown in Fig. 5.5 (c), peaked at 2.9×10^{11} V/m, while the mesh target maximum,

shown in Fig. 5.5 (d), was only 2.2×10^{11} V/m. The higher wire field strength was consistent with the experimentally observed wire proton temperature increase. The laminar field structure around the wire target led to efficient acceleration of protons. The low proton flux from the grid targets could be partially attributed to the complex field structure, around the intersection points, which could accelerate protons in a wider divergence angle than the other two targets.

5.5 Conclusions

In conclusion, proton acceleration has been studied using structured targets with reduced surface areas. All targets were observed to produced nearly the same total Kα photon yield over the approximately the same spatial extent, indicating the hot electrons were slowed by the fields. Hot electron density increased as the target surface area was reduced and was correlated to an increase in the temperature of the accelerated proton beam. The relative field strength observed in simulations confirmed the higher proton energy from the wire target was a result of the increased electric field strength. The profile of the grid target was observed in the accelerated proton beam profile and confirmed that protons were accelerated from the same regions that produced K_α photons.

The low proton flux observed with mesh targets was attributed to the complex field structure around the intersection points, and the reduced target surface area. Focusing of proton beams was observed from the wire target. Simulations suggest the focusing was the result of azimuthal magnetic fields that resulted from the surface current. In the grid target the field symmetry was broken by the crossing segments and no focusing was observed.

These results have several potential implications for laser plasma accelerators. The increased proton energies, without the use of complex mass limited targets, could be used to enhance proton energies without the need for higher energy lasers.

The focusing effect could lead to higher proton beam flux, which could lead to more efficient proton accelerator applications. The use of targets with small surface areas pairs well with femtosecond lasers which typically achieve high focal intensity through sharp focal optics and few micron scale focal spots.

CHAPTER VI

Neutron Generation

6.1 Introduction

Homeland security applications require neutrons with energies of a few MeV to 15 or 20 MeV due to the (n, f) cross sections for fissile, fissionable, and naturally occurring materials, as shown in Fig. 6.1. Neutron beams with these energies also have applications in neutron radiography [145], imaging [146], and fast neutron therapy [147]. Many previous experiments have demonstrated the production of neutrons from laser based acceleration mechanisms, but they have typically been conducted at high laser energy, 10's to 100's of Joule, low repetition rate facilities, producing very low time averaged fluxes. In this chapter, the production of neutrons with the relatively high repetition rate HERCULES laser system at ultra-high intensities is reported [148].

Previous work has investigated neutron generation using ${}^{2}_{1}\mathrm{d(d,n)}{}^{3}_{2}\mathrm{He}$ reactions (D-D) [59],[149],[150], as well as ${}^{7}_{3}\mathrm{Li(p,n)}{}^{7}_{4}\mathrm{Be}$ reactions (P-Li)[55], [57], and, more recently, ${}^{7}_{3}\mathrm{Li(d,n)}{}^{8}_{4}\mathrm{Be}$ reactions (D-Li)[56]. The (D-Li) reaction has a large positive Q value (15 MeV) that upshifts the neutron spectra but requires the acceleration of deuterons into Li instead of protons. This can be accomplished through acceleration of deuterons from the bulk of a deuterated target[56], however surface contaminants, which do not contain deuterons, tend to be preferentially accelerated over bulk ions. This effect

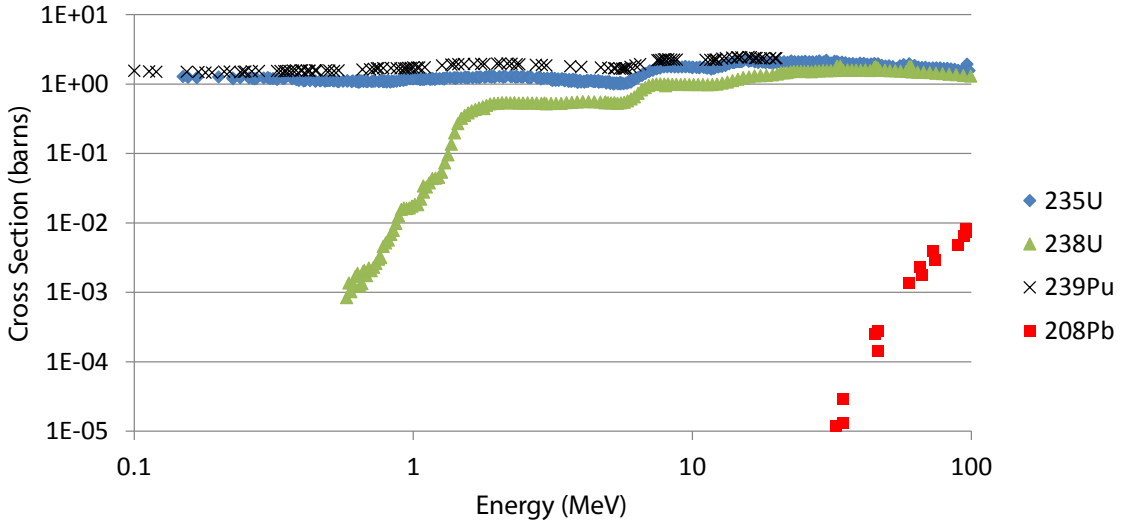

Figure 6.1: The (n, f) cross sections for common fissile, ^{235}U (blue) and ^{239}Pu (black), fissionable, ^{238}U (green), and naturally occuring, ^{208}Pb (red), materials. The optimum neutron interrogation energy is above the fissionable material threshold energy, MeV's, and below the naturally occurring materials, 10's of MeV.

can be harnessed through the introduction of additional surface contaminants which contain deuterium[151]. In this chapter the results from two methods of introducing deuterated surface contaminants are presented and show it is possible to efficiently accelerate an ion beam in which deuterons comprise >99% of the accelerated light ions and yield ≤ 3 $(\pm 1.4)\times 10^6$ neutrons/sr with energies up 16.8($\pm$0.3) MeV[152].

6.2 Experimental Setup

The experiment was performed using the HERCULES laser facility at the University of Michigan. The chamber schematic is pictured in Fig. 6.2. The laser delivered 1.1 ($\pm$0.4) J of P-polarized light to the target in a 1.3 μm FWHM focal spot via an $f/1$ off-axis parabolic mirror. This resulted in an average on-target intensity of 2×10^{21} W/cm^2 with a normalized vector potential of $a_0 = 30$. A near diffraction limited spot size with a Strehl ratio of 0.6-0.95 was attained by using a DM (Xinetics) and a Shock-Hartmann wave front sensor. The HERCULES laser operates at a 0.1

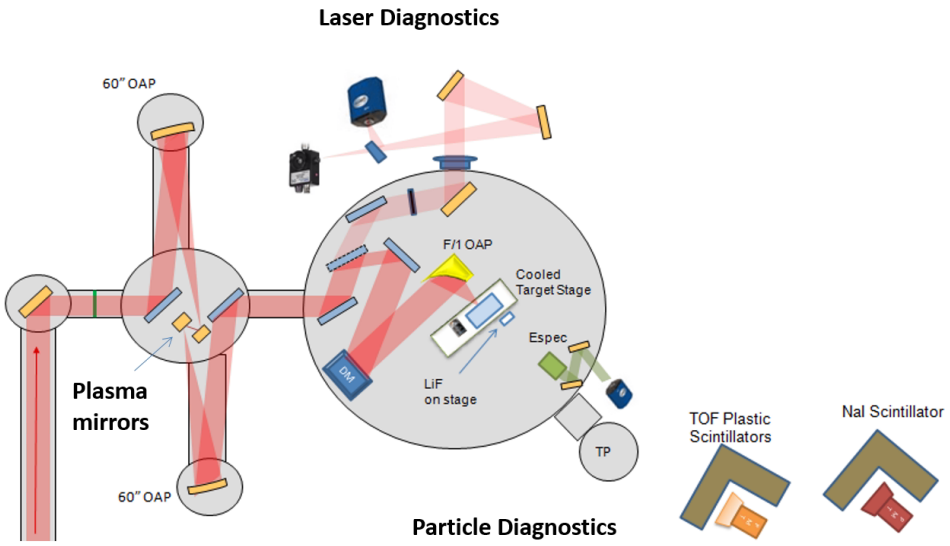

Figure 6.2: HERCULES solid target area chamber schematic. nToF plastic scintilator location is not to scale.

Reaction	Reaction Equation	Target and Catcher	Q Value
(D,D)	${}^{2}_{1}d + {}^{2}_{1}d \rightarrow {}^{3}_{2}He + {}^{1}_{0}n$	1.5($\pm$0.5) mm CD	3.27 MeV
(P,Li)	${}^{1}_{1}p + {}^{7}_{3}Li \rightarrow {}^{7}_{4}Be + {}^{1}_{0}n$	100 nm $(C_2H_4)_n$ + LiF	$-$1.64 MeV
(D,Li)	${}^{2}_{1}d + {}^{7}_{3}Li \rightarrow {}^{8}_{4}Be + {}^{1}_{0}n$	3 μm Mylar with $(C_8D_8)_n$ Paint + LiF	15.03 MeV
(D,Li)	${}^{2}_{1}d + {}^{7}_{3}Li \rightarrow {}^{8}_{4}Be + {}^{1}_{0}n$	800 nm Al with D_2O Ice + LiF	15.03 MeV

Table 6.1: Nuclear reactions and target configurations investigated on HERCULES. The (D,D) reaction used the thick target material for the deuteron source and converter. The other reactions used thin target and a LiF catcher.

Hz repetition rate, although the actual experiment was conducted at 0.01 Hz due to the need to record data between shots.

In this experiment three nuclear reactions for neutron production, D-D, P-Li, and D-Li, were investigated using four different schemes. The reactions and target configurations are summarized in Table 6.1. The D-D reaction was investigated using bulk targets that were made from compressed Deuterated Polyethylene (CD), mainly comprising carbon and deuterons, with a thickness of 1.5($\pm$0.5) mm. The thick CD target was simultaneously a source of accelerated deuterons and converter deuterons, which simplified the target configuration. The dominant acceleration mechanism was ponderomotive front-side acceleration [54], due to the target thickness, which

was confirmed by the observation of neutrons which came from deuterons that were accelerated into the target.

Higher ion energies and improved ion flux can be achieved on femtosecond lasers by exploiting TNSA [153] with thin film targets, as discussed in Section 2.3.1. Parylene 100 nm thin film targets were used to produce TNSA protons for the P-Li reaction in a pitcher-catcher configuration with an 0.85 cm thick LiF catcher. The negative Q value of the P-Li reaction downshifted the neutron spectra which was obviously undesirable. In contrast, the D-Li reaction had a positive Q value which upshifted the neutron spectra but required the acceleration of deuterons into the catcher instead of protons. This required the introduction of a deuteron rich contaminant layer on the surface of the target which was accomplished through two methods. In one technique, developed by Willingale *et al.*[58], denoted D-Li (Paint), 3 μm Mylar targets were "painted" with a solution of deuterated polystyrene deposited on the rear surface with a thickness <1 μm. Since this could not be done *in situ* this technique had the disadvantage of allowing sufficient time for a proton rich contaminant layer to re-form over the painted area, which inhibited deuteron acceleration [154]. Alternatively, using an approach pioneered by Hou *et. al.* [151] and further developed by Morrison *et al.* [155] and Maksimchuk *et al*[156], denoted D-Li (Ice), 800 nm Al targets were cryogenically cooled to allow D_2O water vapor to freeze to the target front and rear surface, forming a deuteron rich contaminant "ice" layer which was proton free and dramatically enhanced the number of accelerated deuterons. The accelerated ions propagated into a 0.65 mm LiF catcher and the geometry of the pitcher-catcher configuration is pictured in Fig. 6.3.

Aluminum targets were selected for their high thermal conductivity. The aluminum targets were held between two pieces of perforated aluminum metal sheets with 0.8 mm thickness. The target holder was cooled to $120^o - 180^o$ K which is significantly below the sublimation point of water, 200^o K, at the pressure of the

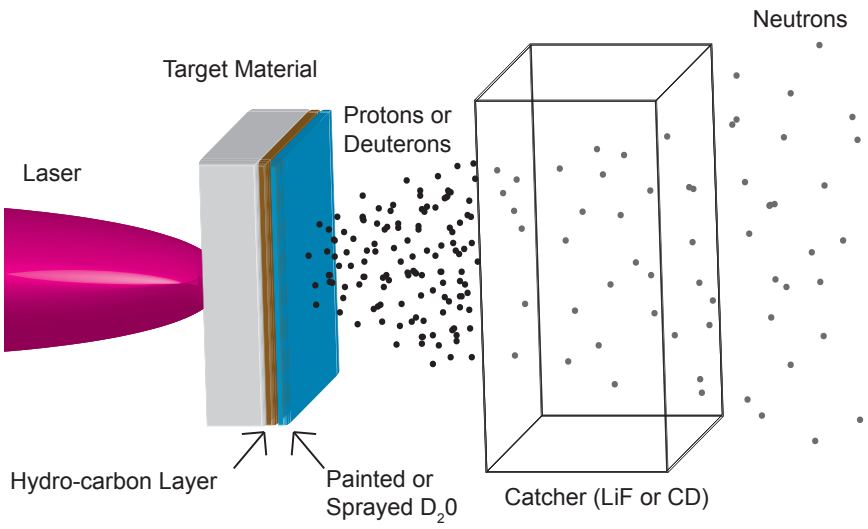

Figure 6.3: Sketch of the target and catcher configuration. The laser interacted with the front side of the foil and accelerated ions from the rear surface, through TNSA, into the catcher. The deuterated ice contaminant layer formed a distinct layer over the hydrogenous contaminants for the D-Li (Ice) target, but was not as well defined for D-Li (Paint).

target vacuum chamber 1×10^{-4} Torr. The aluminum targets and target holder were selected for their high thermal conductivity.

The primary neutron diagnostics were the nToF detectors discussed in Section 3.4.3. A combination of ϕ16 cm and ϕ35.5 cm scintillators, made from EJ-204 and EJ-200 plastic, respectively, were used. The smaller detectors were placed at distances of 2.75 and 3.28 meters from the target, while the larger detector was located at 9.45 meters. The nToF detectors were located in the forward direction within a 15^o cone. A large number of relativistic electrons were accelerated during the ultra-intense laser interaction which generated a temporally short duration pulse of high energy photons. It was necessary to shield the detectors with 10 and 5 cm of lead, respectively, in order to prevent the prompt photon signal from obscuring the neutron signal. The scintillator time constants, 1.8 and 2.1 ns, respectively, in combination with the long stand off distances were optimized to allow the nToFs to measure neutrons with energies from 0.5 to >20 MeV, depending on the strength of the photon flash. A

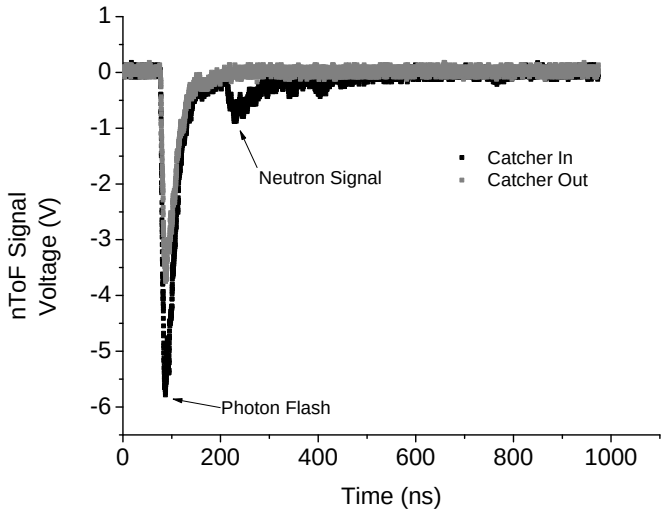

Figure 6.4: Raw nToF data from the detector at 9.45 m with (black) and without (grey) the LiF catcher. In the absence of the catcher the photon flash showed a smooth decay without additional scattered photon signal or signal reflections. The LiF catcher shot showed a neutron signal clearly separated from the photon flash.

sample nToF spectrum is shown in Fig. 6.4.

The neutron flux was also measured with BD-PND bubble detectors from Bubble Technology Industries. The bubble detectors contained droplets of super heated liquid which were suspended in an inert gel. Incident neutrons could deposit energy which served as a nucleation trigger causing the liquid to vaporize and create a bubble. The detectors were sensitive to neutrons with energies between 200 keV and 15 MeV with an approximately flat response. Their small size allowed them to be placed around the target chamber and enabled directionality measurements of the neutrons.

The ion diagnostic was a TP ion spectrometer [99] in the rear target normal direction, as discussed in Section 3.4.2. A micro-channel plate was used as the primary detector, but CR−39 was also used to differentiate between ion species with the same charge to mass ratio by observing different pit sizes from the different ion species.

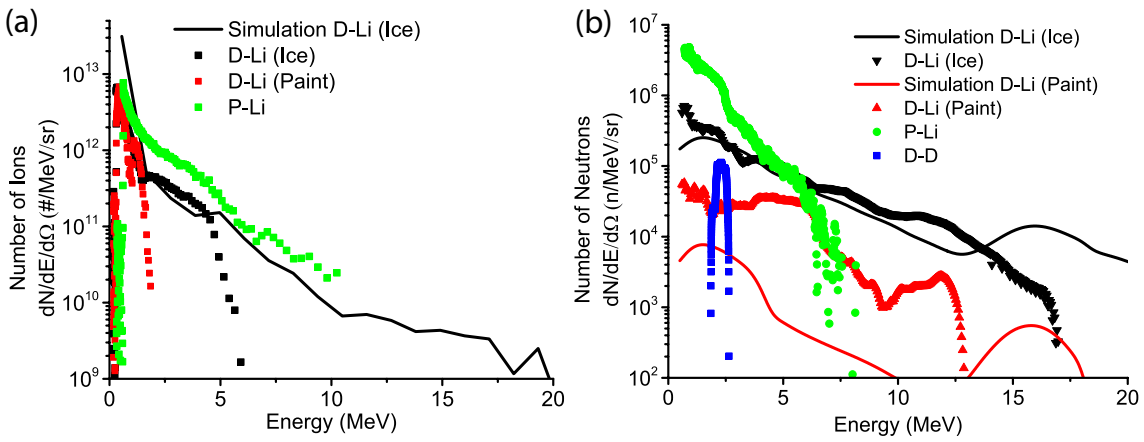

Figure 6.5: Simulated and experimental ion (a) and neutron (b) spectra along the target normal direction. (a) The P-Li spectrum from 100 nm Parylene shows the highest energies and total flux. The D-Li (Ice) spectrum shows higher flux and energy than D-Li (Paint). The simulated D-Li (Ice) spectrum was calculated with exponential scale length $L_s = 100$nm and scaled to match the experimental flux. (b) Experimental spectra from the four reactions. Monte Carlo simulated neutron spectra are shown for comparison.

6.3 Ion Optimization

The ion spectrum from each reaction was measured before the LiF catcher was placed in the ion beam. The spectra are shown in Fig. 6.5 (a). The deuteron spectrum for the bulk D-D reaction could not be measured because the deuterons did not penetrate through the target and therefore could not be detected. The P-Li Parylene target showed an exponentially decaying proton spectrum, consistent with TNSA acceleration, that exhibited a maximum detectable proton energy of 11 MeV on the TP. The deuteron spectra for the paint and ice covered D-Li targets were measured along the ion $q/m = 1/2$ parabola, however the charge to mass ratio of deuterons is the same as C^{6+} and O^{8+}, which means the three traces can overlap. The presence of accelerated deuterons from the D-Li (Paint) targets was confirmed with CR-39.

For the D-Li (Ice) targets, the effect of the deposited heavy ice layer is shown in Fig. 6.6 for two sequential shots. The clean spectra, without any heavy ice layer,

demonstrates the acceleration of protons and a small amount of C^{6+}, with the raw TP trace shown in Fig. 6.6 (c). The deuteron traces from the D-Li (Ice) target demonstrated nearly total suppression of the proton acceleration, with deuterons accounting for 95% of the measured light ion flux, as shown in Fig. 6.6 (d), consistent with previous results [155][156]. The deuteron signal in the D-Li (Ice) target was not contaminated with the small C^{6+} signal as Fig 6.6 (d) demonstrates a complete suppression of carbon ions and no oxygen charge states above O^{6+}. This result indicates the D_2O ice forms a continuous layer over the normal hydrogenous contaminants since TNSA preferentially accelerates the outermost ions [154].

The purity of the accelerated deuterons from D-Li (Ice) targets, quantified as a ratio of the number or total energy of protons to deuterons above 0.5 MeV, was measured for a variety of timing delays between the pulse of heavy water and the arrival of the laser pulse at the target. As seen in Fig. 6.7, the deuteron beam purity increased over 100 fold when the timing delay was decreased from 10 seconds to 0.35 seconds and the number ratio peaked at 250($\pm$100). The error bars represent the range of values measured from multiple shots with the same experimental conditions. Shorter time delays could not be tested due to laser safety concerns related to reflected light back into the amplifiers from the heavy water vapor in the target chamber. The D_2O sample was 99.8% pure yielding, in the absence of additional H_2O contaminants, a maximum ratio purity ratio of 500 which was only a factor of two higher than observed in the experiment. The energy ratio showed the same trend, but peaked at 620($\pm$250) which demonstrated that the proton impurities in the heavy water were not preferentially accelerated by the TNSA field. The re-appearance of protons in the ion signal for later times is believed to be due to sublimation of the heavy water ice layer as well as re-deposition of hydrogenous contaminants on the surface of target. Experiments conducted at target holder temperatures of 140^o($\pm$15) K appeared to exhibit parasitic target acceleration effects from the accumulation of ice on the target,

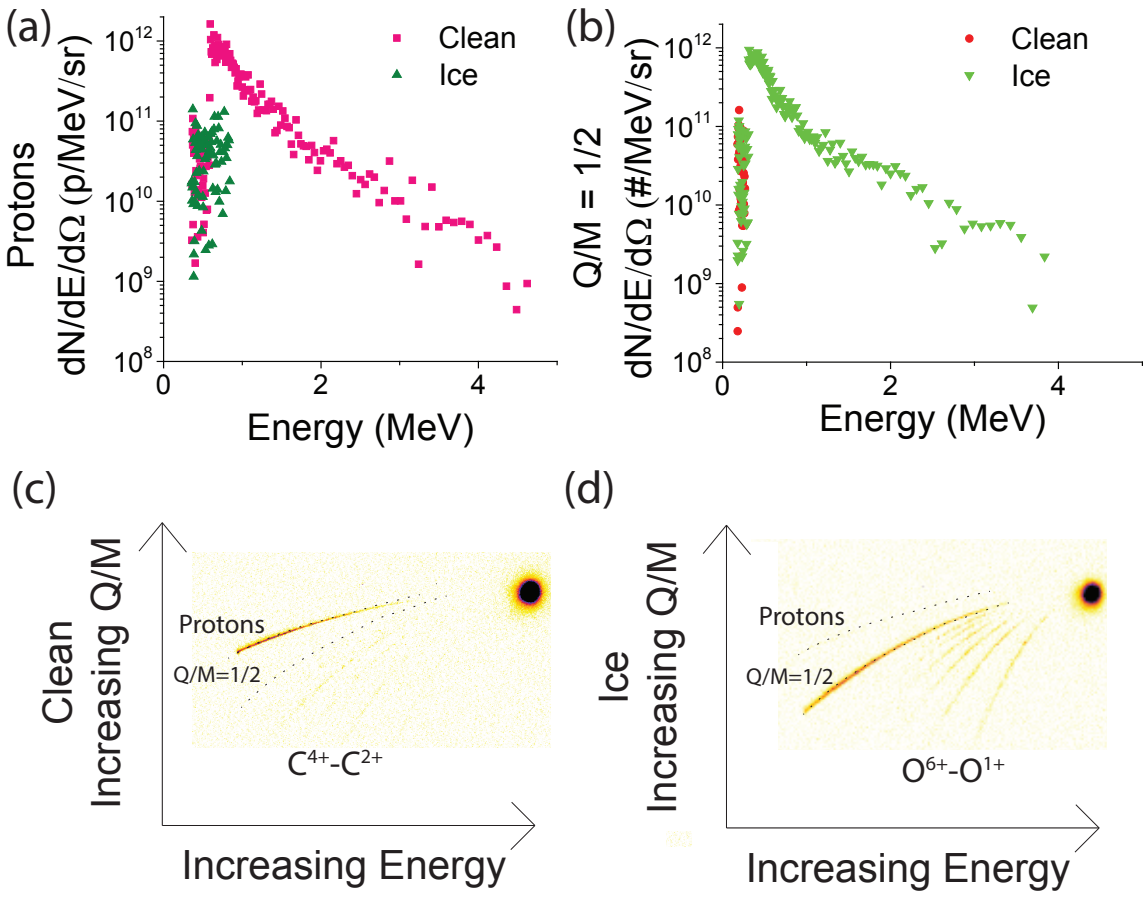

Figure 6.6: Ion spectra for q/m = 1 (a) and q/m = 1/2 (b) parabolas from sequential laser shots on 1.8 μm Al foil. (a) Proton spectra for the clean and ice covered target case showing suppression of the protons by the ice layer. (b) q/m = 1/2 trace showing a small amount of C^{6+} contaminant for the clean case. The ice case shows no O^{7+} which precludes the presence of O^{8+} contamination in the trace, as well as no carbon traces, yielding a pure deuteron signal. The corresponding Thomson parabola traces for the clean (c) and ice (d) case demonstrate the dramatic increase in deuteron signal. Additionally, the heavy ion traces change from carbon (c) to oxygen (d). The dashed lines indicate the location of the proton and q/m = 1/2 parabolas.

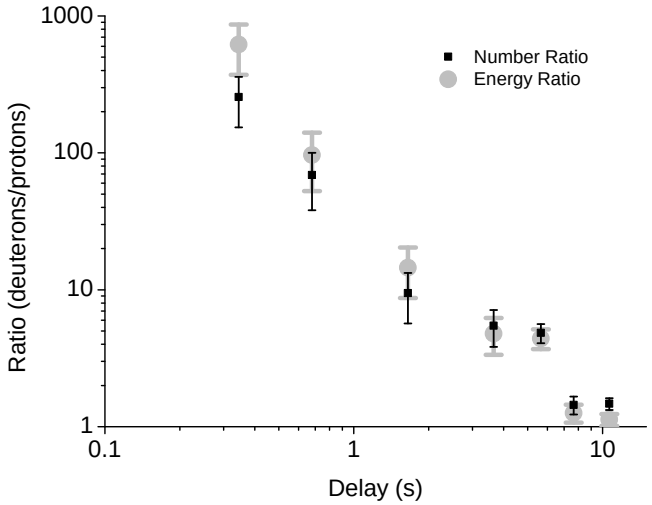

Figure 6.7: The purity, measured as the ratio of the number (black) or total energy (grey) of deuterons to protons observed on the TP with energies above 0.5 MeV, for different timing delays between the heavy water spray and laser pulse arrival on D-Li (Ice) targets. The number ratio approaches the limit of 500, due to impurities in the D_2O, for short timing delays. At longer timing delays the deuterated ice layer sublimates and is contaminated with hydrogenous materials.

however this issue was avoided by operating at target holder temperatures closer to 170^o K. Deuteron acceleration was observed for temperatures as high as 190^o K.

6.4 Neutron Measurements

The experimental single shot neutron spectra are shown in Fig. 6.5 (b). The highest observed total neutron flux for each reaction is listed in Table 6.2. The uncertainty in the neutron flux measurements was a result of uncertainty in the total flux of the calibration source, allowing an accurate comparison between reactions. The D-D spectra from bulk CD was sharply peaked around the characteristic 2.45 MeV peak energy indicating the deuteron energies were very low (<<2 MeV) and produced no upshifted neutrons. This was consistent with the expected deuteron energies from the bulk target. The P-Li spectra demonstrated the same exponential shape that was observed in the proton spectra, albeit with energy downshifted by a

Reaction	Max Flux (n/sr)	Max E_n
(D,D)	1.2 ($\pm$0.6)$\times 10^5$	2.6 ± 0.05 MeV
(P,Li)	1.0 ($\pm$0.5)$\times 10^7$	7.2 ± 0.8 MeV
(D,Li)	4.6 ($\pm$2.2)$\times 10^5$	12.6 ± 0.3 MeV
(D,Li)	3 ($\pm$1.4)$\times 10^6$	16.8 ± 0.3 MeV

Table 6.2: Nuclear reactions and target configurations investigated on HERCULES. The highest measured flux was observed for the P-Li reaction, and the highest energy was observed for the D-Li (ice) reaction.

few MeV, corresponding to the negative Q value of the reaction. The P-Li neutron spectra also had the highest flux of $1(\pm 0.5) \times 10^7$ n/sr, which was consistent with the high P-Li proton flux. The directionality of the neutrons, as measured by the bubble detectors, showed that the P-Li reaction neutron flux in the forward direction was 6.2 ($\pm$3.7) times higher than the flux at 90^o. The D-Li spectra exhibited a complex shape and significant upshift from the deuteron spectra up to energies of 12.6($\pm$0.3) and 16.8($\pm$0.3) MeV for painted and ice targets, respectively. The conversion efficiency of laser energy to ion energy was 1%, using a measured FWHM beam divergence of 20^o, and the ions were converted into neutrons with an efficiency of 0.1% yielding a total conversion efficiency of laser energy to neutron energy of $1(\pm 0.5) \times 10^{-5}$. Numerical simulations were performed in order to better understand the shape of the D-Li spectra.

6.5 Simulations

The D-Li (Ice) target spectrum was simulated using a 2D relativistic PIC code to simulate the high-intensity laser-plasma interaction [157]·[158]. The laser parameters were selected to match the HERCULES laser conditions, as previously described. The 800 nm Al target was modeled as having a 5 nm CH contaminant layer on the rear surface which was overlaid by a D_2O layer with an exponential density profile of the form $\rho = A \times \exp(-z/L_s)$, where A was the solid target density and L_s was the scale

length. This profile was used to account for the heavy water sublimation, which has been shown to have an approximately exponential density profile [159]. Simulations with $0.02<L_s<1$ μm were performed in an attempt to match the experimentally measured deuteron spectra. The best match was observed for a scale length $L_s = 0.1$ μm, shown in Fig. 6.5 (a), which was adopted for further simulations. The D-Li (Paint) target spectrum used the experimentally measured deuteron spectrum to calculate the neutron production.

The neutron production was simulated by modeling the passage of the deuteron spectra through a semi-infinite LiF converter. A 3D Monte Carlo code [65], mentioned in Section 3.5.1, was used to calculate the angularly resolved neutron spectra based on the double-differential cross section $d^2\sigma/d\Omega dE_n$[108]. The simulation results are shown in Fig. 6.5 (b) along with the experimental data. The experimental D-Li (Ice) target spectrum showed reasonable agreement with the PIC simulation results with $L_s = 100$ nm. The spectra from D-Li (Paint) target exhibited a dual peak shape that resulted from two neutron production mechanisms.

Neutron reactions are broadly classified into compound or direct reactions[160]. In compound reactions the incident particle and target nucleus form an intermediary compound nucleus which then decays into the reaction products. The interaction occurs over time scales of as short as 10^{-20} seconds[161] and is elastic in the absence of excited nuclear states. Alternatively, direct nuclear reactions occur when only one or a few of the incident particle or nucleus nucleons are involved in the interaction. One type of direct nuclear reaction is the deuteron stripping reaction [162]. In this reaction the loosely bound deuteron passes by a target nucleus at a distance where one of the deuteron nucleons interacts with the nucleus through the strong force, while the other nucleon continues without the transfer of significant energy or momentum[163]. The time scale for this interaction is 10^{-22} seconds, which is considerably faster than that of the compound reaction. Two important characteristics of this reaction are

the anisotropic distribution of the stripped nucleon, which is tightly confined to the forward direction, and the nucleon energy, which is centered around half the original deuteron energy. The energy spread, $E_d/2 \pm \Delta E$, and angular spread of the neutron beam are

$$\Delta E = 1.5 \left(\epsilon_d E_d\right)^{1/2} \tag{6.1}$$

$$\Delta\theta = 1.6 \left(\frac{\epsilon_d}{E_d}\right)^{1/2} \tag{6.2}$$

where $\epsilon_d = 2.18$ MeV is the deuteron binding energy, and E_d is the deuteron energy. The stripping reaction is not likely for deuteron energies below the binding energy as the nucleons rotate faster than the interaction time scale, preventing a direct reaction from occurring. In both types of reactions the initial and final products are the same, however, in the stripping reaction, energy and momentum conservation require that the target nucleus contains the additional energy which would be transferred to the neutron in a compound reaction. This energy can be stored in the angular momentum and excited nuclear levels of the target nucleus.

In the experimental neutron spectrum, the low energy peak was a result of the stripping reaction [163], producing neutrons with energies $\mathrm{E}_d/2$, while the high energy peak was the result of the high Q value producing neutrons with energies $\approx \mathrm{E}_d + Q$. The spectrum from the D-Li (Ice) target demonstrated that as the deuteron energy increased the stripping reaction dominated and the spectral shape became exponential. The slope predicted by simulations was close to that observed in the experiment. However, the location of the high-energy peak in the simulations was about 5 MeV higher than the one measured by the nToF detectors.

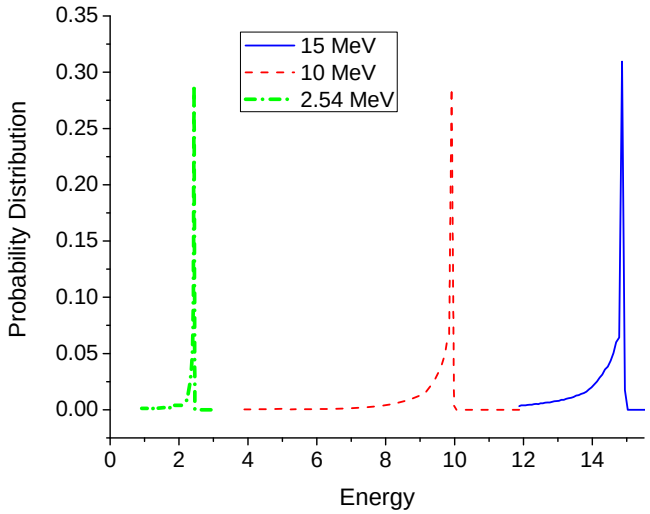

Figure 6.8: MCNPX simulated nToF energy spectrum for mono-energetic neutron beams of 2.54, 10, and 15 MeV for the 9.45 m detector. The downshift is a result of the LiF converter as well as the chamber and shielding materials between the detector and neutron source.

In order to investigate this discrepancy, the effect of neutron scattering, as a result of the vacuum chamber wall, Pb shielding, etc., on the nToF measurements was evaluated using MCNPX[119]. The downshift in the apparent nToF energy, due to the increased path length and lower energy of the scattered neutrons, resulted in 33% of the highest energy neutrons being downshifted less than 0.15 MeV, and >50% less than 0.5 MeV below their original energy. The simulated nToF spectra are shown in Fig. 6.8. The observed experimental neutron peak was close to what would be expected from very low energy deuterons, as measured in the low energy exponential peak of the deuteron spectra, producing neutrons that receive 13.4 MeV of the energy from the nuclear reaction, as necessary for momentum conservation, and were then downscattered by about twice the amount predicted by MCNPX. This discrepancy could be explained by inaccuracies in the MCNPX Pb elastic neutron cross-sections at higher energies and the double-differential D-Li neutron production cross section in the Monte Carlo code, or by lower experimental deuteron energies than predicted by the idealized uniform exponential scale length.

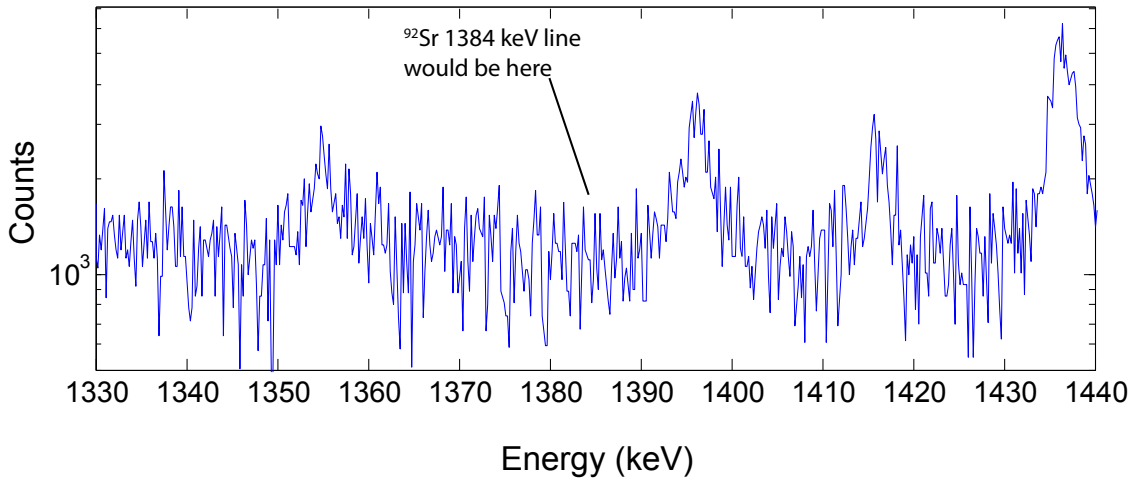

Figure 6.9: ^{238}U gamma spectrum measured with the HPGe detector. The fission fragment ^{94}Sr is typically used as an indicator of the fission of ^{238}U. The location of the ^{94}Sr line at 1384 keV is indicated with an arrow, and was not observed in this spectrum.

6.6 Activation

A 200 g ^{238}U sample was placed 1 cm behind the LiF converter to irradiate the sample with D-Li (Ice) neutrons. A maximum of 10 shots were allowed by the University of Michigan Occupational Safety and Environmental Health service due to concerns about activating the Uranium. The activated ^{238}U sample was measured with the HPGe detector for a 12 hour period with spectra recorded every 10 minutes. The spectra were evaluated for the presence of decay peaks from ^{238}U fission fragments at time periods of $1-2$ half-lives, where the fission fragment decay peak would have the strongest signal-to-background. No activation peaks were observed, as shown in Fig. 6.9.

6.7 Conclusions

In conclusion, the production of neutrons through charged particle acceleration and nuclear reactions at an intensity of 2×10^{21} W/cm^2 has been demonstrated on

a femtosecond laser system with a 0.1 Hz repetition rate. The P-Li reaction demonstrated the highest flux, $1(\pm 0.5)\times 10^7$ and directionality, $6.2(\pm 3.7)$ times higher in the forward direction than at 90^o, due to the high initial proton energy achieved with the Parylene 100 nm target. The D-Li (Ice) target produced 3 $(\pm 1.4)\times 10^6$ neutrons/sr with energies up $16.8(\pm 0.3)$ MeV. The measured neutron flux from the HERCULES laser system was comparable to the flux produced by commercially available D-D generators but in a directional beam with a picosecond bunch duration and higher energies. These results could also be scaled to higher repetition rates, as high intensity lasers that could produce 100 times the time averaged neutron flux of HERCULES are now becoming commercially available.

The D-Li (Ice) target improved both the energy and total number of deuterons and neutrons, as compared to the D-Li painted target. This was attributed to the uniform deposition of deuteron contaminants on the target surface. Deuterons were shown to comprise >99% of the accelerated light ions for short timing delays between the deposition of the ice layer and the arrival of the laser pulse. For longer time delays the heavy ice layer sublimated and became contaminated with hydrogenous material, which led to a decrease in the efficiency of the deuteron acceleration. Neutron spectra were observed that were consistent with theoretical and simulated predictions, but with a lower maximum neutron energy, attributed to discrepancies in the differential cross section and overestimates of deuteron energies due to idealized target conditions.

An attempt to activate ^{238}U was unsuccessful. The detection threshold for the experiment was about 100 counts in a single fission fragment decay peak on the HPGe detector. This would require about 1×10^4 fissions in the sample, as the ^{238}U fission fragment spectrum spans multiple isomers with atomic mass numbers from 90 to 150. While this was potentially possible with 10 shots of 10^6 neutrons per shot, experimental considerations, such as laser fluctuations, and the small uranium sample size, led to no measureable activation of the sample. An increase in the number of

allowed shots, neutron flux, or sample size may have led to measurable activation.

CHAPTER VII

Conclusions and Outlook

7.1 Summary and Discussion

The preceeding chapters have described a systematic investigation of the generation of radiation with laser plasma accelerators, with a particular emphasis on the potential for applications in active interogation. The research was performed on the CPA HERCULES and λ^3 lasers at the University of Michigan CUOS. These lasers represent a substantial step towards the high repetition rates needed for pratical applications.

The high repetition rate of λ^3 also allowed a novel high resolution measurement of the generated bremsstrahlung radiation. This diagnostic was used to better understand the electron behavior, particularly inside of the target. A high energy electron beam was observed in the specular direction, which produced high energy bremsstrahlung photons in the same direction. The beam was observed to scale with energy at a higher rate than Beg scaling. This highlights a significant difference between picosecond and femtosecond scale laser plasma interactions, both in terms of directionality and energy scaling.

The acceleration of protons, using structured targets, was then reported. It was observed that reducing the target surface area constrained the TNSA electron sheath to a smaller area, increasing its strength, and leading to high temperature proton

Table 7.1: A comparison of various laser neutron sources, highlighting the HERCULES results presented in this thesis. The other results are reproduced from Table 1.4

Publication	Flux (n/sr/shot)	Laser Energy (J)	Intensity (W/cm^2)	Reaction	Year
Lancaster *et al.*[55]	4×10^8	69	3×10^{19}	^{7}Li(p,n)^{7}Be	2004
Higginson *et al.*[56]	8×10^8	360	2×10^{19}	^{7}Li(d,n)^{8}Be	2011
Higginson *et al.*[57]	1.4×10^8	140	1×10^{20}	^{7}Li(p,n)^{7}Be	2010
Willingale *et al.*[58]	5×10^4	6	$(1-3) \times 10^{19}$	^{2}d(d,n)^{3}He	2011
Norreys *et al.*[59]	7×10^7	20	1×10^{19}	^{2}d(d,n)^{3}He	1998
Roth *et al.*[60]	1×10^{10}	80	$(1-10) \times 10^{20}$	^{9}Be(d,n)^{10}B	2013
Pretzler *et al.*[61]	3×10^8	0.2	1×10^{18}	^{2}d(d,n)^{3}He	1998
Fritzler *et al.*[62]	1×10^6	62	2×10^{19}	^{2}d(d,n)^{3}He	2002
Ditmire *et al.*[63]	5×10^9	30×10^3	n/a	^{2}d(d,n)^{3}He	1999
Taylor *et al.*[64]	1×10^{19}	2×10^6	n/a	^{3}t(d,n)^{4}He	n/a

beams. While this had been predicted for mass limited targets, structured targets are easier to manufacture and position, and showed the same behavior. A magnetic focusing effect was observed with wire targets, which led to a higher proton flux.

Laser plasma accelerator based neutron production was then reported, examining the use of protons and deuterons to generate neutrons though fusion reactions. The efficient acceleration of deuterons was shown using cryogencially cooled targets with a layer of deuterated ice. The HERCULES neutron flux, per joule, as found in Table 7.1, compare favorably with previous neutron results, especially when considering the higher repetition rate of the HERCULES laser. At a repetition rate of 0.1 Hz, the HERCULES results are also comparable to traditional D-D neutron generators but with higher energy neutrons in a directional beam.

7.2 Future Applications and Outlook

While attempts to demonstrate the activation of ^{238}U were unsuccessful, there are several avenues of research that can be investigated in the future. Increased electron energy from λ^3, which would be possible with increased laser intensity, would greatly

increase the probability of detecting (γ, f) in ^{238}U. The λ^3 laser energy has recently been increased from the 12 mJ used in the experiment described here, to 20 mJ. Further increases in the laser energy, and futher pulse compression [164], could lead to increased laser intensities and electron energies, while maintaining the 500 Hz repetition rate.

The opportunity also exists to systematically study the conversion of electrons in the specular beam into bremsstrahlung through the use of converter materials. Due to the geometery of the electron beam, bremsstrahlung was mainly generated in the chamber wall. It may be possible to more efficiently generate bremsstrahlung by placing high Z materials of varying thickness in the beam path. The potential to independantly optimize the electron acceleration and the bremsstrahlung conversion would be extremely useful in applications.

The main obstacle to activation of ^{238}U with neutrons was the limitations placed on the experiment. The limited number of shots, as well as the material limitations, decreased the probability of observing activation. Fissile material, which could be activated by the substantial number of low energy neutrons, would be highly desirible for proof-of-principle experiments. This, of course, was not possible. The use of ^{238}U could still have been possible under optimum conditions, especially with an increased number of shots. Alternatively, improvements to the laser plasma acceleration scheme, such as those observed with structured targets, could also improve activation probability.

Independent of the above discussion, significant hurdles remain before laser plasma based active interrogation could be implemented for homeland security. The use of high repetition rates lasers requires targets that can be rapidly "refreshed" between laser shots in order to maintain a clean interaction surface. In the experiments described in λ^3 this was accomplished by rotating a disk shaped target. Other efforts have investigated the use of tape drives [165]. Tape drives offer the advantages of thin

targets, more typical of laser plasma accelerators than thick disks, and arbitrarily long lengths, leading to an increased number of possible shots.

Improvements in laser technology will also lead to improvements in laser plasma accelerators. Commercial lasers similar to HERCULES are now available with 10 Hz repetition rates. New approaches to generating high intensities are also being investigated. The use of fiber lasers, which can support very high repetition rates due to the efficient removal of heat through the large surface area of fiber amplifiers, has been proposed as a path to high average power laser plasma accelerators [166]. This type of laser would require the combintation of multiple fiber lasers into a single energetic pulse, which is typically difficult due to phase matching requirements. However, some applications do not require coherent recombination of the pulses[167], which may simplify the path towards implementation of such a laser.

APPENDICES

APPENDIX A

Photon Pile-Up

In the single-hit regime photon pile-up is governed by Poisson statistics which predict the probability of the detector recording n events is

$$P(n) = \frac{\bar{x}^n e^{-\bar{x}}}{n!} \tag{A.1}$$

where $\bar{x}$ is the theoretical photon interaction probability. This probability, which is the first moment of the distribution, or $\bar{x} = \sum_{n=0}^{\infty} nP(n)$, was higher than the experimental detection probability x. The experimental detection probability, which was defined previously as the percentage of laser shots that resulted in a detection event on the HPGe detector, was described by $x = \sum_{n=1}^{\infty} P(n)$ due to photon pile-up. The percentage of detection events observed by the detector that were the result of piled-up photons was calculated by summing the probabilities of the detection of more than one photon, or $\sum_{n=2}^{\infty} P(n)$. This predicted 8% to 13% of the detected photons were due to pile-up for the detection event probabilities used during this experiment.

In order to evaluate the effect of the piled-up photons on the temperature measurement, a Monte Carlo code was written to simulate the observed photon spectrum. A

dual exponential spectrum was used to model a true bremsstrahlung spectrum, $f(E)$, of the form

$$f(E) = (1 - e^{-E/Fe}/A) \times e^{-E/E_b} \tag{A.2}$$

where E_b was the bremsstrahlung temperature, $Fe = 50$ was selected to match the e-folding of the steel transmission curve above 50 keV, and $A = e^{-1}$ was chosen to eliminate photons below 50 keV, such that the low energy (< 100 keV) photon attenuation was accurately modelled. Using this distribution, a spectrum was numerically compiled by modelling the probability of the photon producing a "hit" on the detector using the probabilities P(n). Single photons hits, P(1), were simply recorded in the correct detector channel. Pile-up hits, P(2,3), were combined with one or two additional photons, repetitively, which were separately generated with the same bremsstrahlung spectrum, and then recorded in the channel corresponding to the sum of their energies. This effect alone caused the effective temperature to be overestimated by $\leq 15\%$.

However, the HPGe detector has a detection efficiency that strongly depends on the absorption process, which becomes dominated by the Compton effect over 200 keV [9], and drops in efficiency. In the Compton range, the HPGe detector was measured to have an intrinsic collection efficiency of $0.05 \times E(MeV)^{-0.9}$. In order to recover the true photon spectrum, the intrinsic efficiency of the detector was used to correct the signal. Specifically, the measured spectra were divided by the intrinsic efficiency of each channel, which increased the number of counts in the high energy channels by up to 8 times more than the 100 keV channel. This efficiency correction, when combined with the pile-up effect, amplifies the effect of the piled-up photons, as they are collected by the detector with high efficiency, and then recorded in high energy

channels which are corrected for low efficiency.

In order to correctly model this process, each detected photon was multiplied by the detection efficiency. Specifically, each detection event incremented the corresponding channel by

$$C(E_{\gamma_1} + ... + E_{\gamma_n}) = \frac{\sum_{z=1}^{z=n} D(E_{\gamma_z})}{n} \tag{A.3}$$

where E_{γ_z} is the energy of the photon γ_z, $C(E)$ is the channel corresponding to the summed energies of the detected photons and $D(E)$ is the intrinsic detection efficiency of the detector for a photon of energy E. After the spectrum was compiled in this fashion, the intrinsic efficiency was used to correct the signal, so that it could be compared to the experimental spectra. As a result of this numerical modelling it was observed that the experimentally measured temperature overestimated the true temperature by 35% to 70% over the true temperature range of 100 keV to 1 MeV. This relationship was found to follow $T = 1.1 \times T_{exp}^{0.92}$ where T was the true temperature and T_{exp} was the experimentally observed temperature. This relationship was used to correct the observed temperatures used for the scaling and directionality analysis.

BIBLIOGRAPHY

BIBLIOGRAPHY

[1] J. R. Oppenheimer. Memorandum for group leaders, subject: Trinity test. *Los Alamos Scientific Laboratory. Los Alamos, NM*, 1945.

[2] D. Albright and K. Kramer. Stockpiles still growing. *The Bulletin of the Atomic Scientists*, 14, 2004.

[3] D. Slaughter and D. Sprouse. Screening cargo containers to remove a terrorist threat. *Science and Technology Review*, pages 12–15, 2004.

[4] G. A. English, R. B. Firestone, D. L. Perry, J. P. Reijonen, K. Leung, G. F. Garabedian, G. L. Molnar, and Z. Revay. Prompt gamma activation analysis (pgaa) and short-lived neutron activation analysis (naa) applied to the characterization of legacy materials. *Journal of Radioanalytical and Nuclear Chemistry*, 277(1):25–29, 2008.

[5] D. Strellis and T. Gozani. Classifying threats with a 14-MeV neutron interrogation system. *Applied radiation and isotopes*, 63(5):799–803, 2005.

[6] G. Tsahi. Advances in accelerator based explosives detection systems. *Nuclear Instruments and Methods in Physics Research Section B: Beam Interactions with Materials and Atoms*, 79(14):601 – 604, 1993.

[7] J. Stevenson, T. Gozani, M. Elsalim, C. Condron, and C. Brown. Linac based photofission inspection system employing novel detection concepts. *Nuclear Instruments and Methods in Physics Research Section A: Accelerators, Spectrometers, Detectors and Associated Equipment*, 652(1):124–128, 2011.

[8] J. O'Malley, P. Adsley, S. Quillin, M. Owen, G. Weston, L. Cox, A. Thandi, S. Cullen, and I. D. Smith. Current status of awe programmes for remote detection of snm. In *Nuclear Science Symposium Conference Record, 2008. NSS '08. IEEE*, pages 695 –705, 2008.

[9] G.F. Knoll. Radiation detection and measurement. *Wiley*, pages 47–50,570, 2010.

[10] J. Myatt, J.A. Delettrez, A.V. Maximov, D.D. Meyerhofer, R.W. Short, C. Stoeckl, and M. Storm. Optimizing electron-positron pair production on kilojoule-class high-intensity lasers for the purpose of pair-plasma creation. *Physical Review E*, 79(6):066409, 2009.

[11] H.J. Bhabha. The creation of electron pairs by fast charged particles. *Proceedings of the Royal Society of London. Series A-Mathematical and Physical Sciences*, 152(877):559–586, 1935.

[12] D. Slaughter, M. Accatino, A. Bernstein, J. Candy, A. Dougan, J. Hall, A. Loshak, D. Manatt, A. Meyer, B. Pohl, S. Prussin, R. Walling, and D. Weirup. Detection of special nuclear material in cargo containers using neutron interrogation. *Internal Report UCRL*, 155315, 2003.

[13] C.L. Hollas, D.A. Close, and C.E. Moss. Analysis of fissionable material using delayed gamma rays from photofission. *Nuclear Instruments and Methods in Physics Research Section B: Beam Interactions with Materials and Atoms*, 24:503–505, 1987.

[14] K. A. Jordan and T. Gozani. Pulsed neutron differential die away analysis for detection of nuclear materials. *Nuclear Instruments and Methods in Physics Research Section B: Beam Interactions with Materials and Atoms*, 261(1):365–368, 2007.

[15] D.K. Wehe, H. Yang, and M.H. Jones. Observation of ^{238}U photofission products. *Nuclear Science, IEEE Transactions on*, 53(3):1430–1434, 2006.

[16] P.B. Moon. Resonant nuclear scattering of gamma-rays: Theory and preliminary experiments. *Proceedings of the Physical Society. Section A*, 64(1):76–82, 1951.

[17] U. Kneissl, H.H. Pitz, and A. Zilges. Investigation of nuclear structure by resonance fluorescence scattering. *Progress in Particle and Nuclear Physics*, 37:349–433, 1996.

[18] J. Pruet, D.P. McNabb, C.A. Hagmann, F.V. Hartemann, and C.P.J. Barty. Detecting clandestine material with nuclear resonance fluorescence. *Journal of Applied Physics*, 99(12):123102–123102, 2006.

[19] W. Bertozzi and R.J. Ledoux. Nuclear resonance fluorescence imaging in non-intrusive cargo inspection. *Nuclear Instruments and Methods in Physics Research Section B: Beam Interactions with Materials and Atoms*, 241(1):820–825, 2005.

[20] H. Yang and D.K. Wehe. Detection of concealed special nuclear material using nuclear resonance fluorescence technique. In *Nuclear Science Symposium Conference Record (NSS/MIC), 2009 IEEE*, pages 898–903. IEEE, 2009.

[21] H.W. Koch and J.W. Motz. Bremsstrahlung cross-section formulas and related data. *Reviews of Modern Physics*, 31(4):920–955, 1959.

[22] R.O. Haxby, W.E. Shoupp, W.E. Stephens, and W.H. Wells. Photo-fission of uranium and thorium. *Physical Review*, 59:57–62, 1941.

[23] M. King, T. Shaw, J. Stevenson, M. Elsalim, C. Brown, C. Condron, and T. Gozani. Simulation methods for photoneutron-based active interrogation systems. *Nuclear Instruments and Methods in Physics Research Section A: Accelerators, Spectrometers, Detectors and Associated Equipment*, 652(1):129–132, 2011.

[24] J.L. Jones, W.Y. Yoon, D.R. Norman, K.J. Haskell, J.M. Zabriskie, S.M. Watson, and J.W. Sterbentz. Photonuclear-based, nuclear material detection system for cargo containers. *Nuclear Instruments and Methods in Physics Research Section B: Beam Interactions with Materials and Atoms*, 241(1):770–776, 2005.

[25] J. Reijonen. Neutron generators developed at LBNL for homeland security and imaging applications. *Nuclear Instruments and Methods in Physics Research Section B: Beam Interactions with Materials and Atoms*, 261(1):272–276, 2007.

[26] J. Reijonen. Compact neutron generators for medical, home land security, and planetary exploration. In *Particle Accelerator Conference, 2005. PAC 2005. Proceedings of the IEEE*, pages 49–53. IEEE, 2005.

[27] F. Albert, F.V. Hartemann, S.G. Anderson, R.R. Cross, D.J. Gibson, J. Hall, R.A. Marsh, M. Messerly, S.S. Wu, C.W. Siders, and C.P.J. Barty. Precision linac and laser technologies for nuclear photonics gamma-ray sources. *Physics of Plasmas*, 19(5), 2012.

[28] B.J. Micklich, D.L. Smith, T.N. Massey, C.L. Fink, and D Ingram. Measurement of thick-target high-energy γ-ray yields from the ^{19} F(p, $\alpha\gamma$) ^{16}O reaction. *Nuclear Instruments and Methods in Physics Research Section A: Accelerators, Spectrometers, Detectors and Associated Equipment*, 505(1):1–4, 2003.

[29] Thomas J. T. Kwan, Richard E. Morgado, Tai-Sen F. Wang, B. Vodolaga, V. Terekhin, L. M. Onischenko, S. B. Vorozhtsov, E. V. Samsonov, A. S. Vorozhtsov, Yu. G. Alenitsky, E. E. Perpelkin, A. A. Glazov, D. L. Novikov, V. Parkhomchuk, V. Reva, V. Vostrikov, V. A. Mashinin, S. N. Fedotov, and S. A. Minayev. The development of enabling technologies for producing active interrogation beams. *Review of Scientific Instruments*, 81(10):103304 –103304–13, oct 2010.

[30] D. Dietrich, C. Hagmann, P. Kerr, L. Nakae, M. Rowland, N. Snyderman, W. Stoeffl, and R. Hamm. A kinematically beamed, low energy pulsed neutron source for active interrogation. *Nuclear Instruments and Methods in Physics Research Section B: Beam Interactions with Materials and Atoms*, 241(1):826–830, 2005.

[31] P. Kerr, M. Rowland, D. Dietrich, W. Stoeffl, B. Wheeler, L. Nakae, D. Howard, C. Hagmann, J. Newby, and R. Porter. Active detection of small quantities of shielded highly-enriched uranium using low-dose 60-keV neutron interrogation. *Nuclear Instruments and Methods in Physics Research Section B: Beam Interactions with Materials and Atoms*, 261(1):347–350, 2007.

[32] D. Strickland and G. Mourou. Compression of amplified chirped optical pulses. *Optics Communications*, 55(6):447–449, 1985.

[33] T. Tajima and J.M. Dawson. Laser electron accelerator. *Physical Review Letters*, 43(4):267–270, 1979.

[34] C. McGuffey, T. Matsuoka, S. Kneip, W. Schumaker, F. Dollar, C. Zulick, V. Chvykov, G. Kalintchenko, V. Yanovsky, A. Maksimchuk, A. G. R. Thomas, K. Krushelnick, and Z. Najmudin. Experimental laser wakefield acceleration scalings exceeding 100TW. *Physics of Plasmas*, 19(6), 2012.

[35] M. Vargas, W. Schumaker, Z.-H. He, Z. Zhao, K. Behm, V. Chvykov, B. Hou, K. Krushelnick, A. Maksimchuk, V. Yanovsky, and A. G. R. Thomas. Improvements to laser wakefield accelerated electron beam stability, divergence, and energy spread using three-dimensional printed two-stage gas cell targets. *Applied Physics Letters*, 104(17):–, 2014.

[36] S.P.D. Mangles, C.D. Murphy, Z. Najmudin, A.G.R. Thomas, J.L. Collier, A.E. Dangor, E.J. Divall, P.S. Foster, J.G. Gallacher, C.J. Hooker, D.A. Jaroszynksi, A.J. Langley, W.B. Mori, P.A. Norreys, F.S. Tsung, R. Viskup, B.R. Walton, and K. Krushelnick. Monoenergetic beams of relativistic electrons from intense laser–plasma interactions. *Nature*, 431(7008):535–538, 2004.

[37] C.G.R. Geddes, C. Toth, J. Van Tilborg, E. Esarey, C.B. Schroeder, D. Bruhwiler, C. Nieter, J. Cary, and W.P. Leemans. High-quality electron beams from a laser wakefield accelerator using plasma-channel guiding. *Nature*, 431(7008):538–541, 2004.

[38] J. Faure, Y. Glinec, A. Pukhov, S. Kiselev, S. Gordienko, E. Lefebvre, J.P. Rousseau, F. Burgy, and V. Malka. A laser–plasma accelerator producing monoenergetic electron beams. *Nature*, 431(7008):541–544, 2004.

[39] S. Banerjee, S.Y. Kalmykov, N.D. Powers, G. Golovin, V. Ramanathan, N.J. Cunningham, K.J. Brown, S. Chen, I. Ghebregziabher, B.A. Shadwick, D. P. Umstadter, B. M. Cowan, D. L. Bruhwiler, A. Beck, and E. Lefebvre. Stable, tunable, quasimonoenergetic electron beams produced in a laser wakefield near the threshold for self-injection. *Physical Review Special Topics-Accelerators and Beams*, 16(3):031302, 2013.

[40] E. Miura, S.I. Masuda, T. Ooyama, and S. Ishii. Quasi-monoenergetic electron beam generation by laser wakefield acceleration for all-optical ultrashort x-ray sources. *Journal of the Korean Physical Society*, 56(11):235–240, 2010.

[41] K.T. Phuoc, S. Corde, C. Thaury, V. Malka, A. Tafzi, JP Goddet, RC Shah, S. Sebban, and A. Rousse. All-optical Compton gamma-ray source. *Nature Photonics*, 6(5):308–311, 2012.

[42] H. Ohgaki, T. Noguchi, S. Sugiyama, T. Yamazaki, T. Mikado, M. Chiwaki, K. Yamada, R. Suzuki, and N. Sei. Linearly polarized photons from Compton backscattering of laser light for nuclear resonance fluorescence experiments. *Nuclear Instruments and Methods in Physics Research Section A: Accelerators, Spectrometers, Detectors and Associated Equipment*, 353(1):384–388, 1994.

[43] W.P. Leemans, D. Rodgers, P.E. Catravas, C.G.R. Geddes, G. Fubiani, E. Esarey, B.A. Shadwick, R. Donahue, and A. Smith. Gamma-neutron activation experiments using laser wakefield accelerators. *Physics of Plasmas*, 8(5 II):2510–2516, 2001.

[44] S.A. Reed, V. Chvykov, G. Kalintchenko, T. Matsuoka, V. Yanovsky, C.R. Vane, J.R. Beene, D. Stracener, D.R. Schultz, and A. Maksimchuk. Efficient initiation of photonuclear reactions using quasimonoenergetic electron beams from laser wakefield acceleration. *Journal of Applied Physics*, 102(7):073103–073103, 2007.

[45] K. W. D. Ledingham, I. Spencer, T. McCanny, R. P. Singhal, M. I. K. Santala, E. Clark, I. Watts, F. N. Beg, M. Zepf, K. Krushelnick, M. Tatarakis, A. E. Dangor, P. A. Norreys, R. Allott, D. Neely, R. J. Clark, A. C. Machacek, J. S. Wark, A. J. Cresswell, D. C. W. Sanderson, and J. Magill. Photonuclear physics when a multiterawatt laser pulse interacts with solid targets. *Physical Review Letters*, 84(5):899–902, 2000.

[46] T. E. Cowan, A. W. Hunt, T. W. Phillips, S. C. Wilks, M. D. Perry, C. Brown, W. Fountain, S. Hatchett, J. Johnson, M. H. Key, T. Parnell, D. M. Pennington, R. A. Snavely, and Y. Takahashi. Photonuclear fission from high energy electrons from ultraintense laser-solid interactions. *Physical Review Letters*, 84(5):903–906, 2000.

[47] S. Kneip, C. McGuffey, J.L. Martins, S.F. Martins, C. Bellei, V. Chvykov, F. Dollar, R. Fonseca, C. Huntington, G. Kalintchenko, A. Maksimchuk, S. P. D. Mangles, T. Matsuoka, S. R. Nagel, C. A. J. Palmer, J. Schreiber, K. Ta Phuoc, A. G. R. Thomas, V. Yanovsky, L. O. Silva, K. Krushelnick, and Z. Najmudin. Bright spatially coherent synchrotron x-rays from a table-top source. *Nature Physics*, 6(12):980–983, 2010.

[48] W.P. Leemans, B. Nagler, A.J. Gonsalves, C. Toth, K. Nakamura, C.G.R. Geddes, E. Esarey, C.B. Schroeder, and S.M. Hooker. GeV electron beams from a centimetre-scale accelerator. *Nature Physics*, 2(10):696–699, 2006.

[49] X. Wang, R. Zgadzaj, N. Fazel, Z. Li, S.A. Yi, X. Zhang, W. Henderson, Y.Y. Chang, R. Korzekwa, H.E. Tsai, C.H. Pai, H. Quevedo, G. Dyer, E. Gaul, M. Martinez, A. C. Bernstein, T. Borger, M. Spinks, M. Donovan, and V. Khudik. Quasi-monoenergetic laser-plasma acceleration of electrons to 2 GeV. *Nature Communications*, 4, 2013.

[50] V. Malka, A. Lifschitz, J. Faure, and Y. Glinec. Staged concept of laser-plasma acceleration toward multi-GeV electron beams. *Physical Review Special Topics-Accelerators and Beams*, 9(9):091301, 2006.

[51] W. Leemans. Compact electron accelerators based on lasers and plasmas: Towards a 10 GeV machine. *2012 IEEE 13th International Vacuum Electronics Conference*, pages 11–12, 2012.

[52] S.C. Wilks, A.B. Langdon, T.E. Cowan, M. Roth, M. Singh, S. Hatchett, M.H. Key, D. Pennington, A. MacKinnon, and R.A. Snavely. Energetic proton generation in ultra-intense laser–solid interactions. *Physics of Plasmas*, 8:542, 2001.

[53] R. A. Snavely, M. H. Key, S. P. Hatchett, T. E. Cowan, M. Roth, T. W. Phillips, M. A. Stoyer, E. A. Henry, T. C. Sangster, M. S. Singh, S. C. Wilks, A. MacKinnon, A. Offenberger, D. M. Pennington, K. Yasuike, A. B. Langdon, B. F. Lasinski, J. Johnson, M. D. Perry, and E. M. Campbell. Intense high-energy proton beams from petawatt-laser irradiation of solids. *Physical Review Letters*, 85:2945–2948, Oct 2000.

[54] A. Maksimchuk, S. Gu, K. Flippo, D. Umstadter, and V.Y. Bychenkov. Forward ion acceleration in thin films driven by a high-intensity laser. *Physical Review Letters*, 84(18):4108, 2000.

[55] K. L. Lancaster, S. Karsch, H. Habara, F. N. Beg, E. L. Clark, R. Freeman, M. H. Key, J. A. King, R. Kodama, K. Krushelnick, K. W. D. Ledingham, P. McKenna, C. D. Murphy, P. A. Norreys, R. Stephens, C. Steckl, Y. Toyama, M. S. Wei, and M. Zepf. Characterization of li (p, n) be neutron yields from laser produced ion beams for fast neutron radiography. *Physics of Plasmas*, 11:3404, 2004.

[56] D. P. Higginson, J. M. McNaney, D. C. Swift, G. M. Petrov, J. Davis, J. A. Frenje, L. C. Jarrott, R. Kodama, K. L. Lancaster, A. J. Mackinnon, H. Nakamura, P. K. Patel, G. Tynan, and F. N. Beg. Production of neutrons up to 18 MeV in high-intensity, short-pulse laser matter interactions. *Physics of Plasmas*, 18:100703, 2011.

[57] D. P. Higginson, J. M. McNaney, D. C. Swift, T. Bartal, D. S. Hey, R. Kodama, S. Le Pape, A. Mackinnon, D. Mariscal, H. Nakamura, N. Nakanii, K. A. Tanaka, and F. N. Beg. Laser generated neutron source for neutron resonance spectroscopy. *Physics of Plasmas*, 17:100701, 2010.

[58] L. Willingale, G.M. Petrov, A. Maksimchuk, J. Davis, R.R. Freeman, A.S. Joglekar, T. Matsuoka, C.D. Murphy, V.M. Ovchinnikov, A.G.R. Thomas, L. Van Woerkom, and K. Krushelnick. Comparison of bulk and pitcher-catcher targets for laser-driven neutron production. *Physics of Plasmas*, 18:083106, 2011.

[59] P.A. Norreys, A.P. Fews, F.N. Beg, A.R. Bell, A.E. Dangor, P. Lee, M.B. Nelson, H. Schmidt, M. Tatarakis, and M.D. Cable. Neutron production from picosecond laser irradiation of deuterated targets at intensities of. *Plasma physics and controlled fusion*, 40(2):175–182, 1998.

[60] M. Roth, D. Jung, K. Falk, N. Guler, O. Deppert, M. Devlin, A. Favalli, J. Fernandez, D. Gautier, M. Geissel, R. Haight, C. E. Hamilton, B. M. Hegelich, R. P. Johnson, F. Merrill, G. Schaumann, K. Schoenberg, M. Schollmeier, T. Shimada, T. Taddeucci, J. L. Tybo, F. Wagner, S. A. Wender, C. H. Wilde, and G. A. Wurden. Bright laser-driven neutron source based on the relativistic transparency of solids. *Physical Review Letters*, 110(4):044802, 2013.

[61] G. Pretzler, A. Saemann, A. Pukhov, D. Rudolph, T. Schätz, U. Schramm, P. Thirolf, D. Habs, K. Eidmann, G. D. Tsakiris, J. Meyer-ter Vehn, and K. J. Witte. Neutron production by 200 mJ ultrashort laser pulses. *Physical Review E*, 58(1):1165, 1998.

[62] S. Fritzler, Z. Najmudin, V. Malka, K. Krushelnick, C. Marle, B. Walton, M.S. Wei, R.J. Clarke, and A.E. Dangor. Ion heating and thermonuclear neutron production from high-intensity subpicosecond laser pulses interacting with underdense plasmas. *Physical Review Letters*, 89(16):165004, 2002.

[63] T. Ditmire, J. Zweiback, V.P. Yanovsky, T.E. Cowan, G. Hays, and K.B. Wharton. Nuclear fusion from explosions of femtosecond laser-heated deuterium clusters. *Nature*, 398(6727):489–492, 1999.

[64] A. Taylor, M. Dunne, S. Bennington, S. Ansell, I. Gardner, P. Norreys, T. Broome, D. Findlay, and R. Nelmes. A route to the brightest possible neutron source? *Science*, 315(5815):1092–1095, 2007.

[65] J. Davis, G.M. Petrov, T. Petrova, L. Willingale, A. Maksimchuk, and K. Krushelnick. Neutron production from ^{7}li(d, xn) nuclear fusion reactions driven by high-intensity laser–target interactions. *Plasma Physics and Controlled Fusion*, 52(4):045015, 2010.

[66] J.L. Redding. Interstellar vehicle propelled by terrestrial laser beam. *Nature*, 213:588–589, 1967.

[67] A.P.L. Robinson, M. Zepf, S. Kar, R.G. Evans, and C. Bellei. Radiation pressure acceleration of thin foils with circularly polarized laser pulses. *New Journal of Physics*, 10(1):013021, 2008.

[68] F. Dollar, C. Zulick, A. G. R. Thomas, V. Chvykov, J. Davis, G. Kalinchenko, T. Matsuoka, C. McGuffey, G. M. Petrov, L. Willingale, V. Yanovsky, A. Maksimchuk, and K. Krushelnick. Finite spot effects on radiation pressure acceleration from intense high-contrast laser interactions with thin targets. *Physical Review Letters*, 108(17):175005, 2012.

[69] D. Haberberger, S. Tochitsky, F. Fiuza, C. Gong, R.A. Fonseca, L.O. Silva, W.B. Mori, and C. Joshi. Collisionless shocks in laser-produced plasma generate monoenergetic high-energy proton beams. *Nature Physics*, 8(1):95–99, 2012.

[70] Charlotte A. J. Palmer, N. P. Dover, I. Pogorelsky, M. Babzien, G. I. Dudnikova, M. Ispiriyan, M. N. Polyanskiy, J. Schreiber, P. Shkolnikov, V. Yakimenko, and Z. Najmudin. Monoenergetic proton beams accelerated by a radiation pressure driven shock. *Physical Review Letters*, 106(1):014801, 2011.

[71] A.G. Mordovanakis, J. Easter, N. Naumova, K. Popov, P.E. Masson-Laborde, B. Hou, I. Sokolov, G. Mourou, I.V. Glazyrin, W. Rozmus, V. Bychenkov, J. Nees, and K. Krushelnick. Quasimonoenergetic electron beams with relativistic energies and ultrashort duration from laser-solid interactions at 0.5 kHz. *Physical Review Letters*, 103(23):235001, 2009.

[72] B. Hou, J. Nees, J. Easter, J. Davis, G. Petrov, A.G.R. Thomas, and K. Krushelnick. MeV proton beams generated by 3 mJ ultrafast laser pulses at 0.5 kHz. *Applied Physics Letters*, 95(10):101503, 2009.

[73] V. Yanovsky, V. Chvykov, G. Kalinchenko, P. Rousseau, T. Planchon, T. Matsuoka, A. Maksimchuk, J. Nees, G. Cheriaux, G. Mourou, and K. Krushelnick. Ultra-high intensity-300-TW laser at 0.1 Hz repetition rate. *Optics Express*, 16(3):2109–2114, 2008.

[74] E. Treacy. Optical pulse compression with diffraction gratings. *Quantum Electronics, IEEE Journal of*, 5(9):454–458, 1969.

[75] O.E. Martinez. Design of high-power ultrashort pulse amplifiers by expansion and recompression. *Quantum Electronics, IEEE Journal of*, 23(8):1385–1387, 1987.

[76] P. Mora and T.M. Antonsen. Electron cavitation and acceleration in the wake of an ultraintense, self-focused laser pulse. *Physical Review E*, 53:R2068–R2071, 1996.

[77] W.L. Kruer. *The physics of laser plasma interactions*, volume 70. Addison-Wesley New York, 1988.

[78] F. Brunel. Not-so-resonant, resonant absorption. *Physical Revew Letters*, 59:52–55, Jul 1987.

[79] P. Gibbon. *Short pulse laser interactions with matter*. World Scientific Publishing Company, 2004.

[80] S.C. Wilks, W.L. Kruer, M. Tabak, and A.B. Langdon. Absorption of ultraintense laser pulses. *Physical Review Letters*, 69(9):1383, 1992.

[81] F.N. Beg, A.R. Bell, A.E. Dangor, C.N. Danson, A.P. Fews, M.E. Glinsky, B.A. Hammel, P. Lee, P.A. Norreys, and M.A. Tatarakis. A study of picosecond laser–solid interactions up to 10^{19} w cm- 2. *Physics of Plasmas (1994-present)*, 4(2):447–457, 1997.

[82] M.G. Haines, M.S. Wei, F.N. Beg, and R.B. Stephens. Hot-electron temperature and laser-light absorption in fast ignition. *Physical Review Letters*, 102(4):045008, 2009.

[83] A.G. Mordovanakis, P.E. Masson-Laborde, J. Easter, K. Popov, B. Hou, G. Mourou, W. Rozmus, M.G. Haines, J. Nees, and K. Krushelnick. Temperature scaling of hot electrons produced by a tightly focused relativistic-intensity laser at 0.5 kHz repetition rate. *Applied Physics Letters*, 96(7):071109, 2010.

[84] P. Mora. Plasma expansion into a vacuum. *Physical Review Letters*, 90:185002, May 2003.

[85] F. Dollar, P. Cummings, V. Chvykov, L. Willingale, M. Vargas, V. Yanovsky, C. Zulick, A. Maksimchuk, A. G. R. Thomas, and K. Krushelnick. Scaling high-order harmonic generation from laser-solid interactions to ultrahigh intensity. *Physical Review Letters*, 110:175002, Apr 2013.

[86] J.D. Jackson. Classical electrodynamics, 3rd edn. *ISBN: 0-471-30932-X*, 1999.

[87] D.J.S. Findlay. Analytic representation of bremsstrahlung spectra from thick radiators as a function of photon energy and angle. *Nuclear Instruments and Methods in Physics Research Section A: Accelerators, Spectrometers, Detectors and Associated Equipment*, 276(3):598–601, 1989.

[88] A. Jullien, O. Albert, F. Burgy, G. Hamoniaux, J.P. Rousseau, J.-P. Chambaret, F. Augé-Rochereau, G. Chériaux, J. Etchepare, N. Minkovski, and S.M. Saltiel. 10^{-10} temporal contrast for femtosecond ultraintense lasers by cross-polarized wave generation. *Optics Letters*, 30(8):920–922, 2005.

[89] V. Chvykov, P. Rousseau, S. Reed, G. Kalinchenko, and V. Yanovsky. Generation of 10^{11} contrast 50 TW laser pulses. *Optics letters*, 31(10):1456–1458, 2006.

[90] O. Albert, H. Wang, D. Liu, Z. Chang, and G. Mourou. Generation of relativistic intensity pulses at a kilohertz repetition rate. *Optics Letters*, 25(15):1125–1127, 2000.

[91] R.N. Gyuzalian, S.B. Sogomonian, and Z.G. Horvath. Background-free measurement of time behaviour of an individual picosecond laser pulse. *Optics Communications*, 29(2):239–242, 1979.

[92] F. Dollar, T. Matsuoka, G. M. Petrov, A. G. R. Thomas, S. S. Bulanov, V. Chvykov, J. Davis, G. Kalinchenko, C. McGuffey, L. Willingale, V. Yanovsky,

A. Maksimchuk, and K. Krushelnick. Control of energy spread and dark current in proton and ion beams generated in high-contrast laser solid interactions. *Physical Review Letters*, 107:065003, Aug 2011.

[93] C. Thaury, F. Quéré, J.P. Geindre, A. Levy, T. Ceccotti, P. Monot, M. Bougeard, F. Réau, P. d'Oliveira, P. Audebert, R. Marjoribanks, and P. Martin. Plasma mirrors for ultrahigh-intensity optics. *Nature Physics*, 3(6):424–429, 2007.

[94] G. Doumy, F. Quéré, O. Gobert, M. Perdrix, P. Martin, P. Audebert, J.C. Gauthier, J.P. Geindre, and T. Wittmann. Complete characterization of a plasma mirror for the production of high-contrast ultraintense laser pulses. *Physical Review E*, 69(2):026402, 2004.

[95] F. Dollar. *High intensity, high contrast laser solid interactions with short pulses*. PhD thesis, The University of Michigan, 2012.

[96] F. Dollar, C. Zulick, T. Matsuoka, C. McGuffey, S.S. Bulanov, V. Chvykov, J. Davis, G. Kalinchenko, G.M. Petrov, L. Willingale, V. Yanovsky, A. Maksimchuk, A.G.R. Thomas, and K. Krushelnick. High contrast ion acceleration at intensities exceeding 10^{21} Wcm^{-2}. *Physics of Plasmas*, 20(5):056703, 2013.

[97] R.M. Cassou and E.V. Benton. Properties and applications of CR-39 polymeric nuclear track detector. *Nuclear Track Detection*, 2(3):173–179, 1978.

[98] J.P. Biersack and L.G. Haggmark. A Monte Carlo computer program for the transport of energetic ions in amorphous targets. *Nuclear Instruments and Methods*, 174(1):257–269, 1980.

[99] W. Mróz, P. Norek, A. Prokopiuk, P. Parys, M. Pfeifer, L. Laska, M.P. Stockli, D. Fry, and K. Kasuya. Method of processing ion energy distributions using a thomson parabola ion spectrograph with a microchannelplate image converter camera. *Review of Scientific Instruments*, 71(3):1417–1420, 2000.

[100] L. Willingale. *Ion acceleration from high intensity laser plasma interactions: measurements and applications*. PhD thesis, Imperial College London, 2007.

[101] K. Harres, M. Schollmeier, E. Brambrink, P. Audebert, A. Blažević, K. Flippo, D.C. Gautier, M. Geißel, B.M. Hegelich, F. Nürnberg, J. Schreiber, H. Wahl, and M. Roth. Development and calibration of a thomson parabola with microchannel plate for the detection of laser-accelerated mev ions. *Review of Scientific Instruments*, 79(9):093306, 2008.

[102] W. Schumaker, N. Nakanii, C. McGuffey, C. Zulick, V. Chyvkov, F. Dollar, H. Habara, G. Kalintchenko, A. Maksimchuk, K.A. Tanaka, , A. G. R. Thomas, V. Yanovsky, and K. Krushelnick. Ultrafast electron radiography of magnetic fields in high-intensity laser-solid interactions. *Physical Review Letters*, 110(1):015003, 2013.

[103] M. Tatarakis, I. Watts, F.N. Beg, E.L. Clark, A.E. Dangor, A. Gopal, M.G. Haines, P.A. Norreys, U. Wagner, M.S. Wei, M. Zepf, and K. Krushelnick. Laser technology: Measuring huge magnetic fields. *Nature*, 415(6869):280–280, 2002.

[104] S. Agostinelli, J. Allison, K. Amako, J. Apostolakis, H. Araujo, P. Arce, M. Asai, D. Axen, S. Banerjee, G. Barrand, F. Behner, L. Bellagamba, J. Boudreau, L. Broglia, A. Brunengo, H. Burkhardt, S. Chauvie, J. Chuma, R. Chytracek, G. Cooperman, G. Cosmo, P. Degtyarenko, A. Dell'Acqua, G. Depaola, D. Dietrich, R. Enami, A. Feliciello, C. Ferguson, H. Fesefeldt, G. Folger, F. Foppiano, A. Forti, S. Garelli, S. Giani, R. Giannitrapani, D. Gibin, J.J. Gomez Cadenas, I. Gonzalez, G. Gracia Abril, G. Greeniaus, W. Greiner, V. Grichine, A. Grossheim, S. Guatelli, P. Gumplinger, R. Hamatsu, K. Hashimoto, H. Hasui, A. Heikkinen, A. Howard, V. Ivanchenko, A. Johnson, F.W. Jones, J. Kallenbach, N. Kanaya, M. Kawabata, Y. Kawabata, M. Kawaguti, S. Kelner, P. Kent, A. Kimura, T. Kodama, R. Kokoulin, M. Kossov, H. Kurashige, E. Lamanna, T. Lampen, V. Lara, V. Lefebure, F. Lei, M. Liendl, W. Lockman, F. Longo, S. Magni, M. Maire, E. Medernach, K. Minamimoto, P. Mora de Freitas, Y. Morita, K. Murakami, M. Nagamatu, R. Nartallo, P. Nieminen, T. Nishimura, K. Ohtsubo, M. Okamura, S. O'Neale, Y. Oohata, K. Paech, J. Perl, A. Pfeiffer, M.G. Pia, F. Ranjard, A. Rybin, S. Sadilov, E. di Salvo, G. Santin, T. Sasaki, N. Savvas, Y. Sawada, S. Scherer, S. Sei, V. Sirotenko, D. Smith, N. Starkov, H. Stoecker, J. Sulkimo, M. Takahata, S. Tanaka, E. Tcherniaev, E. Safai Tehrani, M. Tropeano, P. Truscott, H. Uno, L. Urban, P. Urban, M. Verderi, A. Walkden, W. Wander, H. Weber, J.P. Wellisch, T. Wenaus, D.C. Williams, D. Wright, T. Yamada, H. Yoshida, and D. Zschiesche. Geant4 A simulation toolkit. *Nuclear instruments and methods in physics research section A: Accelerators, Spectrometers, Detectors and Associated Equipment*, 506(3):250–303, 2003.

[105] L.S. Waters. Mcnpx users manual. *Los Alamos.(http://mcnpx. lanl. gov/opendocs/versions/v230/MCNPX_2. 3.0 _Manual. pdf)*, 2002.

[106] H. Bethe and W. Heitler. On the stopping of fast particles and on the creation of positive electrons. *Proceedings of the Royal Society of London. Series A, Containing Papers of a Mathematical and Physical Character*, pages 83–112, 1934.

[107] M.J. Berger and S.M. Seltzer. Bremsstrahlung and photoneutrons from thick tungsten and tantalum targets. *Physical Review C*, 2(2):621, 1970.

[108] P. Pereslavtsev, U. Fischer, S. Simakov, and M. Avrigeanu. Evaluation of d+ ^{6,7} li data for deuteron incident energies up to 50mev. *Nuclear Instruments and Methods in Physics Research Section B: Beam Interactions with Materials and Atoms*, 266(16):3501–3512, 2008.

[109] R.A. Fonseca, L.O. Silva, F.S. Tsung, V.K. Decyk, W. Lu, C. Ren, W.B. Mori, S. Deng, S. Lee, T. Katsouleas, and J.C. Adam. Osiris: A three-dimensional, fully relativistic particle in cell code for modeling plasma based accelerators. In *Computational ScienceICCS 2002*, pages 342–351. Springer, 2002.

[110] J.L. Jones, B.W. Blackburn, S.M. Watson, D.R. Norman, and A.W. Hunt. High-energy photon interrogation for nonproliferation applications. *Nuclear Instruments and Methods in Physics Research Section B: Beam Interactions with Materials and Atoms*, 261(1):326–330, 2007.

[111] J.H. Hubbell. Review of photon interaction cross section data in the medical and biological context. *Physics in medicine and biology*, 44(1):R1, 1999.

[112] H. Chen, S.C. Wilks, J.D. Bonlie, E.P. Liang, J. Myatt, D.F. Price, D.D. Meyerhofer, and P. Beiersdorfer. Relativistic positron creation using ultraintense short pulse lasers. *Physical Review Letters*, 102(10):105001, 2009.

[113] C.D. Chen, P.K. Patel, D.S. Hey, A.J. Mackinnon, M.H. Key, K.U. Akli, T. Bartal, F.N. Beg, S. Chawla, H. Chen, et al. Bremsstrahlung and kα fluorescence measurements for inferring conversion efficiencies into fast ignition relevant hot electrons. *Physics of Plasmas*, 16(8):082705, 2009.

[114] P. A. Norreys, M. Santala, E. Clark, M. Zepf, I. Watts, F. N. Beg, K. Krushelnick, M. Tatarakis, A. E. Dangor, X. Fang, P. Graham, T. McCanny, R. P. Singhal, K. W. D. Ledingham, A. Creswell, D. C. W. Sanderson, J. Magill, A. Machacek, J. S. Wark, R. Allott, B. Kennedy, and D. Neely. Observation of a highly directional γ-ray beam from ultrashort, ultraintense laser pulse interactions with solids. *Physics of Plasmas*, 6(5):2150–2156, 1999.

[115] J. Galy, M. Maucec, D.J. Hamilton, R. Edwards, and J. Magill. Bremsstrahlung production with high-intensity laser matter interactions and applications. *New Journal of Physics*, 9(2):23, 2007.

[116] J.F. Seely, C.I. Szabo, U. Feldman, H. Chen, L.T. Hudson, and A. Henins. Gamma ray spectra from targets irradiated by picosecond lasers. *High Energy Density Physics*, 7(3):150–154, 2011.

[117] C. Zulick, B. Hou, F. Dollar, A. Maksimchuk, J. Nees, A.G.R. Thomas, Z. Zhao, and K. Krushelnick. High resolution bremsstrahlung and fast electron characterization in ultrafast intense laser–solid interactions. *New Journal of Physics*, 15(12):123038, 2013.

[118] S.M. Seltzer and M. J. Berger. Bremsstrahlung energy spectra from electrons with kinetic energy 1 kev–10 gev incident on screened nuclei and orbital electrons of neutral atoms with z= 1–100. *Atomic data and nuclear data tables*, 35(3):345–418, 1986.

[119] L.S. Walter. Mcnpx users manual. Technical report, LA-CP-05-0369 (Los Alamos: LANL), 2005.

[120] C.M. Lee, L. Kissel, R.H. Pratt, and H.K. Tseng. Electron bremsstrahlung spectrum, 1-500 keV. *Physical Review A*, 13(5):1714, 1976.

[121] M. Sherlock. Universal scaling of the electron distribution function in one-dimensional simulations of relativistic laser-plasma interactions. *Physics of Plasmas*, 16(10):103101, 2009.

[122] P. McKenna, D. C. Carroll, R. J. Clarke, R. G. Evans, K. W. D. Ledingham, F. Lindau, O. Lundh, T. McCanny, D. Neely, A. P. L. Robinson, L. Robson, P. T. Simpson, C.-G. Wahlström, and M. Zepf. Lateral electron transport in high-intensity laser-irradiated foils diagnosed by ion emission. *Physical Review Letters*, 98(14):145001, 2007.

[123] H. Chen and S.C. Wilks. Evidence of enhanced effective hot electron temperatures in ultraintense laser-solid interactions due to reflexing. *Laser and Particle Beams*, 23(04):411–416, 2005.

[124] M.N. Quinn, X.H. Yuan, X.X. Lin, D.C. Carroll, O. Tresca, R.J. Gray, M. Coury, C. Li, Y.T. Li, C.M. Brenner, A.P.L. Robinson, D. Neely, B. Zielbauer, J. Fils, T. Kuehl, and P. McKenna. Refluxing of fast electrons in solid targets irradiated by intense, picosecond laser pulses. *Plasma Physics and Controlled Fusion*, 53(2):025007, 2011.

[125] A.J. Mackinnon, Y. Sentoku, P.K. Patel, D.W. Price, S. Hatchett, M.H. Key, C. Andersen, R. Snavely, and R.R. Freeman. Enhancement of proton acceleration by hot-electron recirculation in thin foils irradiated by ultraintense laser pulses. *Physical review letters*, 88(21):215006, 2002.

[126] T. Tresca, D.C. Carroll, X.H. Yuan, B. Aurand, V. Bagnoud, C.M. Brenner, M Coury, J. Fils, R.J. Gray, T. Khl, C. Li, Y.T. Li, X.X. Lin, M.N. Quinn, R.G Evans, B. Zielbauer, M. Roth, D. Neely, and P McKenna. Controlling the properties of ultraintense laserproton sources using transverse refluxing of hot electrons in shaped mass-limited targets. *Plasma Physics and Controlled Fusion*, 53(10):105008, 2011.

[127] K.I. Popov, V.Y. Bychenkov, W. Rozmus, V.F. Kovalev, and R.D. Sydora. Mono-energetic ions from collisionless expansion of spherical multi-species clusters. *Laser and Particle Beams*, 27(02):321–326, 2009.

[128] K.I. Popov, V.Y. Bychenkov, W. Rozmus, R.D. Sydora, and S.S. Bulanov. Vacuum electron acceleration by tightly focused laser pulses with nanoscale targets. *Physics of Plasmas*, 16(5):053106, 2009.

[129] S.D. Baton, M. Koenig, P. Guillou, B. Loupias, A. Benuzzi-Mounaix, J. Fuchs, C. Rousseaux, L. Gremillet, D. Batani, A. Morace, M. Nakatsutsumi, R. Kodama, and Y. Aglitskiy. Relativistic electron transport and confinement within charge-insulated, mass-limited targets. *High Energy Density Physics*, 3(3):358–364, 2007.

[130] A. Henig, D. Kiefer, M. Geissler, S. G. Rykovanov, R. Ramis, R. Hörlein, J. Osterhoff, Zs. Major, L. Veisz, S. Karsch, F. Krausz, D. Habs, and J. Schreiber. Laser-driven shock acceleration of ion beams from spherical mass-limited targets. *Physical Review Letters*, 102:095002, Mar 2009.

[131] A. Morace, C. Bellei, T. Bartal, L. Willingale, J. Kim, A. Maksimchuk, K. Krushelnick, M. S. Wei, P. K. Patel, D. Batani, N. Piovella, R. B. Stephens, and F. N. Beg. Improved laser-to-proton conversion efficiency in isolated reduced mass targets. *Applied Physics Letters*, 103(5):054102, 2013.

[132] S. Ter-Avetisyan, M. Schnürer, P. V. Nickles, M. Kalashnikov, E. Risse, T. Sokollik, W. Sandner, A. Andreev, and V. Tikhonchuk. Quasimonoenergetic deuteron bursts produced by ultraintense laser pulses. *Physical Review Letters*, 96:145006, Apr 2006.

[133] A. J. Kemp and H. Ruhl. Multispecies ion acceleration off laser-irradiated water droplets. *Physics of Plasmas*, 12(3), 2005.

[134] S. Busch, M. Schnrer, M. Kalashnikov, H. Schnnagel, H. Stiel, P. V. Nickles, W. Sandner, S. Ter-Avetisyan, V. Karpov, and U. Vogt. Ion acceleration with ultrafast lasers. *Applied Physics Letters*, 82(19), 2003.

[135] T. Kluge, W. Enghardt, S.D. Kraft, U. Schramm, K. Zeil, T.E. Cowan, and M. Bussmann. Enhanced laser ion acceleration from mass-limited foils. *Physics of Plasmas*, 17(12):123103, 2010.

[136] S. Buffechoux, J. Psikal, M. Nakatsutsumi, L. Romagnani, A. Andreev, K. Zeil, M. Amin, P. Antici, T. Burris-Mog, A. Compant-La-Fontaine, E. d'Humières, S. Fourmaux, S. Gaillard, F. Gobet, F. Hannachi, S. Kraft, A. Mancic, C. Plaisir, G. Sarri, M. Tarisien, T. Toncian, U. Schramm, M. Tampo, P. Audebert, O. Willi, T. E. Cowan, H. Pépin, V. Tikhonchuk, M. Borghesi, and J. Fuchs. Hot electrons transverse refluxing in ultraintense laser-solid interactions. *Physical Review Letters*, 105(1):015005, 2010.

[137] J. Limpouch, J. Psikal, A.A. Andreev, K. Platonov, and S. Kawata. Enhanced laser ion acceleration from mass-limited targets. *Laser and Particle Beams*, 26(02):225–234, 2008.

[138] T. Sokollik, M. Schnürer, S. Steinke, P.V. Nickles, W. Sandner, M. Amin, T. Toncian, O. Willi, and A.A. Andreev. Directional laser-driven ion acceleration from microspheres. *Physical Review Letters*, 103(13):135003, 2009.

[139] T. Sokollik, T. Paasch-Colberg, K. Gorling, U. Eichmann, M. Schnürer, S. Steinke, P.V. Nickles, A. Andreev, and W. Sandner. Laser-driven ion acceleration using isolated mass-limited spheres. *New Journal of Physics*, 12(11):113013, 2010.

[140] P. Neumayer, H.J. Lee, D. Offerman, E. Shipton, A. Kemp, A.L. Kritcher, T. Döppner, C.A. Back, and S.H. Glenzer. Isochoric heating of reduced mass targets by ultra-intense laser produced relativistic electrons. *High Energy Density Physics*, 5(4):244–248, 2009.

[141] M.K. Urry, G. Gregori, O.L. Landen, A. Pak, and S.H. Glenzer. X-ray probe development for collective scattering measurements in dense plasmas. *Journal of Quantitative Spectroscopy and Radiative Transfer*, 99(1):636–648, 2006.

[142] K. U. Akli, M. H. Key, H. K. Chung, S. B. Hansen, R. R. Freeman, M. H. Chen, G. Gregori, S. Hatchett, D. Hey, N. Izumi, J. King, J. Kuba, P. Norreys, A. J. Mackinnon, C. D. Murphy, R. Snavely, R. B. Stephens, C. Stoeckel, W. Theobald, and B. Zhang. Temperature sensitivity of cu kα imaging efficiency using a spherical bragg reflecting crystal. *Physics of Plasmas*, 14(2):023102, 2007.

[143] P. M. Nilson, A. A. Solodov, J. F. Myatt, W. Theobald, P. A. Jaanimagi, L. Gao, C. Stoeckl, R. S. Craxton, J. A. Delettrez, B. Yaakobi, J. D. Zuegel, B. E. Kruschwitz, C. Dorrer, J. H. Kelly, K. U. Akli, P. K. Patel, A. J. Mackinnon, R. Betti, T. C. Sangster, and D. D. Meyerhofer. Scaling hot-electron generation to high-power, kilojoule-class laser-solid interactions. *Phys. Rev. Lett.*, 105:235001, Dec 2010.

[144] A.G.R. Thomas, M. Sherlock, C. Kuranz, C.P. Ridgers, and R.P. Drake. Hybrid vlasov–fokker–planck–maxwell simulations of fast electron transport and the time dependance of k-shell excitation in a mid-z metallic target. *New Journal of Physics*, 15(1):015017, 2013.

[145] L.J. Perkins, B.G. Logan, M.D. Rosen, M.D. Perry, T. D. de la Rubia, N.M. Ghoniem, T. Ditmire, P.T. Springer, and S.C. Wilks. The investigation of high intensity laser driven micro neutron sources for fusion materials research at high fluence. *Nuclear Fusion*, 40(1):1, 2002.

[146] R. Loveman, J. Bendahan, T. Gozani, and J. Stevenson. Time of flight fast neutron radiography. *Nuclear Instruments and Methods in Physics Research Section B: Beam Interactions with Materials and Atoms*, 99(1):765–768, 1995.

[147] L.H. Gray and J. Read. Treatment of cancer with fast neutrons. *Nature*, 152:53, 1943.

[148] C. Zulick, F. Dollar, V. Chvykov, J. Davis, G. Kalinchenko, A. Maksimchuck, G.M. Petrov, A. Raymond, A.G.R. Thomas, L. Willingale, V. Yanovsky, and

K. Krushelnick. Energetic neutron beams generated from femtosecond laser plasma interactions. *Applied Physics Letters*, 102(12):4101, 2013.

[149] N. Izumi, Y. Sentoku, H. Habara, K. Takahashi, F. Ohtani, T. Sonomoto, R. Kodama, T. Norimatsu, H. Fujita, Y. Kitagawa, K. Mima, K. A. Tanaka, and T. Yamanaka. Observation of neutron spectrum produced by fast deuterons via ultraintense laser plasma interactions. *Physical Review E*, 65(3):036413, 2002.

[150] H. Habara, K. L. Lancaster, S. Karsch, C. D. Murphy, P. A. Norreys, R. G. Evans, M. Borghesi, L. Romagnani, M. Zepf, T. Norimatsu, Y. Toyama, R. Kodama, J. A. King, R. Snavely, K. Akli, B. Zhang, R. Freeman, S. Hatchett, A. J. MacKinnon, P. Patel, M. H. Key, C. Stoeckl, R. B. Stephens, R. A. Fonseca, and L. O. Silva. Ion acceleration from the shock front induced by hole boring in ultraintense laser-plasma interactions. *Physical Review E*, 70(4):046414, 2004.

[151] B. Hou, J.A. Nees, Z. He, G. Petrov, J. Davis, J.H. Easter, A.G.R. Thomas, and K.M. Krushelnick. Laser-ion acceleration through controlled surface contamination. *Physics of Plasmas*, 18(4), 2011.

[152] C. Zulick, F. Dollar, V. Chvykov, J. Davis, G. Kalinchenko, A. Maksimchuk, G. M. Petrov, A. Raymond, A. G. R. Thomas, L. Willingale, V. Yanovsky, and K. Krushelnick. Ultra-intense laser neutron generation through efficient deuteron acceleration. *Proceedings of SPIE*, 8779:87790N–87790N–9, 2013.

[153] S.P. Hatchett, C.G. Brown, T.E. Cowan, E.A. Henry, J.S. Johnson, M.H. Key, J.A. Koch, A. B. Langdon, B.F. Lasinski, R.W. Lee, A.J. Mackinnon, D.M. Pennington, M.D. Perry, T.W. Phillips, M. Roth, T. C. Sangster, M.S. Singh, R.A. Snavely, M.A. Stoyer, S.C. Wilks, and K. Yasuike. Electron, photon, and ion beams from the relativistic interaction of petawatt laser pulses with solid targets. *Physics of Plasmas*, 7:2076, 2000.

[154] G.M. Petrov, L. Willingale, J. Davis, T. Petrova, A. Maksimchuk, and K. Krushelnick. The impact of contaminants on laser-driven light ion acceleration. *Physics of Plasmas*, 17(10), 2010.

[155] J. T. Morrison, M. Storm, E. Chowdhury, K. U. Akli, S. Feldman, C. Willis, R. L. Daskalova, T. Growden, P. Berger, T. Ditmire, L. Van Woerkom, and R. R. Freeman. Selective deuteron production using target normal sheath acceleration. *Physics of Plasmas*, 19:030707, 2012.

[156] A. Maksimchuk, A. Raymond, F. Yu, G.M. Petrov, F. Dollar, L. Willingale, C. Zulick, J. Davis, and K. Krushelnick. Dominant dueteron acceleration. *Applied Physics Letters*, 102(19):191117, 2013.

[157] G.M. Petrov and J. Davis. Energy and angular distribution of deuterons from high-intensity laser–target interactions. *Plasma Physics and Controlled Fusion*, 50(1):015004, 2007.

[158] G.M. Petrov and J. Davis. A two-dimensional electromagnetic field algorithm for high-intensity laser–target interactions. *Computer Physics Communications*, 179(12):868–880, 2008.

[159] T.H. Yang and C. Pan. Molecular dynamics simulation of a thin water layer evaporation and evaporation coefficient. *International journal of heat and mass transfer*, 48(17):3516–3526, 2005.

[160] E. Segre. *Nuclei and particles*. 1977.

[161] R. Butsch, D. J. Hofman, C. P. Montoya, P. Paul, and M. Thoennessen. Time scales for fusion-fission and quasifission from giant dipole resonance decay. *Physical Review C*, 44:1515–1527, Oct 1991.

[162] J. R. Oppenheimer. The disintegration of the deuteron by impact. *Phys. Rev.*, 47:845–846, Jun 1935.

[163] R. Serber. The production of high energy neutrons by stripping. *Physical Review*, 72(11):1008, 1947.

[164] Z.H. He, J.A. Nees, B. Hou, K. Krushelnick, and A.G.R. Thomas. Enhancement of plasma wakefield generation and self-compression of femtosecond laser pulses by ionization gradients. *Plasma Physics and Controlled Fusion*, 56(8):084010, 2014.

[165] S.J. Haney, K.W. Berger, G.D. Kubiak, P.D. Rockett, and J. Hunter. Prototype high-speed tape target transport for a laser plasma soft-x-ray projection lithography source. *Applied Optics*, 32(34):6934–6937, 1993.

[166] G. Mourou, B. Brocklesby, T. Tajima, and J. Limpert. The future is fibre accelerators. *Nature Photonics*, 7(4):258–261, 2013.

[167] C. Benedetti, C. B. Schroeder, E. Esarey, and W. P. Leemans. Plasma wakefields driven by an incoherent combination of laser pulses: A path towards high-average power laser-plasma acceleratorsa). *Physics of Plasmas*, 21(5):056706, 2014.